Problems with Incompressibility in Finite Element Analysis

PROBLEMS WITH INCOMPRESSIBILITY IN FINITE ELEMENT ANALYSIS

BY

KYLE MAITLAND, B.Eng.

A THESIS

SUBMITTED TO THE DEPARTMENT OF CIVIL ENGINEERING

AND THE SCHOOL OF GRADUATE STUDIES

OF MCMASTER UNIVERSITY

IN PARTIAL FULFILMENT OF THE REQUIREMENTS

FOR THE DEGREE OF

MASTER OF APPLIED SCIENCE

Master of Applied Science (2010) McMaster University

(Civil Engineering) Hamilton, Ontario, Canada

TITLE:	Problems with Incompressibility in Finite Element Analysis
AUTHOR:	Kyle Maitland B.Eng., (Civil Engineering) McMaster University, Hamilton,Canada
SUPERVISOR:	Dr. D.F.E Stolle
NUMBER OF PAGES:	xv, 111

Abstract

Within this study, low order finite elements were applied to problems with (near) incompressible material behaviour. Solutions were obtained for creep, using transient and dynamic iterative solvers with volumetric strain enhancement algorithms, as well as a flow solution obtained using the fractional step method. To enhance creep algorithm performance, a radial return procedure was implemented.

Preliminary results show that the fraction step method and dynamic iterative solver implementing dynamic relaxation provided adequate results, while other methods required improvement. Volumetric strain enhancement was insufficient to correct pressure drift when using transient analysis. The fractional step method was able to provide good results, but is sensitive to time step and initial stress field.

A thorough evaluation of convergence criteria was conducted through tracking of norms and errors. The trend of norms was used to evaluate the number of iterations required to reach steady-state. The solution acquired from the method of successive approximations was improved and quality pressure plots were obtained, in contrast to the experience from the preliminary analysis.

An analysis of the Barnes ice cap was conducted to verify formulation performance in the context of a real problem. Dynamic relaxation provided results closest to the measured trend and values.

Acknowledgements

In presenting this thesis, the author would like the express his gratitude to the following:

- My wife, for her support and aid throughout this program

- My advisor, Dr. Stolle, for his insight and support

- McMaster University and NSERC for the funding that made this work achievable

Contents

List of Figures

Chapter 1

Introduction

Problems associated with incompressible low order finite elements have been under scrutiny for many years, but universal solutions remain scarce. For most studies, procedures have been developed to overcome some difficulties, but improvements continue to be sought. Many numerical procedures deviate from what could be considered acceptable practice. Consequently, further investigation of the methods used to improve incompressible behaviour is required.

Previously, at McMaster, considerable work was completed with regard to time–dependent deformation, in particular creep of soils, rocks and ice masses. The quality of these solutions is not clear due to pathological problems that develop when the solution is dominated by incompressible creep strains. Methods have been developed since this earlier research to overcome problems. Two solution enhancement methods include the introduction of strain enhancements or smoothening [1, 20, 7] into an existing algorithm and the use of the fractional step method [39, 22, 41]. The primary goal of these techniques is to subvert problematic issues surrounding incompressible behaviour.

1.1 Purpose and Scope

The primary objective of this work is to compare previous and current methods of dealing with incompressible flow when using low order finite elements, and to develop a method to help ensure a quality solution is achieved. In order to investigate the effects of incompressibility in an extreme case, a fully incompressible domain (problem area) will be used. The requirement of an incompressible domain makes creep analysis an ideal choice, as creep flow of many common materials is incompressible. A working assumption is that if the pathological problems can be examined and corrected for extreme cases, problems containing zones of creep or plastic flow can be handled readily.

To find the optimal method for dealing with incompressibility, the fractional step method will be used alongside traditional transient creep formulations with strain enhancement algorithms. The performance, as well as the results obtained through these methods, are analysed thoroughly.

This work is comprised of 8 chapters. Chapter 2 contains a literature review with respect to pressure modes, creep analysis, and the fractional step method. Chapter 3 presents the governing equations for creep flow and incompressible flow using the fraction step method. Chapter 4 contains preliminary analysis using the formulations presented in Chapter 3. Chapter 5 presents an alternate creep formulation that borrows from plasticity formulations. Chapter 6 presents a convergence criterion selection guide. Chapter 7 applies all previous work completed to a real problem, and Chapter 8 presents the concluding remarks.

Chapter 2

Literature Review

2.1 Spurious Pressure Modes and Locking

There are two well documented pathological problems that exist when using low order finite elements for problems approaching incompressibility. These are the development of spurious pressure distributions, and locking of elements. Locking can occur either through bending or volumetric constraints, but this study focuses only on volumetric strain locking. The root of spurious pressure distributions is the presence of a singularity, or near singularity, of the constitutive matrix. Figure 2.1 is an image demonstrating what a mesh with spurious pressures and locking typically looks like; note the extreme values and polarity of pressures (mean stresses). Large jumps in pressure side by side are known as checker boarding, due to the similarities to a checker board when using quadrilateral elements. The velocities associated with creep also become increasingly small due to locking, which often accompanies spurious pressures.

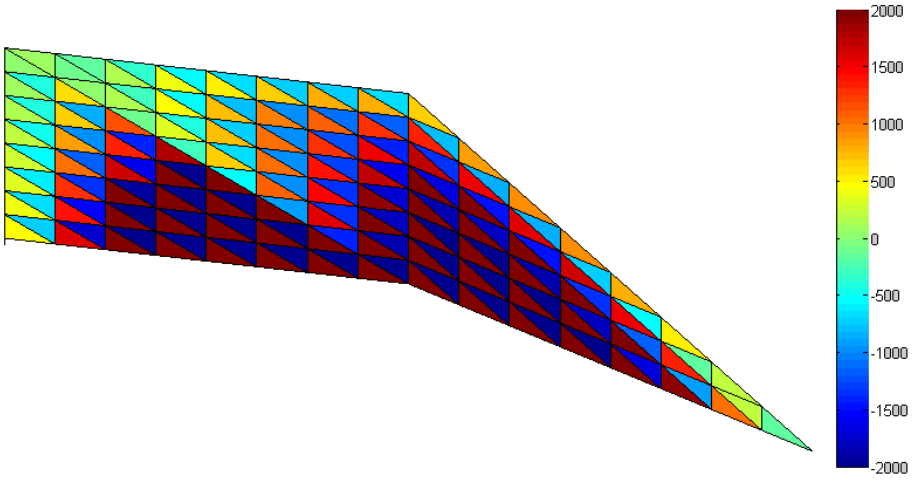

Figure 2.1: A locked mesh with "checker boarding"

Regardless of the limitations imposed by incompressible or near incompressible conditions, many researchers prefer to utilize low order elements for their computational efficiency when dealing with large deformations and adaptive mesh procedures. The existence of pressure modes leads to meaningless results. There have been many attempts to mitigate the undesirable predictions through the application of various penalty methods or reduced integration, as well as the fractional step method, but many of these solution schemes are not desirable due to the artificial nature of the mathematical "tricks" that are employed. To examine the problem in detail, eigenvalue analysis can be conducted.

Eigenvalue analysis on an element stiffness matrix can be conducted to show when spurious modes are generated. An example is included that was presented by Stolle [33]. Using a mixed formulation, with pressure and displacement (or velocity) degrees of freedom, the system of equations describing the physics is of the form

$$\begin{bmatrix} \mathbf{K} & \mathbf{Q} \\ \mathbf{Q}^T & -\mathbf{C} \end{bmatrix} \begin{pmatrix} \mathbf{a} \\ \mathbf{p} \end{pmatrix} = \begin{pmatrix} \mathbf{f} \\ \mathbf{0} \end{pmatrix} \tag{2.1}$$

where $\mathbf{K}$ represents the stiffness of material due to deviatoric stress, $\mathbf{C}$ depends on the bulk modulus, and $\mathbf{Q}$ is a gradient that yields volumetric strain when operating on displacements $\mathbf{a}$ and $\mathbf{p}$ is pressure. Consider a 3-noded element with 6 displacement degrees of freedom. When calculating the eigenvalues for the matrix of Eqn. (2.1) there are 3 positive eigenvalues, which correspond to the modes of deformation that result in strain energy, 3 zero eigenvalues, that correspond to the rigid body modes, which are eliminated by appropriate kinematic boundary conditions, and 1 negative eigenvalue for each pressure degree of freedom. Assuming an elastic modulus $E = 1000$ MPa, and nodal coordinates (0,0), (2,1), and (1,2) for nodes 1,2 and 3, respectively. Eigenvalue analysis was conducted considering the effects of Poisson's ratio (ν) on the eigenvalues for pressure degrees of freedom. Two finite element possibilities were considered: a linear element with constant pressure, and one with linear variation of pressure. The results of the eigenvalue analysis are shown in Fig. 2.2.

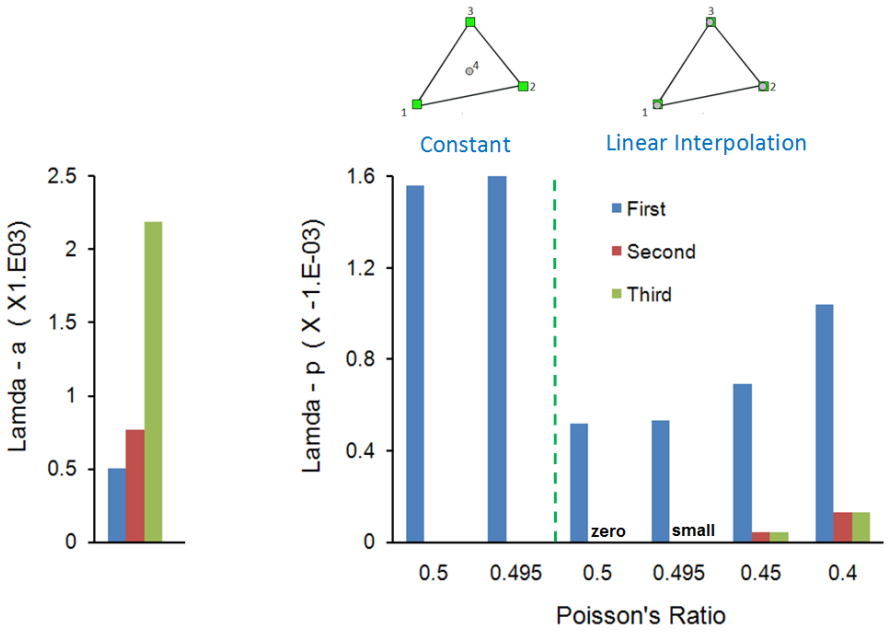

Figure 2.2: Eigenvalues (λ) for linear triangular finite elements

The eigenvalues corresponding to displacement modes were constant for all analyses. As for those corresponding to pressure modes, it is observed that they remain constant for the constant pressure element, but vary as functions of ν for the linear pressure element. The significance of this is that when $\nu \to 0.5$, 2 additional zero eigenvalues (pressure modes) associated with the pressure degrees of freedom appear, which present problems. The mechanism for the pressure mode lies in the incompressibility condition. The singularity in the constitutive matrix occurs as the bulk modulus approaches infinity, with its inverse approaching zero. Given that stresses are related to strains, the interpolation of pressure should be one order less than that of displacement (or velocity), unless some compressibility is available. This restriction is captured by the Babuška-Brezzi (B-B) stability condition for mixed formulations [39].

The generation of a spurious pressure distribution is often accompanied with locking. Referring to Fig. 2.3, where linear elements are fixed along the

base, displacement of the free node is such that it can only be parallel to the base to maintain constant volume. Since elements A and B do not share a base of common orientation, neither element can deform. Any attempt for this node to displace will be countered by the generation of a pressure of the magnitude required to prevent this displacement.

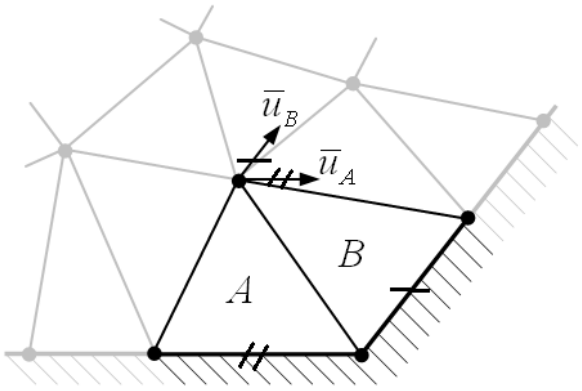

Figure 2.3: Two element assemblage that will exhibit locking within incompressible behaviour

There are two main approaches to accommodate incompressibility. One is to introduce a volumetric strain enhancement, while the other is to provide "algorithmic compressibility", via the fractional step method. The strain enhancement approach is introduced in a creep formulation in this work, with the fractional step method being used within the context of a flow formulation.

2.1.1 Smoothening to Prevent Volumetric Locking

The smoothening method used in this study follows that proposed by Detournay and Dzik [7], which they refer to as the nodal mixed discretization method. Mixed discretization refers to the deviatoric and volumetric tensors being separated. The relaxation imposed is such that the deviatoric components occur on the element level, while the volumetric components are computed for an

assembly of elements. The main assumption is that any smoothening should leave the deviatoric strain rate in an element unchanged. When using this technique an explicit dynamic time-stepping algorithm was used. Given the nature of such an algorithm, an element at the "wave front" temporarily has some "compressibility". Given the nodal velocities, strain rates can be calculated. In the smoothening technique a weighted average of volumetric strain rates at the nodes is calculated based on volumetric strain rates within an element.

$$\dot{\epsilon}_v^n = \frac{\sum_{i=1}^{m_n} \dot{\epsilon}_{v^e} V^e}{\sum_{i=1}^{m_n} V^e} \tag{2.2}$$

The superscripts 'n' and 'e' denote nodal and elemental values, $\dot{\epsilon}_v$ is the volumetric strain rate, V is the volume, and m_n is the number of elements surrounding the node. The nodal values are then used to determine the average volumetric strain rates in each element via

$$\bar{\dot{\epsilon}}_v = \frac{1}{d} \sum_{n=1}^{d} \dot{\epsilon}_v^n \tag{2.3}$$

where $\bar{\dot{\epsilon}}_v$ is the averaged volumetric stress of the element, and d is the number of nodes per element. Once the average volumetric strain rate has been attained, the total strain rate is given by

$$\dot{\boldsymbol{\epsilon}} = \dot{\boldsymbol{\epsilon}}^d - \frac{\dot{\epsilon}_v^e}{3}\mathbf{I} + \frac{\bar{\dot{\epsilon}}_v}{3}\mathbf{I} \tag{2.4}$$

where $\mathbf{I}$ is the matrix form of Kronecker's delta. Figure 2.4 provides a graphical representation of this technique. For example, the area weighted nodal volumetric strain at node 1 is calculated given volumetric strains in elements a,b,c, and d. Similar calculations are repeated for all other nodes, and then the

average elemental value for element c is obtained by averaging nodal volumes 1,2, and 3. It is important to realize that this smoothening is applied on the incremental level.

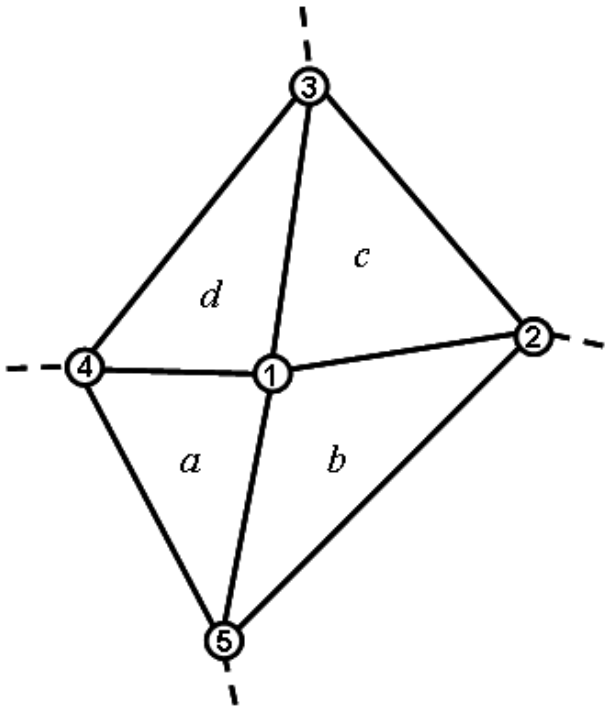

Figure 2.4: Four element assembly

This smoothening technique can be viewed as representing an explicit version of a mixed finite element approach that has volumetric strain degrees of freedom, in addition to displacement (or velocity) degrees of freedom. Two sets of equations are solved: momentum, and volume change. First the momentum equation is solved to get an incremental displacement, followed by the equations for discretized volumetric strain increment (rate). The equation for the volumetric strain rate degrees of freedom is given by

$$\int \delta\dot{\epsilon}_v \left(\dot{\boldsymbol{\epsilon}}_v^e - \dot{\boldsymbol{\epsilon}}_v\right) dV = 0 \tag{2.5}$$

with $\dot{\epsilon}_v = \mathbf{Na}$ or

$$\int \mathbf{N}^T \mathbf{N} dV \dot{\boldsymbol{\epsilon}}_v^n = \int \mathbf{N}^T \dot{\boldsymbol{\epsilon}}_v^e dV \tag{2.6}$$

where, as before, $\dot{\boldsymbol{\epsilon}}_v^n$ and $\dot{\boldsymbol{\epsilon}}_v^e$ are the nodal and elemental volumetric strain rates, respectively. Equation (2.6) uses a stepwise uncoupled volumetric strain rate of an element to calculate the nodal strain rates. These values are then used to determine the total strain rate within the element as $\dot{\boldsymbol{\epsilon}} \rightarrow \dot{\boldsymbol{\epsilon}} - \frac{\mathbf{I}}{3}\dot{\boldsymbol{\epsilon}}_v^e + \frac{\mathbf{I}}{3}\mathbf{N}'\dot{\boldsymbol{\epsilon}}_v^n$, where $\mathbf{N}'$ is $\mathbf{N}$ at the centroid of the element. In essence, the volumetric strain rate obtained from the velocity field is replaced by an average smoothened volumetric strain rate while leaving the deviatoric strain rate unaffected. This scheme is identical to that of Dzik and Detourney [7] when the left hand side of Eqn. (2.6) is replaced with a "lumped mass" equivalent.

Bonet and Burton [1] used a linear tetrahedron together with an explicit dynamic solver for incompressible materials. A modified nodal volume was used to find a smoothened pressure for each element. The use of an explicit dynamic solver also allows for additional compressibility. Micheli and Mocellin [20] presented an explicit formulation using a linear tetrahedron for simulation of high speed forming. This element was shown to be efficient when using adaptive non-structured meshes. In the authors' words (Micheli and Mocellin) the procedure is a simple method inspired by the average nodal pressure method [20]. Volumetric strains were smoothened in this study, using a Jacobian matrix to capture volume change. This method was noted to be successful for volumetric locking, but not for bending locking.

2.2 Transient Creep Analysis

Creep can be described as the time-dependant deformation of a material under constant stress [19]. In addition to time and stress level, creep also depends on temperature. The time dependency is sometimes replaced by a creep strain dependency to form an equation of the state $\dot{\boldsymbol{\epsilon}}^c = f\left(\boldsymbol{\sigma}, \boldsymbol{\epsilon}^c, T\right)$[19].

Creep is generally separated into 3 phases: I-primary, II-secondary, and III-tertiary (Fig. 2.5), with tertiary creep often ending in creep rupture. The analysis within this paper focuses on secondary creep, also referred to as steady state-creep. With the assumption of steady-state, the creep strain rate is independent of time, assuming that stress and temperature do not change. It is important to note that a material does not necessarily go through all three stages, depending on the stress level. Creep rate generally increases with stress level, as does the probability of creep failure.

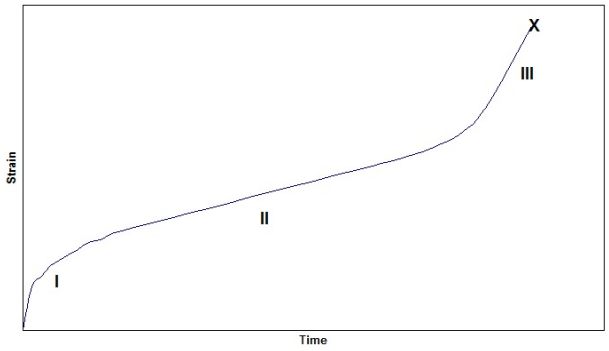

Figure 2.5: Creep stages and behaviour

Within the McMaster context there has been a fair deal of research in creep mechanics. Emery [9], in his research at the University of British Columbia, worked with various creep laws and formulations using linear elements. The scope of the research dealt with both steady-state creep and creep rupture

within the context of undrained soil response. Later, under Dr. Emery's supervision at McMaster, Hanafy [12] went on to model excavation of tunnels within squeezing rock. Creep was analysed before and after the installation of tunnel liners. The joint type (rough or smooth) between the lining and the rock was investigated to study the influence of interface type. Linear elements were once again used.

Within the context of glaciology, Nguyen [21] studied the effects of various creep laws, the use of joint elements to model basal sliding and failure, and tensile cracking within an ice mass. A sliding layer was introduced above the base, comprised of a material with a greater flow rate, along with joint elements, to allow concentrated basal sliding. Linear elements were used for this analysis. Hanafy [13] also modelled the Barnes Ice Cap, in which the focus was the steady-state solution. The initial analyses showed that with the creep laws used, the creep stresses were too high, but it was pointed out that this could be refined. Van Egmond [8] compared the effects of initial stress distribution on creep flow, as well as temperature. It was concluded that gravity loading may not provide an accurate starting point for creep analysis as "glaciers may have a 'memory' of previous stress states imposed on the elastic state of stress under gravity" [8] . Chan [3] studied the creep and fracture mechanics of ice flows. Preliminary results for the fracture of ice were obtained showing that redistribution of stress around a fracture was unchanged after approximated 48 days, and that there are significant changes in the stress distribution before cracking. Rate of crack propagation was shown to be sensitive to the angle of the slope. Further study of ice fracture was recommended.

Within the scope of this work, Stolle [30] further studied the Barnes ice cap, this time to model instability or 'surges' of the ice mass. Stolle noticed that

with the use of low order elements, the prediction of the pressure field was not accurate, and that the velocity locked once steady state creep was attained. To remedy this, higher order mixed elements with velocity and pressure degrees of freedom were used to check pressure fields and find solutions to steady state creep. As the creep does not depend on pressure distribution, and glacier flow tended to be dominated by shear deformation, this was not considered to be overly important to the problem when addressing the instability condition. The sensitivity of creep to boundary conditions was also tested. Killeavy [18] further studied this ice mass, as well as Mount Logan, in order to identify flow lines (particle paths) and isochrones, that were used to identify the relative age of the ice. In his research, higher order elements were used.

2.2.1 Creep Solution Methodology

For the works presented that used low order elements, the basic approach was to use an initial strain formulation based on an initial stiffness procedure [32]. Nonlinear equations often have the stiffness matrix as a function of displacement, *i.e.*,

$$\mathbf{K}(\mathbf{a})\mathbf{a} = \mathbf{F} \tag{2.7}$$

in which $\mathbf{K}(\mathbf{a})$ is the displacement dependent stiffness and $\mathbf{F}$ is the applied force. By assuming that the stiffness at the beginning of the problem ($\mathbf{K}(\mathbf{a}^*)$) is valid for the duration of the analysis, calculations are simplified, but rate of convergence is decreased (initial stiffness procedure).

Defining the residual load vector ($\mathbf{R} = \mathbf{F} - \mathbf{K}(\mathbf{a}^*)$), its values at time t_{n+1}

are

$$\mathbf{R}_{n+1} = \mathbf{F}_{n+1} - \int_V \mathbf{B}^T \boldsymbol{\sigma}_{n+1} dV = 0 \tag{2.8}$$

where $\boldsymbol{\sigma}_{n+1} = \boldsymbol{\sigma}_n + \Delta\boldsymbol{\sigma}_n$, in which $\boldsymbol{\sigma}_n$ is a known stress and $\Delta\boldsymbol{\sigma}$ is a stress increment that one wishes to calculate. Through use of the additivity postulate, $\Delta\epsilon = \Delta\epsilon^e + \Delta\epsilon^c$, where ϵ^e is the elastic strain and ϵ^c is the creep strain, the stress increment is given by

$$\Delta\boldsymbol{\sigma}_n = \mathbf{D}\left(\Delta\epsilon - \Delta\epsilon^c\right) \tag{2.9}$$

where $\mathbf{D}$ is the linear elastic constitutive matrix. Assuming constant loading and relating strain increment to displacement increment $\Delta\mathbf{a}$ via the strain-displacement matrix $\mathbf{B}$

$$\int_V \mathbf{B}^T\mathbf{D}\mathbf{B} dV \Delta\mathbf{a}_n = \mathbf{F} - \int_V \mathbf{B}^T \sigma_n dV + \int_V \mathbf{B}^T\mathbf{D}\boldsymbol{\epsilon}_n^c dV \tag{2.10}$$

which can be reduced to

$$\mathbf{K}\Delta\mathbf{a}_n = \mathbf{R}_n + \int_V \mathbf{B}^T\mathbf{D}\boldsymbol{\epsilon}_n^c dV \tag{2.11}$$

with $\mathbf{K}$ being the "elastic" stiffness matrix. It is important to note that as the residual load approaches zero, the creep loading ($\int_V \mathbf{B}^T\mathbf{D}\boldsymbol{\epsilon}_n^c dV$) will continue to drive the system. With respect to the previous sequence of equations, the initial strain method follows

1. Determine initial stresses and loads.
2. Given $\boldsymbol{\sigma}_n$, evaluate $\Delta\boldsymbol{\epsilon}_n^c$.
3. Find $\Delta\mathbf{a}_n$: $\mathbf{K}\Delta\mathbf{a}_n = \mathbf{R}_n + \int_V \mathbf{B}^T\mathbf{D}\boldsymbol{\epsilon}_n^c dV$
4. Determine $\Delta\boldsymbol{\epsilon}_n = \mathbf{B}\mathbf{a}_n$ and calculate the stress increment.
5. Update all quantities, including stresses.
6. Check for convergence to steady state field and repeat from step 2 if convergence is not achieved.

This approach is general, allowing the engineer to choose any creep laws or formulation that are applicable for the problem at hand. The freedom of choice of creep law has been particularly well exercised in the work of Nguyen [21], where a large number of creep laws were evaluated.

2.3 The Fractional Step Method

The fractional step method has its origins in fluid mechanics, involving the solution of the Stokes' flow equations. This method, also called the velocity correction procedure or operator splitting scheme, provides algorithmic compressibility that ensures $\mathbf{C}$ does not vanish for incompressible problems. Schneider and coworkers [29] introduced the velocity correction procedure in 1978, based on ideas presented in finite differences by Chorin [4]. Kawahara and Ohmiya [17] also presented this type of formulation. In the early 1990s, Zienkiwicz and Wu [41] demonstrated that it is possible to introduce algorithmic compressibility in various ways. The velocity correction method has also been adapted for soil mechanics; for example, by Pastor et al. [25], as well as by Huang and coworkers [15]. The necessary change for soil mechanics is to

introduce the concept of effective stress and pore pressure, opposed to deviatoric stress and pressure (mean stress) that is used for fluids or incompressible solid formulations. Various other papers presenting similar methods are also available [38, 23, 36, 39, 40, 22, 16]. This family of formulations uses equal order of interpolation for displacement (or velocity) and pressure.

2.3.1 Example Fractional Step Formulation

Given that there are various versions of the fractional step method, the details of which change slightly, it would be prudent to examine a formulation that differs from that presented later in this work. The formulation to follow is taken from Zienkiewicz and Wu [41]. Adopting indicial notation, the momentum balance and continuity equation are given by

$$\frac{du}{dt} \approx \frac{u_i^{n+1} - u_i^n}{\Delta t} = \frac{\partial \tau_{ij}^n}{\partial x_j} + \frac{\partial (p^n + \theta_2 \Delta p)}{\partial x_i} \tag{2.12}$$

$$\frac{1}{c^2}\frac{dp}{dt} \approx \frac{1}{c^2}\frac{\Delta p}{\Delta t} = \frac{\partial ((1-\theta_1)u_j^n + \theta_1 u_j^{n+1})}{\partial x_j} \tag{2.13}$$

where the superscript 'n' denotes the iteration, τ_{ij} the deviatoric stresses, p the pressure, c the wave speed, and u the velocity. Parameters θ_1 and θ_2 control whether the algorithm is implicit or explicit. Values of $\theta_1 = 1$ and $\theta_2 = 0$ are used here to simplify further equations.

The operator split, which is characteristic of this type of formulation, is introduced next. The purpose of this split is to subdivide the momentum equation into independent deviatoric and spherical parts.

$$\frac{u_i^* - u_i^n}{\Delta t} = \frac{\partial \tau_{ij}^n}{\partial x_j} \tag{2.14}$$

$$\frac{u_i^{n+1} - u_i^*}{\Delta t} = \frac{\partial p^n}{\partial x_i} \tag{2.15}$$

where u^* is a predictor velocity that ignores the effects of pressure. In the next step we differentiate Eqn. (2.15) with respect to x_i

$$\frac{1}{\Delta t}\left(\frac{\partial u_i^{n+1}}{\partial x_i} - \frac{\partial u_i^*}{\partial x_i}\right) = \frac{\partial}{\partial x_i}\frac{\partial}{\partial x_i}p^n \tag{2.16}$$

which is then substituted into the continuity equation, to eliminate u_i^{n+1}.

$$\frac{1}{c^2}\frac{\Delta p}{\Delta t} = \frac{\partial}{\partial x_i}\frac{\partial}{\partial x_i}p^n - \frac{1}{\Delta t_{int}}\frac{\partial u_i^*}{\partial x_i} \tag{2.17}$$

The rate of change of pressure now depends on the pressure gradient. These gradients stabilize the solution. Furthermore, Eqns. (2.14), (2.15), (2.17) are then ready to be discretized using the Galerkin method for the finite element implementation. As the emphasis is on a steady-state solution, it was observed by Zienkiewicz and Nithiarasu that Δt_{int} (Eqn. (2.17) R.H.S) need not be the same as Δt (Eqn. (2.17) L.H.S)[23]. Increasing Δt_{int} by a factor of 2 was found to improve the pressure field. Nithiarasu improved the algorithm by adopting an artificial wave speed in the continuity equation (Eqn. (2.17)), that depends on size of element and shear modulus [22]. It is important to realize that the success of the scheme is attributed to the iterative nature of the algorithm and the inclusion of the pressure gradient term when updating pressure. The procedure adopted in the current study is presented in Sec. (3.2.3).

2.3.2 Justification of Equal Order of Interpretation

An advantage of the fractional step method is that it allows the mapping of pressure and velocity to be of the same order of interpolation. While this is seen as advantageous, there is an inconsistency given that the stresses are constant

for linear displacement (velocity) elements. The rational behind choosing to work with this equal order of interpolation, despite violating the Babuska Brezzi criterion, can be found in the text by Zienkiewicz and Taylor [39], and is briefly presented in the following text.

When using a standard formulation, the system of equations in matrix form appears as below.

$$\begin{bmatrix} \mathbf{A} & \mathbf{Q} \\ \mathbf{Q}^T & -\mathbf{C} \end{bmatrix} \begin{pmatrix} \mathbf{v} \\ \mathbf{p} \end{pmatrix} = \begin{pmatrix} \mathbf{f}_1 \\ \mathbf{0} \end{pmatrix} \tag{2.18}$$

where $A = \int \mathbf{B}^T \mathbf{D}_d \mathbf{B} d\Omega$; $Q = \int \mathbf{B}^T \mathbf{m} \mathbf{N}_p d\Omega$; $C = \int \mathbf{N}_p^T \frac{1}{K} \mathbf{N}_p d\Omega$. Observe that $\mathbf{C}$ is in terms of the bulk modulus, and therefore as $\nu \to 0.5$, $\mathbf{C}$ will approach zero. When $C \to 0$ spurious pressure distributions occur as the matrix becomes singular, causing the generation of additional zero eigenvalues. In contrast the fractional step method has the effect of adding a non-zero term to the diagonal [39], algorithmically, yielding a steady state solution that is consistent with the matrix equation

$$\begin{bmatrix} \mathbf{A} & \mathbf{Q} \\ \mathbf{Q}^T & \Delta t(\mathbf{Q}^T \mathbf{C} \mathbf{Q} - \theta \mathbf{H}) \end{bmatrix} \begin{pmatrix} \mathbf{v} \\ \mathbf{p} \end{pmatrix} = \begin{pmatrix} \mathbf{f}_1 \\ \mathbf{0} \end{pmatrix} \tag{2.19}$$

It should be noted that the term on the diagonal no longer depends on the bulk modulus alone, due to the presence of $\mathbf{H} = \int \mathbf{B}_p^T \mathbf{B}_p d\Omega$. This means that the term will not vanish as $\nu \to 0.5$ and the rigid body modes remain intact. Although there are slight differences between the form of presentation chosen by Zienkiewicz and Taylor [39], and the presentation for this research, what is important is that there is effectively no zero term on the diagonal of the matrix, so that additional energy free deformation modes are not present. It

should be noted that Eqn. (2.19) corresponds to a quasi-static solution.

2.4 Material Properties of Ice

To make this body of work complete within the context of glacier flow, typical values for material properties are included. The elastic modulus ranges from 8687–9307 kPa for dynamic conditions [21], and was reported as 5998 for static conditions [11]. Poisson's ratio was similarly reported as ranging between 0.31–0.365 and 0.5 for dynamic and static conditions, respectively [21]. The density of ice was found to range from 0.85–0.91 g/mm^3 [21] and the shear strength for natural ice ranges from 0.97–1.08 MPa [30].

Chapter 3

Fully Incompressible Flow

3.1 Introduction

When using the finite element method, situations arise where it is necessary to model a slope or foundation in which the material response is (near) incompressible. Often the finite elements used for such problems are of higher order. For such elements locking is avoided as there are more degrees of freedom per element, which increases the flexibility of the element, while maintaining a constant volume. Nevertheless, low order elements are preferred for large deformation modelling or adaptive finite element schemes. This is particularly true for extensions of FEM to 3 dimensions [36, 25, 41]. The weaknesses associated with these elements are the development of spurious pressure distributions and locking, as indicated previously. Two approaches have been used to mitigate these problems in this work. Alternative approaches, which were not evaluated in this study can be found in the following [6, 2, 35, 24, 28]

The goal of this chapter is to present two algorithms for predicting (near) incompressible flow behaviour. The first approach is the method of successive approximation starting from the elastic solution, where the material is allowed

to creep until the 'steady state' solution (or flow solution) has been obtained. In order to eliminate locking and spurious pressure distributions some 'artificial compressibility' is added to the creep law, as well as the smoothening of volumetric strain increments. The other formulation considered is the fractional step method (FSM) presented by Nithiarasu and Zienkiewicz [40]. Nithiarasu extended this procedure to the solution of solid mechanics problems, taking advantage of the fact that the form of Stoke's equation for creeping flow is identical to that of an isotropic, elastic solid [22].

The motivation behind testing the various formulations for dealing with an incompressible low order element lies in the extension of regular FEM to the Material Point Method (MPM). The mapping for low order elements is much simpler, and therefore less problematic. Before carrying out the extension, it is necessary that the pressure and element locking difficulties are properly addressed.

3.2 Solution Schemes

3.2.1 Governing Equations

Before the details of the solution schemes are disclosed, the governing field equations for the formulations are presented. For the creep algorithm, a Lagrangian formulation is used, while the fractional step method, being rooted in fluid mechanics, uses a spatial description of equilibrium.

The Lagrangian Formulation

In the Lagrangian formulation, the calculation of a derivative is based on using the initial configuration as a reference, in which each particle is tracked

explicitly, $\mathbf{x} = \mathbf{u} + \mathbf{a}; \mathbf{u} = \mathbf{u}(\mathbf{a}, t)$, with $\mathbf{x}$ being the final position, $\mathbf{u}$ being the displacement, and $\mathbf{a}$ being the initial position, and the dot notation implies the time derivative.

$$\mathbf{L}_a^T \boldsymbol{\sigma} + \rho \mathbf{g} = \rho \ddot{\mathbf{u}} \tag{3.1}$$

for a 2-D formulation, the operator $\mathbf{L}_a^T = \begin{bmatrix} \frac{\partial}{\partial a_x} & 0 & \frac{\partial}{\partial a_y} \\ 0 & \frac{\partial}{\partial a_y} & \frac{\partial}{\partial a_x} \end{bmatrix}$, ρ the material density and $\mathbf{g}$ the gravitational acceleration vector. The total stress at a point is decomposed according to $\boldsymbol{\sigma} = \mathbf{S} + \mathbf{m}^T p$, where $\mathbf{S}$ is the deviatoric stress, p is the spherical stress (also referred to as pressure), and $\mathbf{m}$ is the vector form of Kronecker's delta ($\mathbf{m} = (1, 1, 1, 0)^T$) . Given that during Lagrangian analysis the reference configuration is normally updated, and that deformations relative to the updated configuration are small, it is generally assumed that $\frac{\partial}{\partial a} \approx \frac{\partial}{\partial x}$. It follows that $\mathbf{L}_a^T \approx \mathbf{L}^T$.

The equation of mass balance is given

$$\dot{\mathbf{M}} = \frac{d}{dt} \int \rho dV = 0 \tag{3.2}$$

When mass ($\mathbf{M}$) is conserved, *i.e.*, none is gained or lost, Eqn. (3.2) is satisfied implicitly. The strain is given by $\boldsymbol{\epsilon} = \mathbf{L}_a \mathbf{u}$, with total strain being defined as the sum of the elastic and creep strains ($\boldsymbol{\epsilon} = \boldsymbol{\epsilon}^e + \boldsymbol{\epsilon}^c$). As creep strain is presented in more detail in Sec. (3.2.2), one proceeds by assuming elastic behaviour, with the constitutive equation of the form

$$\dot{\boldsymbol{\sigma}} = \mathbf{D}^e (\dot{\boldsymbol{\epsilon}} - \dot{\boldsymbol{\epsilon}}^c) \tag{3.3}$$

in which $\mathbf{D}^e$ is the linear elastic constitutive matrix, which for 2-D plane strain

applications is given by:

$$\mathbf{D}^e = \frac{E}{(1+\nu)(1-2\nu)} \begin{pmatrix} 1-\nu & \nu & \nu & 0 \\ \nu & 1-\nu & \nu & 0 \\ \nu & \nu & 1-\nu & 0 \\ 0 & 0 & 0 & 2(1-2\nu) \end{pmatrix} \tag{3.4}$$

Stress and strain rates are expressed in their vector form as $\dot{\boldsymbol{\sigma}} = (\dot{\sigma}_{xx}, \dot{\sigma}_{yy}, \dot{\sigma}_{zz}, \dot{\sigma}_{xy})$ and $\dot{\boldsymbol{\epsilon}} = (\dot{\epsilon}_{xx}, \dot{\epsilon}_{yy}, \dot{\epsilon}_{zz}, \dot{\gamma}_{xy})$, respectively. It should be noted that the mathematical definition of shear strain is not used in Eqn. (3.3), and in its place is the engineering shear strain ($\epsilon_{xy} = 2\gamma_{xy}$). This definition of strain is implied unless noted otherwise. As the problems being solved in this study are plane strain, the out-of-plane strain rates need not be considered explicitly but are accounted for implicitly.

The Spatial Formulation

In the spatial description of equilibrium, usually used in fluid mechanics, the mass is moving through space, such that $\mathbf{x} = \mathbf{u} + \mathbf{a}$ and $\mathbf{u} = \mathbf{u}(\mathbf{x}, t)$, where $\mathbf{x}$ changes continuously. In this thesis Stoke's flow is assumed, in which advection is assumed to be negligible. The rate of deformation is defined as $\mathbf{d} = \mathbf{L}_x\mathbf{v}$ in which $\mathbf{L}_x = \mathbf{L}$ is the differential operator with respect to $\mathbf{x}$ and $\mathbf{v} = \dot{\mathbf{u}}$. For the purpose of this study it is also assumed $\mathbf{d} = \dot{\boldsymbol{\epsilon}}$, although strictly speaking, this is not true. Momentum (Eqn. (3.5)) and mass balance in terms of continuity (Eqn. (3.6)) are given as

$$\rho\dot{\mathbf{v}} = \mathbf{L}^T\boldsymbol{\sigma} + \mathbf{b} \tag{3.5}$$

$$\frac{1}{c^2}\dot{\mathbf{p}} = \rho\nabla \cdot \mathbf{v} = \rho\mathbf{m}^T\mathbf{L}\mathbf{v} \tag{3.6}$$

where ρ is the density, $\mathbf{v}$ the velocity, $\mathbf{L}$ a gradient operator, $\boldsymbol{\sigma}$ the stress vector, $\mathbf{B}$ the body forces, c the wave speed, and $\mathbf{p}$ the pressure. The term on the right hand side of the continuity equation, can be written as $\dot{\epsilon}_v = \nabla \cdot \mathbf{v}$.

The constitutive relation for this formulation is based on the deviatoric stress being related to the velocity gradient

$$\mathbf{S} = \mathbf{D}^f \mathbf{d} \tag{3.7}$$

with

$$\mathbf{D}^f = \frac{\mu}{3} \begin{bmatrix} 4 & -2 & 0 \\ -2 & 4 & 0 \\ 0 & 0 & 6 \end{bmatrix} \tag{3.8}$$

and μ being the viscosity. The vectors for deviatoric stress and rate deformation are defined as $\mathbf{S} = (S_{xx}, S_{yy}, S_{xy})$ and $\mathbf{d} = \dot{\boldsymbol{\epsilon}} = (\dot{\epsilon}_{xx}, \dot{\epsilon}_{yy}, \dot{\gamma}_{xy})$, respectively. The out-of-plane strain rate, $\dot{\epsilon}_{zz} = 0$ for planar problems.

3.2.2 Creep Flow Analysis

For the analysis of incompressible material three approaches are considered that treat the material as a creeping elastic solid. The first is the method of successive approximations (MSA), and uses a standard matrix solver to calculate the steady-state solution. The second is central difference scheme (CDS), which adopts an explicit dynamic time stepping algorithm to establish the steady-state solution. The third is based on dynamic relaxation (DR), which adjusts the density in the CDS algorithm to accelerate to steady-state [34].

Creep Flow Formulation

In this formulation one begins with the constitutive law given by Eqn. (3.3). By assuming there is an elastic body that creeps, the elastic strain is decomposed using the additivity postulate such that $\dot{\boldsymbol{\epsilon}}^e = \dot{\boldsymbol{\epsilon}} - \dot{\boldsymbol{\epsilon}}^c$. Within this framework, the elasticity takes into account the instantaneous response, while the creep accounts for the time-dependant response.

The creep law used in this work is that of Glen, which states that poly-crystalline ice obeys a power creep law $\dot{\epsilon}^c = A\sigma^n$ [10]. A similar law is used for multi-axial conditions such that $\dot{\epsilon}^c_e = A\sigma^n_e$ where Dorn's definition of equivalent stress and strain rate are given by

$$\sigma_e = \frac{1}{\sqrt{2}}\sqrt{(\sigma_x - \sigma_y)^2 + (\sigma_y - \sigma_z)^2 + (\sigma_z - \sigma_x)^2 + 6\tau_{xy}^2} = \sqrt{\frac{3}{2}\mathbf{S}^T\mathbf{S}} \tag{3.9}$$

$$\dot{\epsilon}_e = \frac{2}{\sqrt{3}}\sqrt{\dot{\epsilon_x}^2 + \dot{\epsilon_y}^2 + \dot{\epsilon_x}\dot{\epsilon_y} + \left(\frac{\dot{\gamma}_{xy}}{2}\right)^2} = \sqrt{\frac{2}{3}(\dot{\boldsymbol{\epsilon}}^d)^T(\dot{\boldsymbol{\epsilon}}^d)} \tag{3.10}$$

Both of these invariants reduce to the uniaxial form for uniaxial conditions. When extending the creep law to multiple dimensions, there are three assumptions: creep flow is incompressible, creep is independent of the mean normal stress (independent of the first invariant of stress), and creep strain rate ($\dot{\boldsymbol{\epsilon}}^C$) is proportional to the deviator stress ($\mathbf{S}$) [19, 9].

$$\dot{\boldsymbol{\epsilon}}^c = \lambda_1\mathbf{S} \tag{3.11}$$

where λ_1 is a proportionality constant. Squaring this equation, it follows that

$$(\dot{\boldsymbol{\epsilon}}^c)^T(\dot{\boldsymbol{\epsilon}}^c) = \lambda_1^2\mathbf{S}^T\mathbf{S} \tag{3.12}$$

Introducing Dorn's definitions of equivalent strain and stress, in order to extend from 1^D to multi-axial creep, Eqn. (3.12) becomes

$$\frac{9}{4}(\dot{\epsilon}_e^c)^2 = \lambda_1^2 \sigma_e^2 \tag{3.13}$$

Solving for λ_1, it can be shown

$$\lambda_1 = \frac{3}{2}\frac{\dot{\epsilon}_e^c}{\sigma_e} \tag{3.14}$$

which is substituted back into Eqn. (3.11)

$$\dot{\boldsymbol{\epsilon}}^c = \frac{3}{2}\frac{\dot{\epsilon}_e^c}{\sigma_e}\mathbf{S} \tag{3.15}$$

The creep law can also be developed using an approach attributed to Perzyna [27], and applied to finite elements following the example of Zienkiewicz and Cormeau [37]. Beginning by assuming the creep flow is proportional to the gradient of equivalent stress, which acts as a 'creep potential', one has

$$\dot{\boldsymbol{\epsilon}}^c = \lambda_2 \frac{\partial \sigma_e}{\partial \boldsymbol{\sigma}} \tag{3.16}$$

squaring this equation, and introducing Dorn's definitions for equivalent strain rate

$$\lambda_2 = \epsilon_e^c \tag{3.17}$$

thus delivering the same multi-axial creep law and showing that

$$\lambda_1 = \frac{3}{2}\frac{\lambda_2}{\sigma_e} \quad \text{or} \quad \dot{\boldsymbol{\epsilon}}^c = \frac{3}{2}\frac{\lambda_2}{\sigma_e}\mathbf{S} \tag{3.18}$$

In order to establish the creep law for use, the relationship between $\dot{\epsilon}_e^c$ and σ_e

must be defined.

A parallel can be drawn between the creep law and fluid flow

$$\dot{\boldsymbol{\epsilon}}^c = \frac{3}{2}\frac{\dot{\epsilon}_e^c}{\sigma_e}\mathbf{S} = \frac{1}{2\mu}\mathbf{S} \tag{3.19}$$

where the viscosity, $\mu = \frac{1}{3}\frac{\sigma_e}{\dot{\epsilon}_e^c}$. It should be noted that when substituting Eqn. (3.19) into Eqn. (3.3) it is necessary to take into account $\dot{\gamma}_{xy} = 2\dot{\epsilon}_{xy}$. Looking to the governing equation for isotropic elasticity where

$$\boldsymbol{\epsilon}^d = \frac{1}{2G}\mathbf{S} \tag{3.20}$$

with $\boldsymbol{\epsilon}^d = \boldsymbol{\epsilon} - \frac{\mathbf{m}\epsilon_v}{3}$ being the deviatoric strain, one can observe similarities to the creep law. Again, for the 'shear term': $\gamma_{xy} = 2\epsilon_{xy} = S_{xy}/G$. The difference is that for 'a creeping fluid' the deviatoric stress is related to the strain rate, rather than to the deviatoric strain as in elasticity. Furthermore, viscosity is replaced by shear modulus.

The creep law (Eqn. (3.19)) can be expanded as follows, which again makes use of engineering shear strain.

$$\dot{\boldsymbol{\epsilon}}^c = \begin{pmatrix} \dot{\epsilon}_{xx}^c \\ \dot{\epsilon}_{yy}^c \\ \dot{\epsilon}_{zz}^c \\ \dot{\gamma}_{xy}^c \end{pmatrix} = \frac{1}{2\mu}\begin{bmatrix} 1 & 0 & 0 & 0 \\ 0 & 1 & 0 & 0 \\ 0 & 0 & 1 & 0 \\ 0 & 0 & 0 & 2 \end{bmatrix}\begin{pmatrix} S_{xx} \\ S_{yy} \\ S_{zz} \\ S_{xy} \end{pmatrix} \text{ OR } = \frac{1}{2\mu}\begin{bmatrix} \frac{2}{3} & \frac{-1}{3} & \frac{-1}{3} & 0 \\ \frac{-1}{3} & \frac{2}{3} & \frac{-1}{3} & 0 \\ \frac{-1}{3} & \frac{-1}{3} & \frac{2}{3} & 0 \\ 0 & 0 & 0 & 2 \end{bmatrix}\begin{pmatrix} \sigma_{xx} \\ \sigma_{yy} \\ \sigma_{zz} \\ \sigma_{xy} \end{pmatrix} \tag{3.21}$$

As this creep law is incompressible, locking and spurious pressure distributions are expected. In order to help mitigate this problem, a little artificial

compressibility ($\nu = 0.4995$, opposed to $\nu = 0.5$) is induced into the algorithm. Borrowing from elasticity, the creep law is written as

$$\begin{pmatrix} \dot{\epsilon}^c_{xx} \\ \dot{\epsilon}^c_{yy} \\ \dot{\epsilon}^c_{zz} \\ \dot{\gamma}^c_{xy} \end{pmatrix} = \frac{1}{2\mu(1+\nu_c)} \begin{bmatrix} 1 & -\nu_c & -\nu_c & 0 \\ -\nu_c & 1 & -\nu_c & 0 \\ -\nu_c & -\nu_c & 1 & 0 \\ 0 & 0 & 0 & 2(1+\nu_c) \end{bmatrix} \begin{pmatrix} \sigma_{xx} \\ \sigma_{yy} \\ \sigma_{zz} \\ \sigma_{xy} \end{pmatrix} \tag{3.22}$$

with Poisson's ratio $v_c \to 0.5$, which implies incompressible behaviour. Equation (3.22) is obtained by recognizing the similarities between the creep law and fluid flow equations, which was alluded to in Eqn. (crplw). As the formulation is plane strain, total strain out of plane must remain equal to zero,($\dot{\epsilon}_{zz} = \dot{\epsilon}^e_{zz} + \dot{\epsilon}^c_{zz} = 0$), as steady state is approached $\dot{\epsilon}^e_{zz} \to -\dot{\epsilon}^c_{zz}$.

The emphasis of this section has been on the relations of creep strain rate to stress. Next, the method of successive approximations is presented.

The Method of Successive Approximations

The method of successive approximations (MSA) [30, 18] assumes that given a reasonable starting point, one can iterate to a unique flow solution. When using the MSA, Eqn. (3.1) it is assumed that $\rho\ddot{\mathbf{u}} \approx 0$. To obtain the discretized momentum equation a Galerkin method was used. The gradient term was then integrated by parts, and the displacement field approximated as $\mathbf{u} = \mathbf{Na}$. These operations are summarized as follows:

$$\int_V \delta u^T \mathbf{L}^T \boldsymbol{\sigma} dV + \int_V \delta u \mathbf{b} dV = 0$$
$$\int_V \delta \epsilon^T \boldsymbol{\sigma} dV - \int_S \delta u^T \cdot \mathbf{t}_n dS - \int_V \delta u^T \mathbf{b} dV = 0$$

where $\mathbf{t}_n$ contains the surface tractions. Given the following substitutions

$$\delta u^T \rightarrow \mathbf{N}^T; \delta \epsilon^T \rightarrow \mathbf{B}^T$$

the final form is

$$\mathbf{K}\Delta\mathbf{a} = \mathbf{F} - \int \mathbf{B}^T \boldsymbol{\sigma} dV + \int \mathbf{B}^T \mathbf{D} \Delta \boldsymbol{\epsilon}^c dV \tag{3.23}$$

with $\mathbf{B} = \mathbf{LN}$, $\mathbf{K} = \int_V \mathbf{B}^T \mathbf{D}^e \mathbf{B} dV$, $\mathbf{F} = \int_V \mathbf{N}^T \mathbf{b} dV + \int_S \mathbf{N}^T \sigma_n$ dS, vector $\Delta\mathbf{a} = \mathbf{a}_{n+1} - \mathbf{a}_n$ contains the nodal displacement increments, with "n" being the time step counter. As the residual load ($\mathbf{R} = \mathbf{F} - \int \mathbf{B}^T \boldsymbol{\sigma} dV$) eventually approaches zero, this implies that any subsequent displacement increments ($\Delta\mathbf{a}$) are caused solely by creep. It should be noted that an explicit approximation is used where $\Delta\epsilon^c = \dot{\epsilon}^c \Delta t$, with Δt being the time increment.

As the equilibrium equation has been discretized, a suitable time increment is needed for the time marching scheme. Given that explicit time marching schemes are conditionally stable [31], the time step for each iteration, as presented by Killeavy [18], is given by

$$\Delta t = \alpha \frac{\sigma_e}{\dot{\epsilon}_e^c} \frac{4\,(1+\nu)}{3nE} \tag{3.24}$$

where factor $\alpha < 1$ is introduced into Eqn. (3.24) to increase the quality of solution, as well as the numerical stability. After the time step and the creep strain increments are calculated, the constitutive relation is applied as $\Delta\boldsymbol{\sigma} = \mathbf{D}(\Delta\boldsymbol{\epsilon} - \Delta t \dot{\boldsymbol{\epsilon}}^c)$ where $\dot{\boldsymbol{\epsilon}}^c$ is the creep stain rate from Eqn. (3.22), and $\Delta\boldsymbol{\sigma} = \boldsymbol{\sigma}_{n+1} - \boldsymbol{\sigma}_n$. The solution scheme begins with an elastic estimate of stresses and displacements. With the initial elastic estimate the solution follows the initial strain algorithm presented in Sec. (2.2.1). If the creep strain were

fully incompressible, the volumetric component would be zero; however, as compressibility to the creep strain has been introduced, the total volumetric strain ($\epsilon_v = \epsilon_v^e + \epsilon_v^c \neq 0$).

This algorithm is based on full matrix solutions, which are solved by decomposing the global stiffness matrix using the Cholesky method. To relax the penalty associated with incompressibility, a smoothening algorithm for volumetric strain is introduced. The smoothening algorithm used has been presented in Sec. (2.1.1).

The next formulation presented will be a matrix free formulation making use of a dynamic algorithm. It provides the foundation for the third formulation, which is identical, with the exception of the addition of dynamic relaxation.

The Central Difference Scheme

The central difference scheme is obtained by applying a Galerkin procedure to the momentum balance equation. The sequence of operations follows

$$\int_V \delta u \rho \ddot{\mathbf{u}} dV = \int_V \delta u \left(\mathbf{L}^T \boldsymbol{\sigma} + \mathbf{b} \right) dV$$
$$\int_V \delta u \rho \ddot{\mathbf{u}} dV = \int_S \delta u^T \cdot \mathbf{t}_n dS + \int_V \delta u^T \mathbf{b} dV - \int_V \delta \epsilon^T \boldsymbol{\sigma} dV$$
$$\int_V \mathbf{N}^T \rho \mathbf{N} \ddot{\mathbf{a}} dV = \mathbf{F} - \int_V \mathbf{B}^T \boldsymbol{\sigma} dV$$

$$\mathbf{M} \frac{\Delta \dot{\mathbf{a}}}{\Delta t} = \mathbf{F}^{ext} - \mathbf{F}^{int} \tag{3.25}$$

in which $\mathbf{M} = \int_V \mathbf{N}^T \rho \mathbf{N} dV$ is the mass matrix, $\dot{\mathbf{a}} = \frac{d\mathbf{a}}{dt}$ is the nodal velocity vector, $\mathbf{F}^{ext}$ is the external force vector containing body forces and tractions and is synonymous with $\mathbf{F}$ presented in the previous section, and $\mathbf{F}^{int} = \int_V \mathbf{B}^T \boldsymbol{\sigma} dV$

is the internal force vector which is adjusted based on the creep strains. Since an explicit time marching scheme is adopted, a lumped mass version for $\mathbf{M}$ is used. The updated velocity is given by $\dot{\mathbf{a}}^{n+1} = \dot{\mathbf{a}}^n + \Delta\dot{\mathbf{a}}$. Stresses and displacements are updated similar to what is done for the MSA.

This formulation does not require decomposing the global stiffness matrix. The left hand side of Eqn. (3.25) is a lumped mass, which leads to scalar operations. Stresses are updated on the element level, making use of smoothened volumetric strain rates ($\dot{\boldsymbol{\epsilon}}_v$ and $\dot{\boldsymbol{\epsilon}}_v^c$). Owing to creep being dissipative, no additional damping is required when using this algorithm to suppress reflections from artificial boundaries. The stopping criterion for this formulation is a maximum time, such that $\Delta\dot{a} \to 0$.

The Dynamic Relaxation Scheme

The dynamic relaxation scheme is the same as the central difference algorithm, but the mass is scaled in each element to accelerate the convergence to the steady state solution. The density is adjusted so that the time it takes for the wave to propogate through each element is equal. Referring to the paper by Metzger and Sauvé [34], it is shown

$$v_c = \sqrt{\frac{E_c}{\rho}} = \frac{\beta h}{\Delta t_c} \tag{3.26}$$

$$\rho = \left(\frac{\Delta t_c}{h}\right)^2 \cdot E_c \tag{3.27}$$

where Δt_c is the critical time step, E_c is the constrained modulus, and 'h' is the characteristic length of the element, taken as the smallest altitude of the element. The time step taken is usually smaller than the critical time step, such that $\Delta t = \beta \Delta t_c$, with Δt_c being the critical time step, and $\beta < 1$ is

introduced to improve stability or resolution of the solution.

For the elastic solution, a local damping is used in place of viscous damping, similar to what is used in the commercial program FLAC [5]. This damping effectively reduces the magnitude of the residual load vector during the solving process, and applies loading in the direction opposite to the velocity. The damping is the product of the residual load vector ($\mathbf{R} = \mathbf{F}^{ext} - \mathbf{F}^{int}$), a factor $\alpha < 1$ and the normalized (unit) velocity vector. The algorithm therefore becomes:

$$\mathbf{M}\frac{\Delta\dot{\mathbf{a}}}{\Delta t} = \mathbf{F}^{ext} - \mathbf{F}^{int} - \alpha\mathbf{R}\dot{\mathbf{a}}/ \parallel \dot{\mathbf{a}} \parallel$$

$$\mathbf{M}\frac{\Delta\dot{\mathbf{a}}}{\Delta t} = (1 - \alpha\dot{\mathbf{a}}/ \parallel \dot{\mathbf{a}})\mathbf{R} \tag{3.28}$$

In addition to volumetric strain smoothening presented in the literature review (Sec. (2.1.1)), volumetric creep strains are also smoothened. The results from the creep formulations are presented in the next chapter.

3.2.3 Fractional Step Method

An alternate method for dealing with incompressible flows is presented next. This method is called the fractional step method, or the velocity correction procedure. The fractional step method (FSM) has its origins in fluid mechanics, but was later employed for incompressible solids; see e.g. Zienkiewicz and co-workers [38, 40]. The formulation makes use of the spatial description of equilibrium (Sec. (3.2.1)). This algorithm is not new by any means, variations of it have been readily available in mechanics journals since the early 90's [41, 25, 15]; however, papers continue to be produced on similar algorithms,

which raises questions about where the issues lie. What is most common between algorithms is their use as a transient relaxation tool for attaining a steady state solution. This family of solution techniques uses equal order of interpolation for velocity (displacement) and pressure.

Formulation of the Fractional Step Method

The formulation begins with the momentum equation (Eqn. (3.5)). The moment equation is partitioned to yield a predictor velocity ($\mathbf{v}^*$) which ignores the effect of pressure, and a velocity correction ($\mathbf{v}^c$) that takes into account the effect of pressure on the velocity field. This split in the velocity term is introduced as it circumvents oscillations which are present with a standard Galerkin discretization of the momentum equation. The partitioned equations are as follows:

$$\rho\dot{\mathbf{v}}^* = \mathbf{L}^T\mathbf{S} + \rho\mathbf{g} \tag{3.29}$$

$$\rho\dot{\mathbf{v}}^c = \mathbf{L}^T\mathbf{m}^T p \tag{3.30}$$

With respect to Eqns. (3.29), and (3.30), the partition is defined according to $\Delta\bar{v} = \Delta\bar{v}^c + \Delta\bar{v}^*$, where the bar represents the nodal velocity vector. The sum of the equations returns the momentum equation. Equations (3.29), and (3.30) are then discretized using a Galerkin procedure, where $\mathbf{v} = \mathbf{N}\bar{\mathbf{v}}$ and $\mathbf{p} = \mathbf{N}_p\bar{\mathbf{p}}$. The equations then become

$$\int_V \mathbf{N}^T\rho\mathbf{N}\dot{\bar{\mathbf{v}}}^* dV = \int_V \mathbf{N}^T\left(\mathbf{L}^T\mathbf{S} + \rho\mathbf{g}\right) dV \tag{3.31}$$

$$\int_V \mathbf{N}^T\rho\mathbf{N}\dot{\bar{\mathbf{v}}}^c dV = \int_V \mathbf{N}^T\left(\mathbf{L}^T\mathbf{m}^T p\right) dV \tag{3.32}$$

The terms containing deviatoric stress on the right hand side must be integrated by parts, yielding

$$\mathbf{M}\dot{\bar{\mathbf{v}}}^{*} = \int_{V} \mathbf{N}^{T}\rho\mathbf{g}dV - \int_{S} \mathbf{N}^{T}\cdot\mathbf{t}_{s}dS - \int_{V} \mathbf{B}^{T}\mathbf{S}dV \tag{3.33}$$

$$\mathbf{M}\dot{\bar{\mathbf{v}}}^{c} = \int_{V} \mathbf{N}^{T}\left(\mathbf{L}^{T}\mathbf{m}^{T}\mathbf{p}\right)dV \tag{3.34}$$

in which the mass matrix $\mathbf{M} = \int_{V}\mathbf{N}^{T}\rho\mathbf{N}$, and $\mathbf{t}_{s}$ contains the deviatoric tractions. The body forces and tractions are contained in $\mathbf{F}$, leading to the final form of the equations.

$$\mathbf{M}\frac{\Delta\bar{\mathbf{v}}^{*}}{\Delta t}dV = \mathbf{F} - \int_{V} \mathbf{B}^{T}\mathbf{S}dV \tag{3.35}$$

$$\mathbf{M}\frac{\Delta\bar{\mathbf{v}}^{c}}{\Delta t}dV = \int_{V} \mathbf{N}^{T}\left(\mathbf{L}^{T}\mathbf{m}^{T}\mathbf{p}\right)dV \tag{3.36}$$

To solve the continuity equation an estimation of the velocity field ($\mathbf{v}^{n+1}$) at the end of the time step is required. The continuity equation is discretized using the same procedure as the momentum equations, but with respect to pressure where $\delta p \rightarrow \mathbf{N}_{p}^{T}$.

$$\int_{V} \delta p\frac{1}{\beta^{2}}\dot{\mathbf{p}}\,dV = \int_{V}\left(\delta p\,\rho\frac{\partial\mathbf{v}^{n+1}}{\partial x}\right)dV \tag{3.37}$$

$$\mathbf{M}_{p}\frac{\Delta\bar{\mathbf{p}}}{\Delta t} = \int_{V} \mathbf{N}_{p}^{t}\mathbf{m}^{T}\mathbf{L}\mathbf{v}\,dV \tag{3.38}$$

where the artificial wave speed is introduced as $\beta = 2G/h$, 'h' being the characteristic length of the element [22]. While it is not enough to guarantee stability, the artificial wave speed aids in the convergence of the continuity equation. The introduction of this term nullifies the time-dependant solution,

similar to the introduction of dynamic relaxation. The term on the RHS (Eqn. (3.38)) is the rate of volumetric strain and is simplified as $\dot{\boldsymbol{\epsilon}}_v = \mathbf{m}^T\mathbf{L}\mathbf{v}$.

Next, the velocity at the end of the step as is substituted $\bar{\mathbf{v}}^{n+1} = \bar{\mathbf{v}} + \Delta\bar{\mathbf{v}}$, followed by integrating only the term pertaining to the velocity increment by parts. This integration by parts generates a boundary term with respect to the normal projection of velocity at the face of the element.

$$\mathbf{M}_p \frac{\Delta\bar{\mathbf{p}}}{\Delta t} = \int_V \mathbf{N}_p^T \dot{\boldsymbol{\epsilon}}_v^n \, dV - \int_V \mathbf{B}_p^T (\Delta\mathbf{v}^* + \Delta\mathbf{v}^c) \, dV + \int_S \mathbf{N}_p^T \mathbf{n} \cdot \Delta\mathbf{v} \, dS \quad (3.39)$$

The addition of the velocity correction ($\Delta\mathbf{v}^c$) to the right hand side is beneficial in stabilizing the algorithm. As $\Delta\mathbf{v}^c = \frac{\Delta t_{int}}{\rho}\mathbf{L}^T\mathbf{m}^T\mathbf{p}$, the gradient of the pressure field is introduced to the continuity equation. The effect of the pressure gradient acts to stabilize the pressure equation, and the internal time step (Δt_{int}) further contributes to this. It has been shown by Zienkiewicz and Nithiarasu that the overall stability of the algorithm may be improved by choosing a value of the internal time step equal to double the time step used to calculate the velocity prediction [23]. Referring back to the section on justification for equal order of interpolation (Sec. (2.3.2)), this term is the additional term on the diagonal that introduces algorithmic compressibility.

The boundary term generated can be neglected in special cases. According to Nithiarasu, the term can be neglected when an 'appropriate' initial pressure field is provided [22]. This term will also be equal to zero when steady state is reached, as the velocity increment approaches zero through iteration. The final justification for neglecting this term in steady state analysis is shown in Fig. 3.1. When solving the boundary between elements, the effects of the projection will cancel out, but the term remains on the outside surface. In order to supply an 'appropriate' pressure field, the elastic pressure field was

calculated to provide initial values for the pressure degrees of freedom..

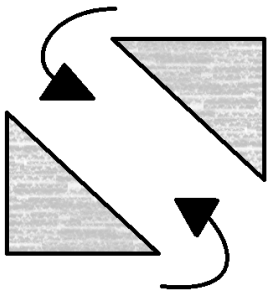

Figure 3.1: Figure illustrated when computing the surface integral, projections will be equal and opposite between adjoining elements.

Once the continuity equation is solved, the resulting change in pressure is used to update the pressure field as $\bar{\mathbf{p}}^{n+1} = \bar{\mathbf{p}}^{n} + \Delta\bar{\mathbf{p}}$.

Breakdown of Algorithm

The algorithm used in this analysis is as follows:

Step 1:

$$\mathbf{M}\Delta\bar{\mathbf{v}}^{*} = \Delta t \left[\mathbf{F} - \int \mathbf{B}^{T}\mathbf{S}dV\right] \tag{3.40}$$

The first step is to calculate $\mathbf{v}^{*} = \mathbf{v}_{n} + \Delta\mathbf{v}^{*}$.

Step 2:

$$\mathbf{M}_{p}\Delta\bar{\mathbf{p}} = \Delta t \left[\int \mathbf{N}_{p}^{T}\dot{\boldsymbol{\epsilon}}_{v}^{n} + \int \mathbf{B}_{b}^{T}(\Delta\mathbf{v}^{*} + \Delta\mathbf{v}^{c})\right] dV \tag{3.41}$$

$$\bar{\mathbf{p}}^{n+1} = \bar{\mathbf{p}}^{n} + \Delta\bar{\mathbf{p}} \tag{3.42}$$

The influence of the pressure gradient is introduced to the continuity equation through the velocity correction term. The velocity correction ($\mathbf{v}^{c}$) from the previous time step is added to this to give the total velocity increment for calculation in the continuity equation.

Step 3:

$$\Delta\bar{\mathbf{v}} = \Delta\bar{\mathbf{v}}^* + \mathbf{M}^{-1}\left(\int_V \Delta t \mathbf{B}^T \mathbf{m}^T \bar{\mathbf{p}}^{n+1} dV\right) \tag{3.43}$$

$$\bar{\mathbf{v}}^{n+1} = \bar{\mathbf{v}}^n + \Delta\bar{\mathbf{v}} \tag{3.44}$$

The final step uses the updated pressure field to calculate the velocity correction term. The velocity can be updated, and the process is repeated starting at Step 1 until convergence is achieved. Change of velocity is used as the stopping criterion for this algorithm.

The interest in this analysis is the velocity at steady state, not the change in velocity. While it is not necessary to use the updated pressure to calculate the velocity correction, it allows the program to converge faster. If this step is neglected, the velocity correction is effectively one step behind, but the final converged solution is nearly identical.

Chapter 4

Test Problems for Incompressible Simulations

4.1 The Double Slope

The first test problem presented is the double slope shown in Fig. 4.1. It that has been analysed in detail by Killeavy [18]. Two meshes were used: 48 elements and 35 nodes referred to as the coarse mesh; and 192 elements and 117 nodes referred to as the fine mesh. The measure of coarse and fine in this case was relative. The slope is assumed to creep with a Newtonian flow rule (constant viscosity) due to a unit weight of 10 $\mathrm{kN{\cdot}m^{-3}}$. A benchmark solution was established using a 6-noded triangular element, with straight edges. The main comparison used was the calculation of horizontal velocity at the crest of the slope. This value was found to be approximately 6 $\mathrm{m{\cdot}a^{-1}}$ (meters per annum), as shown in Fig. 4.2, measured at B in Fig. 4.1. A creep constant of $A = 0.001$ $\mathrm{kPa^{-1}yr^{-1}}$ is used along with $n = 1$, and the elastic modulus is 1×10^6 kPa. When performing simulations with the FSM, a viscosity of $\mu = 333$ kPa·s is assumed, as it corresponds to the viscosity of the creep flow

in the other algorithms. No external point loads or tractions are applied. The left boundary corresponds to a divide, so the shear traction is equal to zero, and the horizontal velocity has a zero value. The convergence of pressure is monitored near the base of the divide, at Point A. The base of the slope is fully fixed. Figure 4.1 shows the expected pressure distribution, obtained from a 6 noded analysis using a coarse grid (drawn as 3 noded elements), with Fig. 4.2 providing the horizontal velocity history at B. The scale on the right hand side of this diagram is the scale used for all results in this section. For the pressure plots of mean stress a compression positive scheme is adopted. The measure of mean stress used is the center of the Mohr circle $(-(\sigma_x + \sigma_y)/2)$. The scale is from -50 kPa mean stress (tension) to 450 kPa mean stress (compression).

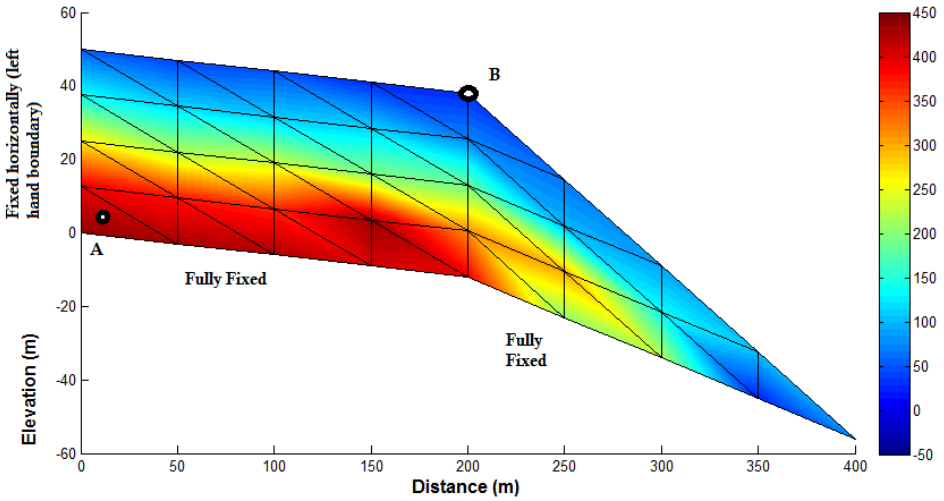

Figure 4.1: Pressure distribution for double slope using 6 noded analysis with 48 elements and 117 nodes

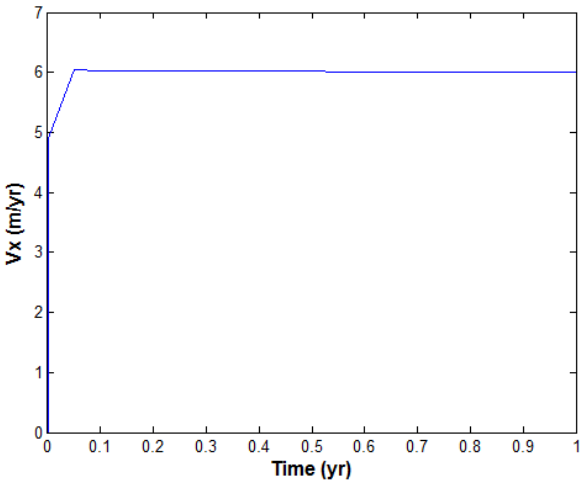

Figure 4.2: Velocity history for 6 noded element analysis

Referring to Fig. 4.3 and the legend, the first letter corresponds to mesh (C - coarse, F - fine), the second to smoothing (NS - not smoothened, S - smoothened), and the final letter implies compressibility (IC - incompressible, C- slightly compressible). The meaning of slightly compressible is $\nu = 0.4995$. For example C-NS-C denotes a coarse mesh that did not use smoothening and is slightly compressible. For the DR there are 2 variables, mesh density (C or F) and compressibility (IC or C); the FSM has only mesh density as a variable (C or F). The same convention is used for the pressure history plots. These parameters encompass the array of analysis conducted and allow the changing variables to be tracked in a systematic way. The steady-state velocities of the problem solved using the formulations are presented in Chapter 3.

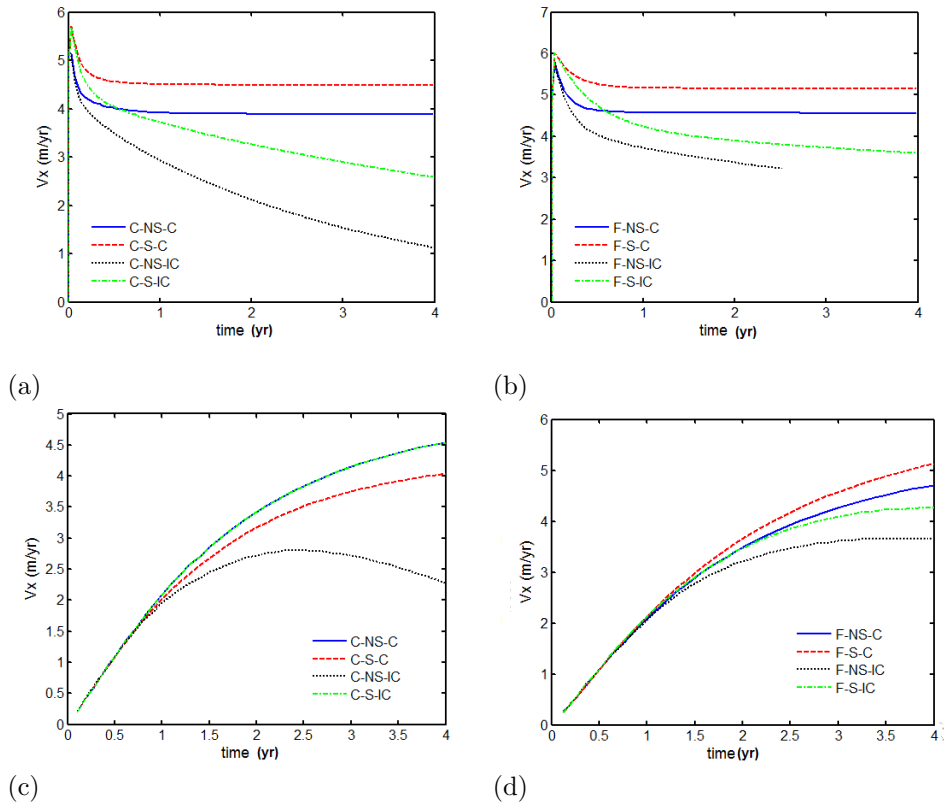

Figure 4.3: Velocity histories a) MSA, coarse mesh b) MSA, fine mesh c) CDS, coarse mesh d)CDS, fine mesh

Figures 4.3a and 4.3b show that for the method of successive approximations (MSA), the predictions for simulations incorporating slight compressibility begin close to the target value, and decrease before stabilizing. Those that have no compressibility do not converge. As one might expect, the velocities for the finer mesh are higher and smoothening helps in reducing locking. It was noted that the solution approached the 6-noded solution as enchancement was added. Looking at the same results from the central difference scheme (CDS) (Figs. 4.3c and 4.3d), the steady-state velocities are approached from below and do not fully converge. The velocities are approached from below, given that load is increased incrementally throughout the analysis.

Locking is evident, given the decreasing velocities, particularly for the

MSA simulations that are fully incompressible. The results obtained from both methods allowing for compressibility are similar and are acceptable solutions. The best results are obtained from the smoothened fine mesh that is slightly compressible (F-S-C). These results demonstrate that in order to get acceptable results, the following is required: smoothing, slight compressibility, and a sufficiently fine mesh.

With respect to dynamic relaxation (DR) and fraction step method (FSM), the velocities converge to a value closer to 6 , as shown in Figs. 4.4a and 4.4b. Both predictions show some oscillation before convergence, with the DR code showing heavier oscillations. Both programs converge readily. Mesh density and incompressibility have less influence using DR and FSM formulations, at least for the problem analysed. It should be noted that for these two algorithms the time actually acts as an iteration counter.

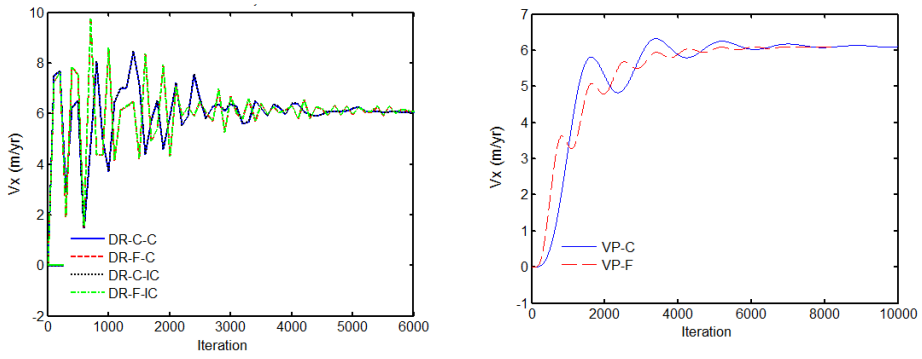

(a) (b)

Figure 4.4: Velocity histories a) DR, coarse and fine b) FSM, coarse and fine mesh

Looking at the pressure histories (Figs. 4.5, and 4.6), the convergence trends are very similar to the velocity histories. The only exceptions are that heavy oscillation is prominent in the predictions of the CDS pressure histories

(Figs. 4.5c and 4.5d), and that the DR-C-C solution (Fig. 4.6a) does not appear to be stabilizing, contrary to other DR simulations. The MSA and CDS figures also have negative pressures on the coarse grid and positive on the fine grid, which suggests spurious pressure distributions. There was no change in the output at the time of simulations, and it follows that the element in question was showing signs of a spurious pressure distribution. The incompressible solutions for the MSA and CDS (Fig. 4.5) did not converge, but rather deviated from the steady state solution obtained by the 6-noded element. While the pressures approach the solution incrementally in the MSA, CDS and DR algorithms, the FSM seems to oscillate around the final value. The pressures attained using linear elements are higher than the 6-noded element solution, as a very coarse grid was used during the 6-noded simulation. The fact that pressure predictions do not necessarily correspond to what might be expected, yet the velocities are reasonable, is due to creep being largely independent of pressure.

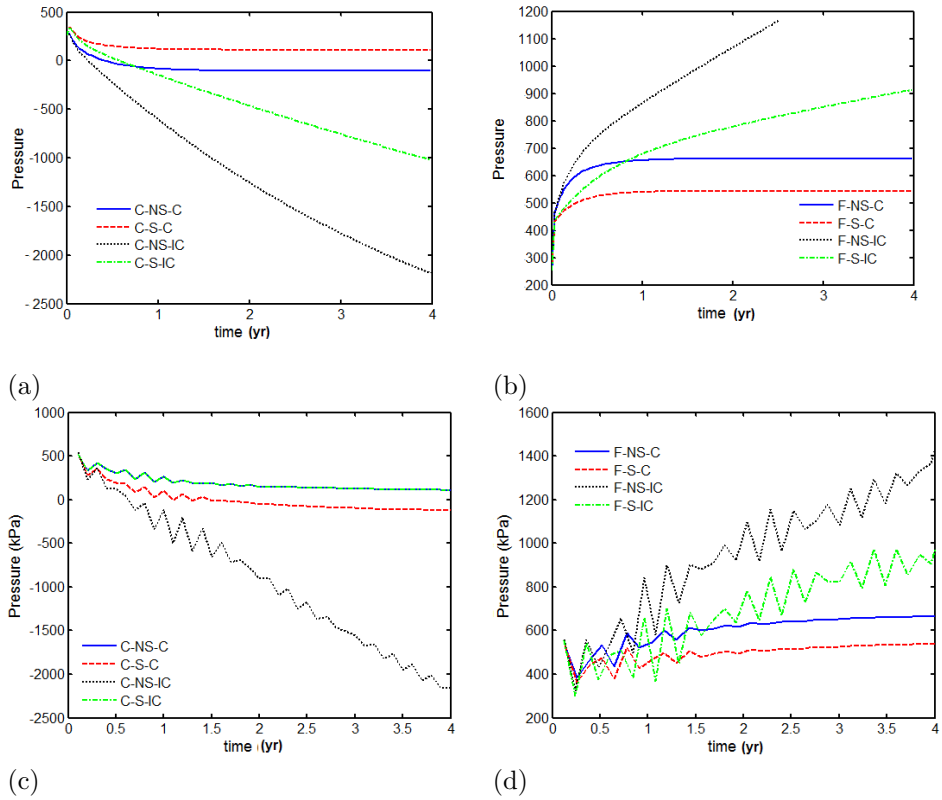

Figure 4.5: Convergence of pressure histories a) MSA, coarse mesh b) MSA, fine mesh c) CDS, coarse mesh d)CDS, fine mesh

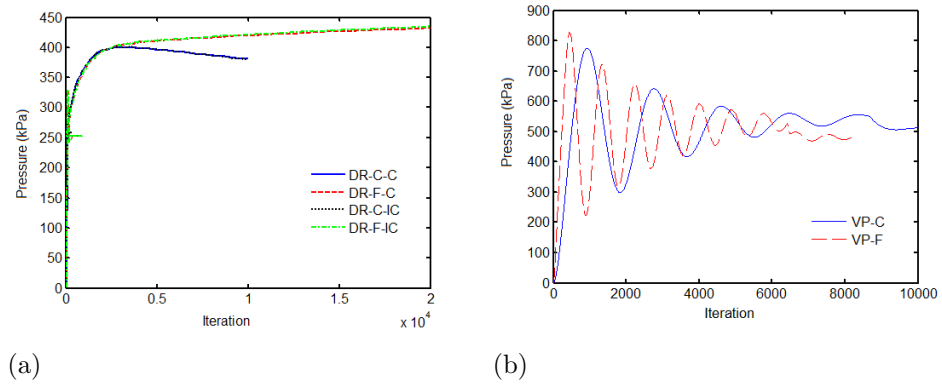

Figure 4.6: Convergence of pressure histories a) DR, coarse and fine b) FSM, coarse and fine mesh

The pressure plots for both the MSA and CDS display a large amount of checker boarding (Figs. 4.7 and 4.9, showing worst and best for each case). The incompressible solutions possess checker boarding to a greater extent, as

is expected. When comparing the not smoothened solutions to the smoothened solutions, the level of checker boarding is reduced, but the problem is not eliminated. These pressure plots do not make physical sense, with large, inconsistent jumps in the pressure from element to element. The solutions provided by both the DR and FSM programs are by contrast very good (Figs. 4.8 and 4.10, incompressible DR plots are omitted as they are identical to the compressible ones). Both algorithms provide a rational pressure field, which increases with depth. There are discontinuities between elements, but that is due to using constant stress elements in the formulation. The DR results (Fig. 4.12a) have slight tensile (suction) pressures on the surface, which could be caused by horizontal movement. The pressure fields obtained from the DR and FSM are of much higher quality than those of the MSA or CDS. The DR and FSM plots do not have spurious pressure distributions ("checker boarding"), unlike those predicted by the other creep formulations.

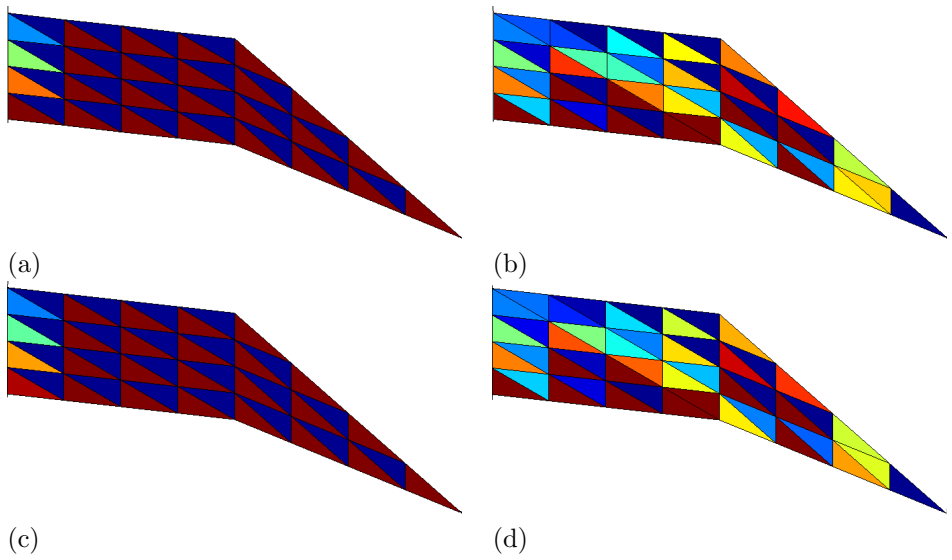

Figure 4.7: Pressure fields for coarse double slope smoothing a) MSA, incompressible, not smoothened b) MSA, slightly compressible, smoothened c) CDS, incompressible, not smoothened d) CDS, slightly compressible, smoothened

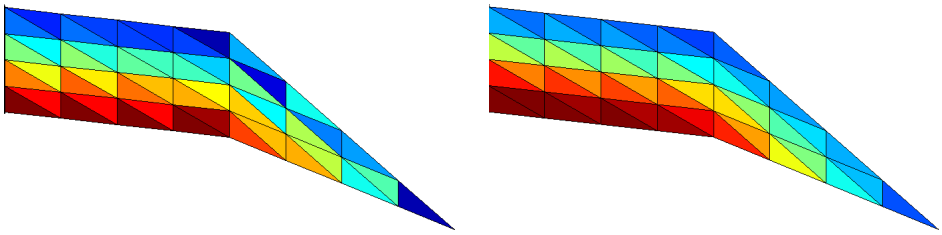

(a) (b)

Figure 4.8: Pressure fields for coarse double slope a) DR, slightly compressible b) FSM, slightly compressible

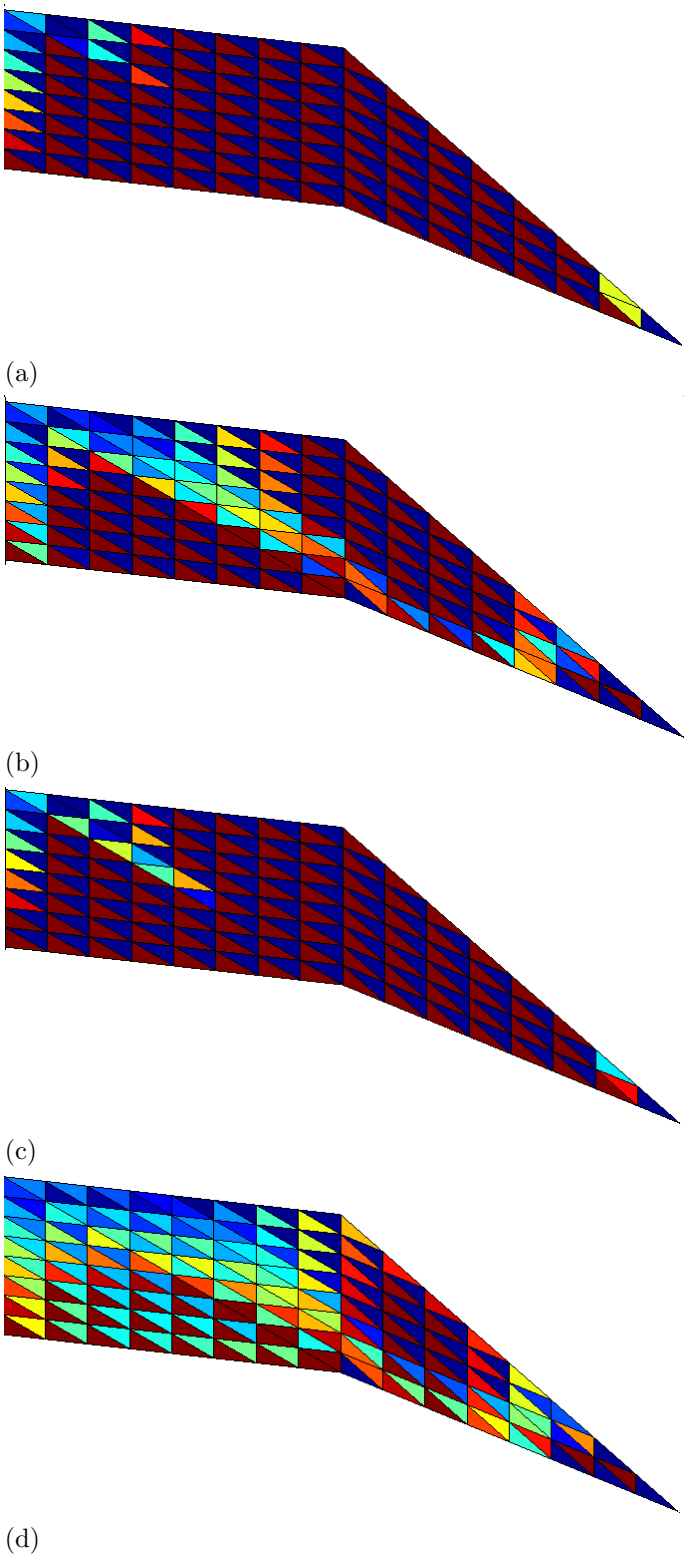

Figure 4.9: Pressure fields for fine double slope a) MSA, incompressible, not smoothened b) MSA, slightly compressible, smoothened c) CDS, incompressible, not smoothened d) CDS, slightly compressible, smoothened

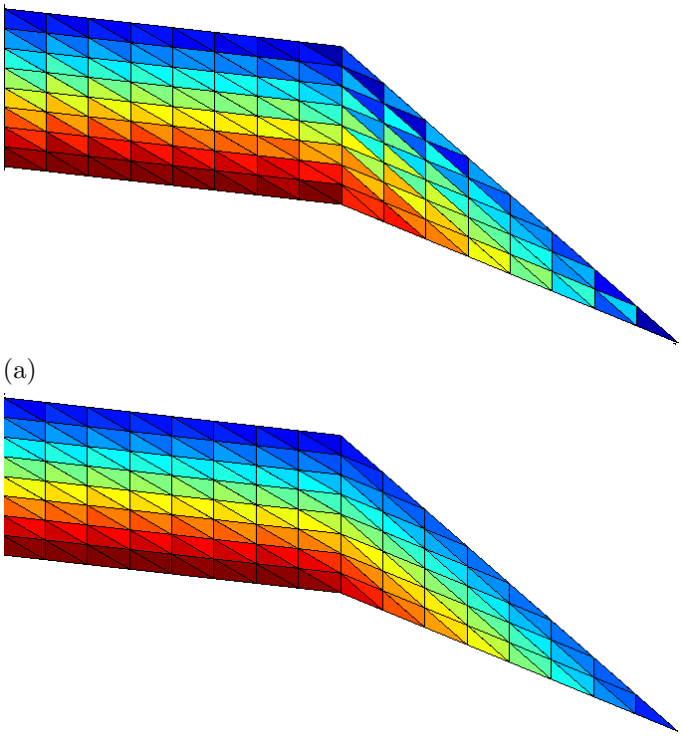

Figure 4.10: Pressure fields a) DR, slightly compressible b) FSM, slightly compressible

To illustrate what is commonly encountered in typical commercial output, least squares smoothened pressure fields, where the smoothening is done after simulation is completed, are shown in Figs. 4.11a, and 4.11b, corresponding to Fig. 4.9a and Fig. 4.9b, respectively. Note the few odd inconsistencies in both figures, such as the line of high compression propagating to the surface from the left of break in the slope, the stress nearing tension 1 element under the surface right of the break, and the drastic increase in tension nearing the tip. Figure 4.11a shows moderate stress throughout the depth with a sudden increase at the fixed boundary, while Fig. 4.11b, inconsistencies aside, shows a distribution close to what would be expected. As figures 4.11a, and 4.11b were generated based on checker boarded results, care must be exercised when interpreting smoothened results. Locally elements are not necessarily in equilibrium as the

equations of motion are satisfied globally. Thus, although large jumps can be observed from element to element (local level), these are eliminated on a global level when processing the predictions using a least squares smoothening.

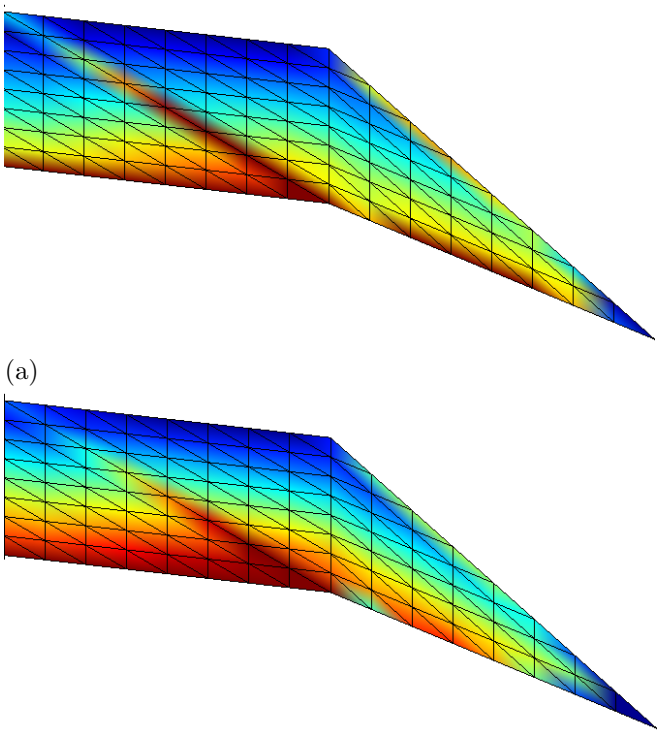

Figure 4.11: Least squares post analysis smoothened pressure plots using the MSA a) incompressible, not smoothened b) slightly compressible, smoothened

Given that the pressure distributions corresponding to 4 years were poor for the MSA and CDS programs, this raises the question: are the pressure field predictions more reasonable if the 1 year values are selected as representative of steady-state? Figure 4.12 shows two plots, with the shorter analysis showing slight reductions in the amount of checker boarding. The maximum pressure in the 1 year plot was 671 kPa, in the 4 year plot it was 808 kPa, which suggests that drifting may occur after steady-state is attained due to insensitivity of creep to pressure. The influence of simulation time will be thoroughly investigated in Chapter 6.

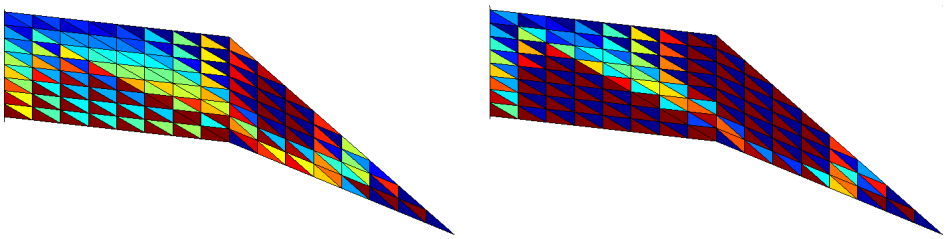

(a) (b)

Figure 4.12: Pressure fields for fine double slope a) 1 year simulation b) 4 year simulation

4.1.1 Final comments on the Double Slope problem

To begin a direct comparison of performance, it is prudent to also address computational effort required to arrive at a steady-state solution. When performing simulations, it was found that the CDS was by far the slowest. Given the quality of solution, this algorithm can be discounted. The dynamic relaxation (DR) and MSA arrived at a steady-state with no noticeable difference in computation time, but the DR scheme provided a better solution. The FSM executed the fastest, and provided a solution on par with that of the DR scheme. It should be noted that there were occasional difficulties in the FSM algorithm. Obtaining a solution took trial and error with regard to choice of time step. Without a benchmark problem this would contribute to uncertainty with regards to the reliability of predictions.

When looking at velocity, the determination of a good solution is fairly straight forward, due to having the benchmark solution of 6 $m \cdot a^{-1}$. Although the MSA converged readily, the velocity was calculated, under best circumstances, at 5.16 $m \cdot a^{-1}$. The CDS provides roughly the same solution as the MSA at 5.13 $m \cdot a^{-1}$, but had a greater computation time. The DR and FSM both readily converge to a value that for all effective purposes is equal to the bench mark.

With respect to pressure distributions, the only programs that were free of checker boarding were the DR and FSM schemes. The FSM provided a slightly better pressure plot, with a much smaller tensile stress at the surface. The linear pressure interpolation of the FSM provided less improvement of pressure distribution when mesh density was increased, with the coarse mesh providing a pressure distribution nearly equal to that of the fine mesh DR simulation.

The best results were provided by the FSM for this particular test problem, followed by the DR program. The CDS lacked in both quality of solution and computational time and will not be considered any further for this study.

4.2 Couette Flow Problem

Couette flow, flow of a fluid between two plates, is pressure driven, but is entirely shear flow. The material is typically assumed to be fully incompressible. Although sliding of the plate along the upper boundary for the case studied was suppressed, a pressure gradient was applied to the fluid through a left side compressive traction of 4 kPa, and a right side compressive traction of 2 kPa. An elastic modulus of $E = 10000$ kPa, Poisson's ratio of $\nu = 0.3$ and $A = 0.6\bar{6}$ were used. The effects of gravity are ignored for the purpose of this problem. As the domain is 1m wide, it can be expected that the horizontal velocity at half of the width will be equal to 0.25 $\mathrm{m{\cdot}s^{-1}}$, assuming a unit viscosity. The mesh consisted of 400 elements and 231 nodes. Smoothening routines were used to attain the best possible solution.

Initially all programs returned a velocity of 0.259 $\mathrm{m{\cdot}s^{-1}}$, which is greater than expected, varying about 5% from the closed-form solution. The cause of this discrepancy was found to be the slight compressibility used to ensure

stability within each of these algorithms (MSA, DR, and FSM). When the DR or MSA were made to be fully incompressible, the expected result of 0.25 $m \cdot s^{-1}$ was obtained; however, they were much less efficient when executed, showing an increase in computational effort.

The other important feature of the Couette flow is the proper identification of the pressure gradient, which should be evenly distributed from 4 kPa to 2 kPa within the fluid. Aside from slight boundary issues at the edges, this was captured by all algorithms. The parabolic deformation/velocity was also captured. Pressure plots shown in Figs. 4.13, 4.14, and 4.15, have a range from 4 kPa (red) to 2 kPa (blue), with the velocity profiles (which match the closed form solution).

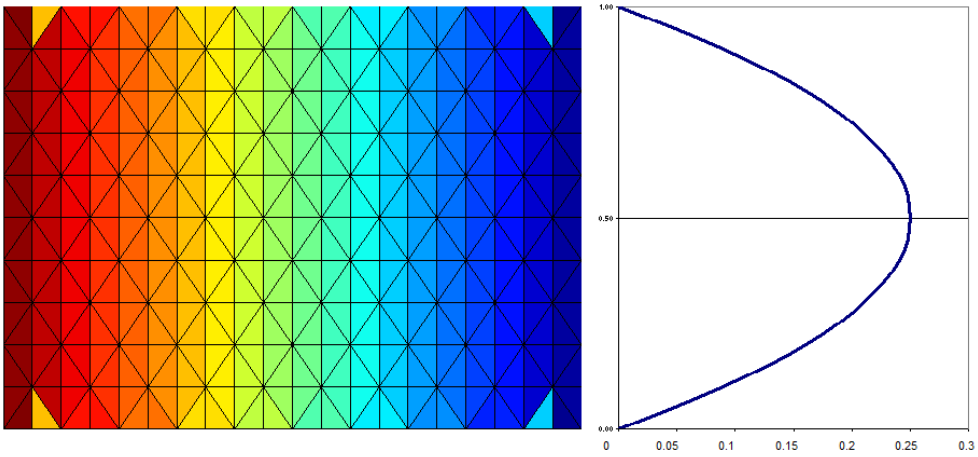

Figure 4.13: Pressure distribution and velocity profile for the MSA in Couette flow

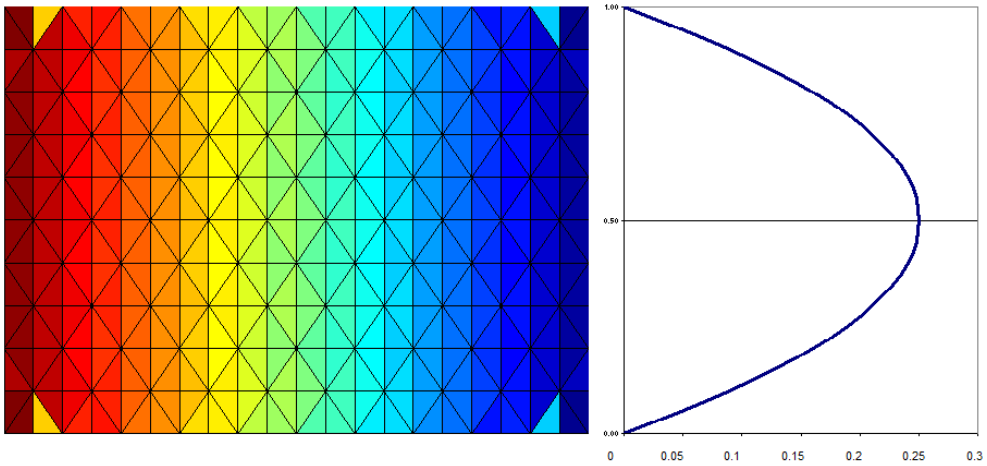

Figure 4.14: Pressure distribution and velocity profile for the DR in Couette flow

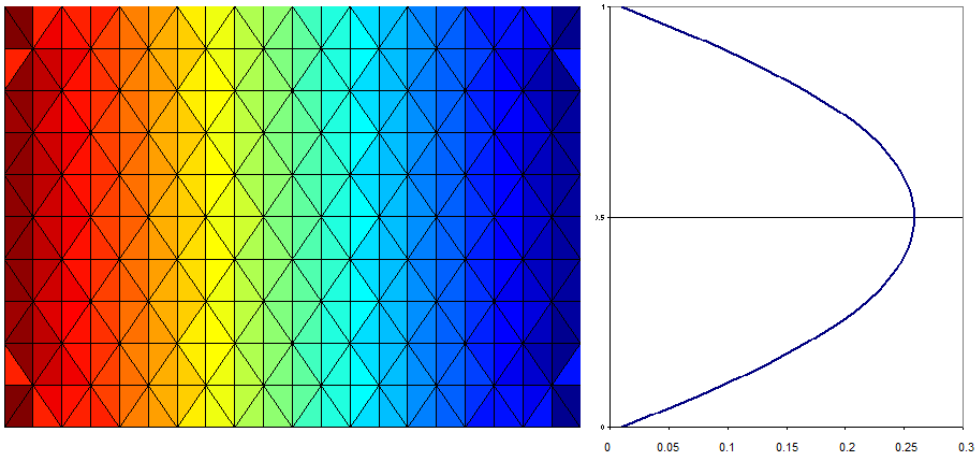

Figure 4.15: Pressure distribution and velocity profile for the FSM in Couette flow

Chapter 5

An Alternative Creep Formulation

5.1 Rationale

Although the creep algorithm presented in the earlier chapter is sufficient for many problems, it can be improved in a few aspects. The previous algorithm worked poorly when the problem was assumed to be fully incompressible. Slight compressibility was required to ensure that the method would provide more reasonable predictions. Such compressibility introduced errors into the solution of the Couette flow problem. Another issue was the use of an explicit algorithm. The algorithm was used as it was easy to implement, but the solution was found to be sensitive to the time step adopted. The time steps had to be small and any deviation could cause the algorithm to quickly become unstable. For many problems, creep analysis could benefit from not being constrained in the choice of time step, to allow acquisition of a reasonable steady-state solution with much smaller computational cost. With this goal in mind, a new algorithm was devised by borrowing from a radial return

plasticity approach.

5.2 Radial Return Creep Formulation

Since creep is independent of the third stress invariant and incompressible, the stress–strain rate law can be formulated in terms of the invariants p and σ_e that represent the spherical and deviatoric stresses, and the strain rate invariants $\dot{\epsilon_v}$ and $\dot{\epsilon_e}$ that represent the volumetric and deviatoric strain rates, respectively. Using these invariants the stress–strain law, in invariant form, becomes

$$\begin{Bmatrix} \Delta p \\ \Delta \sigma_e \end{Bmatrix} = \begin{bmatrix} K & 0 \\ 0 & 3G \end{bmatrix} \begin{Bmatrix} \Delta\epsilon_v - \cancelto{0}{\Delta\epsilon_v^c} \\ \Delta\epsilon_e - \Delta\epsilon_e^c \end{Bmatrix} \tag{5.1}$$

in which K and G are the bulk and shear moduli, respectively. The volumetric creep strain rate is zero in this formulation, as the creep flow is fully incompressible. Having established the stress increments at a given iteration, the total stresses during an iteration are defined as

$$p = p_0 + K\Delta\epsilon_v \tag{5.2}$$

$$\sigma_e = \sigma_{e0} + 3G(\Delta\epsilon_e - \Delta\epsilon_e^c) \tag{5.3}$$

in which the subscript '0' implies initial value. As the method of successive approximations is being used, the creep analysis begins with the elastic predictor stresses

$$p^* = p_0 + K\Delta\epsilon_v \tag{5.4}$$

$$\sigma_e^* = \sigma_{e0} + 3G\Delta\epsilon_e \tag{5.5}$$

in which the superscript '$*$' denotes a predictor value. One observes that pressure remains at the predictor value within a time step (Eqn. (5.5)). The stress at the end of the increment therefore becomes

$$p = p^* \tag{5.6}$$

$$\sigma_e = \sigma_e^* - 3G\Delta\epsilon_e^c \tag{5.7}$$

In the traditional initial strain algorithm $\Delta\boldsymbol{\epsilon}^c$ is calculated using the stresses at the beginning of the time step. Given the simplified form of Eqn. (5.7), the creep strain increment can also be estimated using σ_e at the end of a time step, thus after introducing the creep law it may be shown that

$$F = \sigma_e - \sigma_e^* + 3G\Delta t A\sigma_e^n = 0 \tag{5.8}$$

which reduces to a 'root finding' exercise. Using the Newton-Raphson method to find the root of Eqn. (5.8), it was shown that

$$(\sigma_e)_{m+1} = (\sigma_e)_m - \frac{F_m}{(\frac{dF}{d\sigma_e})_m} \tag{5.9}$$

$$F' = \frac{dF}{d\sigma_e} = 3G\Delta t A n\sigma_e^{n-1} + 1 \quad \Rightarrow \quad 3G\Delta t A n\frac{\dot{\epsilon}_e^c}{\sigma_e} + 1 \tag{5.10}$$

in which 'm' is an iteration counter. Looking at Eqn. (5.10) one observes that if σ_e is equal to zero, $F' = 1$. Thus, one does not need need to worry about dividing by zero when employing the Newton-Raphson method. Furthermore, creep flow only occurs when $F' > 1$.

Once the converged value for σ_e is obtained, stresses in the Cartesian system are updated by scaling the deviatoric component to arrive at the total stress according to

$$\boldsymbol{\sigma} = p\mathbf{I} + \frac{\sigma_e}{\sigma_e^*}\mathbf{S}^* \tag{5.11}$$

where $\mathbf{S}^*$ corresponds to σ_e^*, and σ_e is the converged value for Eqn. (5.9). By using the stress at the end of a time step to determine the creep rate, the initial strain algorithm must be modified slightly to take this into account, having then the appearance of an initial stress algorithm.

5.2.1 Example solution

Re-evaluating the Couette flow problem with the radial return creep routine, the exact value of maximum velocity is predicted, along with the correct profile. The pressure plot shows the same trends as previous formulations, with an even transition from 4 kPa (red) to 2 kPa (blue). Figures 5.1, and 5.2 show the results from the method of successive approximations (MSA) and dynamic relaxation (DR), respectively.

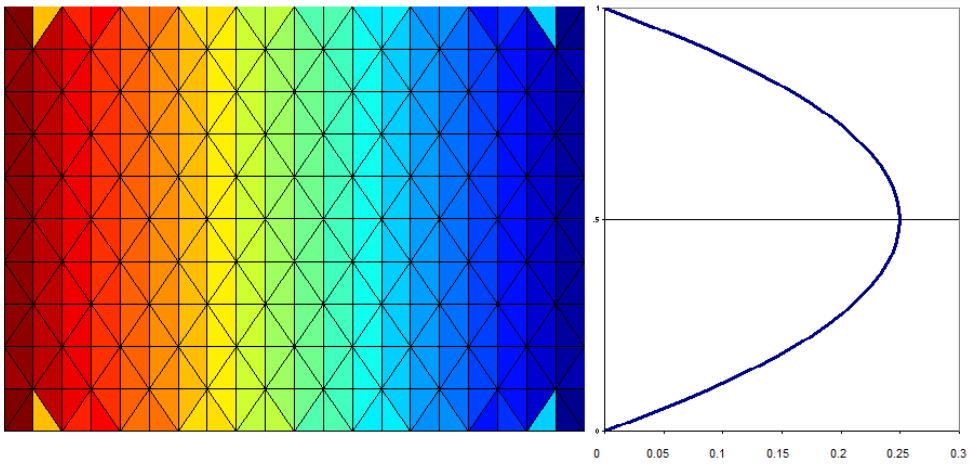

Figure 5.1: Pressure distribution and velocity profile for in Couette flow using MSA with Radial Return Creep

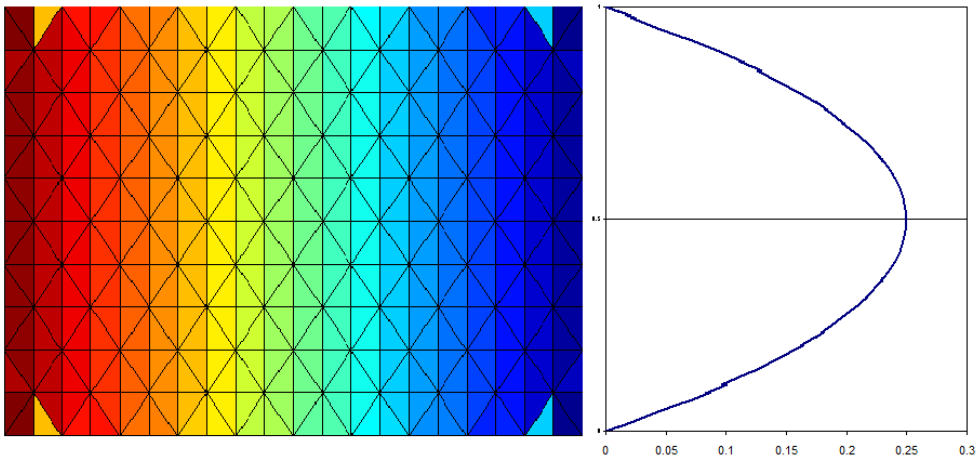

Figure 5.2: Pressure distribution and velocity profile for in Couette flow using DR with Radial Return Creep

The double slope problem, as presented in Sec. (4.1), was also simulated. Results are presented for both the MSA and DR schemes.

MSA Double Slope

Examining the pressure plot (Fig. 5.3), which corresponds to the fine grid, it shows the same "checker boarding" as seen with earlier predictions. When

using post process smoothening, shown in Fig. 5.4, the same anomalies present for the previous MSA formulation were noticed, such as the odd diagonal compression beginning at the break in the slope. The velocity convergence (Fig. 5.5) reaches a maximum velocity, then begins to decrease indefinitely, which is attributed to locking. The final velocity is well below the bench mark of 6 m/a. This is attributed to using the MSA algorithm, and allowing creep to proceed long after the deviatoric stresses, which are responsible for creep, have stabilized to steady-state values. This aspect will be addressed in Chapter 6.

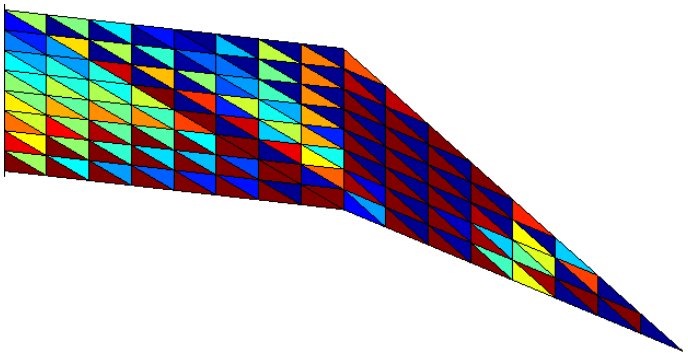

Figure 5.3: Pressure distribution for the double slope (MSA)

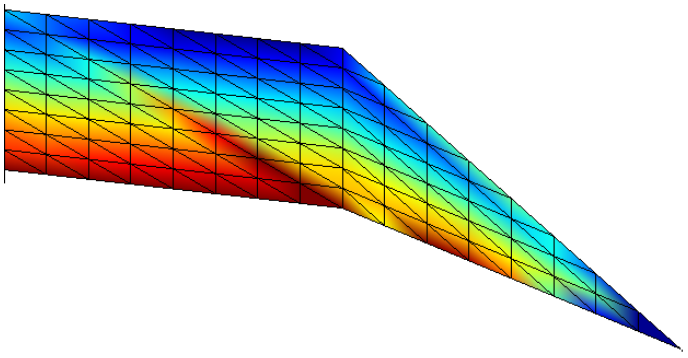

Figure 5.4: Post process smoothened pressure distribution for the double slope (MSA)

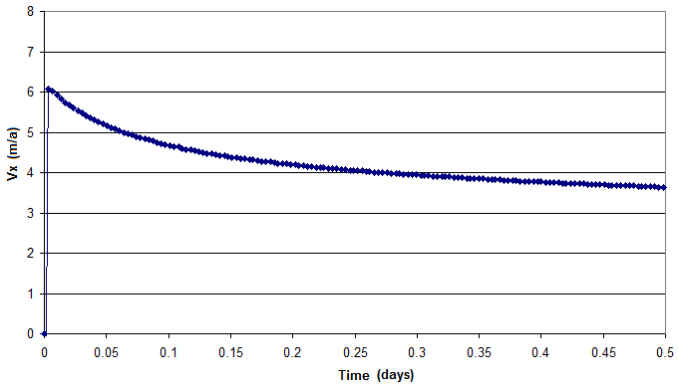

Figure 5.5: Velocity history for the double slope (MSA)

DR Double Slope

The pressure distribution, shown in Fig. 5.6, has very minor checker boarding, but is not free of this defect, as the previous DR algorithm was. This increase in checker boarding may be due to the removal of volumetric creep strain smoothening, which was removed due to incompatibility with the radial return formulation. Figure 5.7 shows the post process smoothened pressure distribution, which is free of the anomalies. The velocity history, shown in Fig. 5.8, converges after several oscillations.

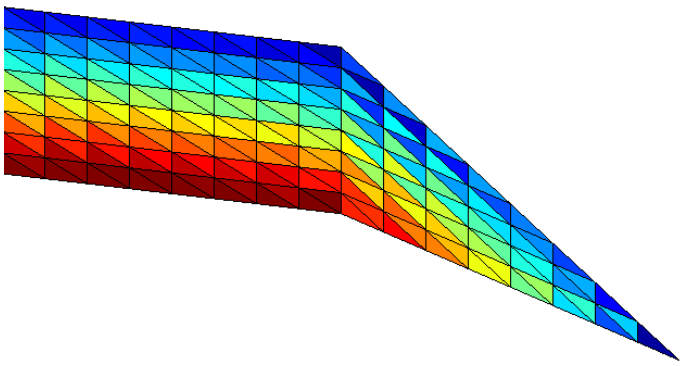

Figure 5.6: Pressure distribution for the double slope (DR)

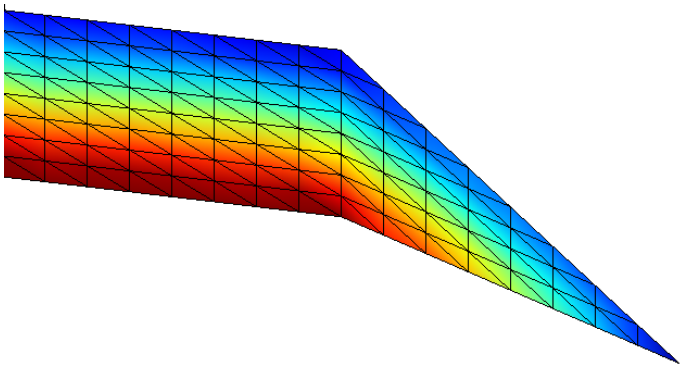

Figure 5.7: Post process smoothened pressure distribution for the double slope (DR)

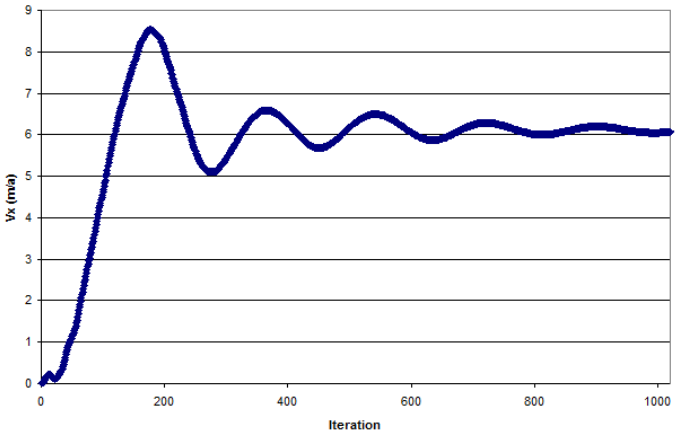

Figure 5.8: Velocity history for the double slope (DR)

5.3 Radial Return Plasticity Variation

Plasticity can be accommodated by making minor changes to the radial return creep routine. This will allow a check to identify areas of material failure yielding within the domain. For plasticity, constitutive law may be written as

$$\Delta\boldsymbol{\sigma} = \mathbf{D}(\Delta\boldsymbol{\epsilon} - \Delta\boldsymbol{\epsilon}^p) \tag{5.12}$$

where $\Delta\boldsymbol{\epsilon}^p$ is the plastic strain increment. When working in invariant space

$$\begin{Bmatrix} \Delta p \\ \Delta\sigma_e \end{Bmatrix} = \begin{bmatrix} K & 0 \\ 0 & 3G \end{bmatrix} \begin{Bmatrix} \Delta\epsilon_v - \cancelto{0}{\Delta\epsilon_v^p} \\ \Delta\epsilon_e - \Delta\epsilon_e^p \end{Bmatrix} \tag{5.13}$$

As the plastic flow is incompressible, the terms regarding pressure are unchanged and $p = p^*$ and

$$\sigma_e = \sigma_e^* - 3G\Delta\epsilon_e^p \tag{5.14}$$

Defining the plastic strain increment as a function of the gradient of the plastic potential, and specifying the failure criterion, one has

$$\dot{\boldsymbol{\epsilon}}^p = \lambda_3 \frac{\partial Q}{\partial \sigma_e} \tag{5.15}$$

$$F = \sigma_e - 2c = 0 \tag{5.16}$$

Substituting the plastic strain increment into Eqn. (5.14) and assuming an associated flow rule ($Q = F$)

$$\sigma_e = \sigma_e^* - 3G\lambda_3 \tag{5.17}$$

The consistency condition is then applied to solve for lambda

$$\lambda_3 = \frac{\sigma_e^* - 2c}{3G} \tag{5.18}$$

after applying the value of λ_3 to Eqn. (5.14), it can be shown

$$\sigma_e = 2c \tag{5.19}$$

As the effective stress cannot exceed the yield strength ($2c$), the stresses can be scaled in a method identical to that used for the radial return creep formulation.

$$\boldsymbol{\sigma} = p\mathbf{m} + \frac{2c}{\sigma_e^*}\mathbf{S}^* \tag{5.20}$$

This simple radial return plasticity formulation can be used to evaluate the failure of isotropic homogeneous materials, or entirely cohesive materials through a von mises failure criterion. This scheme is applied to ice in Chapter 7.

Chapter 6

Selection of Stopping Criterion

6.1 Motivation

With drifting pressure distributions diminishing confidence of the results from creep analysis, the question that needs to be asked is at what point does the pressure field begin to deteriorate? This prompted a closer look at a problem's entire history with regard to changes of the stress values. The goal was to pinpoint the iteration at which the pressure distribution begins to drift, ideally identifying a tell tale sign. To do this, long term analysis of problems was conducted, and the evolution of many variables was tracked. The variables that were tracked are measured changes in the residual load, the creep load, the equivalent deviatoric stress, and the value of pressure. It was assumed that taking a closer look could gain the insight needed to identify stopping criterion, which in turn could be used to control the quality of solution attained.

The "converged" solution has to correspond to steady-state. With pathological errors such as spurious pressure distributions and locking, determination of steady-state is difficult, as the problem can continue to degenerate indefinitely due to locking. Ways to look past this were required.

To conduct this analysis, the double slope was once again chosen. The 192 element, 117 node mesh was used, which was previously denoted as the fine mesh. Six noded verifications use a 48 element 117 node mesh. The radial return creep formulation was used to conduct this analysis using the method of successive approximation (MSA). The predictions that follow are by no means exact with respect to the location of steady state. It was assumed that as long as a reasonable prediction is made after initial stabilization, that only small changes occur, and therefore any point close to this region will display minor deviations from a 'steady-state' solution.

6.2 Stopping Criterion

6.2.1 Residual Load Norm

The residual load norm ($|R|$) allows quasi-static equilibrium to be tracked within the body being analysed. The norm itself is defined as follows

$$|R| = \sqrt{\frac{\mathbf{R}^T\mathbf{R}}{\mathbf{F}^T\mathbf{F}}} \tag{6.1}$$

in which $\mathbf{R} = \mathbf{F} - \int_V \mathbf{B}^T\boldsymbol{\sigma}dV$ is the residual load vector and $\mathbf{F}$ is the total load applied. Within the context of this analysis $|R|$ will not go to zero due to the smoothening algorithm, which redistributes pressure, thereby upsetting equilibrium slightly. On the other hand, if steady-state is attained, $|R|$ should approach a constant value.

6.2.2 Creep Load Norm

The creep norm ($|C|$) is then calculated as

$$|C| = \sqrt{\frac{\mathbf{C}^T\mathbf{C}}{\mathbf{F}^T\mathbf{F}}} \tag{6.2}$$

in which $\mathbf{C} = \int_V \mathbf{B}^T\mathbf{D}\Delta\boldsymbol{\epsilon}^c dV$. The thinking behind this measure is that it provides insight to the magnitude of creep load distribution during a given step, which will ideally become constant under steady-state creep conditions.

6.2.3 Equivalent Stress Norm

The third measure of error used is the change in equivalent stress during a time step ($|\sigma_e|$).

$$|\sigma_e| = \frac{\Sigma\left(\frac{\sigma_e^{m+1}}{\sigma_e^m} - 1\right)^2}{nelq} \tag{6.3}$$

where 'm' is the iteration number, and $nelq$ is the number of elements with $\sigma_e > 0$, which is synonymous to the number of elements which are creeping.

6.2.4 Pressure Field Change

While it is possible to propose a measure of error for the pressure change, relative to a norm, it was found that the absolute value, not squared, is more sensitive; *i.e*,

$$\bar{e}_p = \frac{|\Sigma K\Delta\epsilon_v|}{nel} \tag{6.4}$$

where K is the elastic bulk modulus, ϵ_v is the volumetric strain change from this iteration, and nel is the number of elements. The idea is that $\Delta\epsilon_v \to 0$ as steady-state is approached. Given the smoothening, the volumetric strain rate levels off, but does not vanishing completely.

6.3 Time Step

Time step was found to have interesting effects on the solution. Figure 6.1 shows how pressure degrades with the number of iterations. The scale ranges from -50 kPa (blue) to 450 kPa, or greater (red), with compression being positive. It is apparent that through iterations, the instance of checker boarding increases. The factor α is used to manipulate time step magnitude, such that $\Delta t = \alpha \Delta t_{cr}$. The critical time step is 1.73×10^{-3}.

In repeating this test with $\alpha = 0.001$, the pressure distribution degradation is the same over a similar number of iterations; however, the time of the solution is not. When using creep flow, it was assumed that the stresses are constant during the time step, and that the time step is sufficiently small for a quality solution. With a smaller time step the stresses change more often; this led, in some cases, to a faster relative convergence. In the case of this example with $\alpha = 0.01$ (original time step), the solution was found to be between 400-600 iterations, while with $\alpha = 0.001$ (time step was 10 times smaller), the solution converged at $\approx$10000 iterations. While the time step is a factor of 10 smaller, the solution occurs in roughly 20 times the number of iterations. Taking this into consideration, it was seen that proper choice of time step is required. The converse is also true, with a time step that is too large $\alpha = 0.1$, the solution was not readily approached, and the highest values of velocity were less than would be predicted (5.1 m·a instead of 6). As the effect of time step has been quantified, this study now moves to the evaluation of stopping criterion.

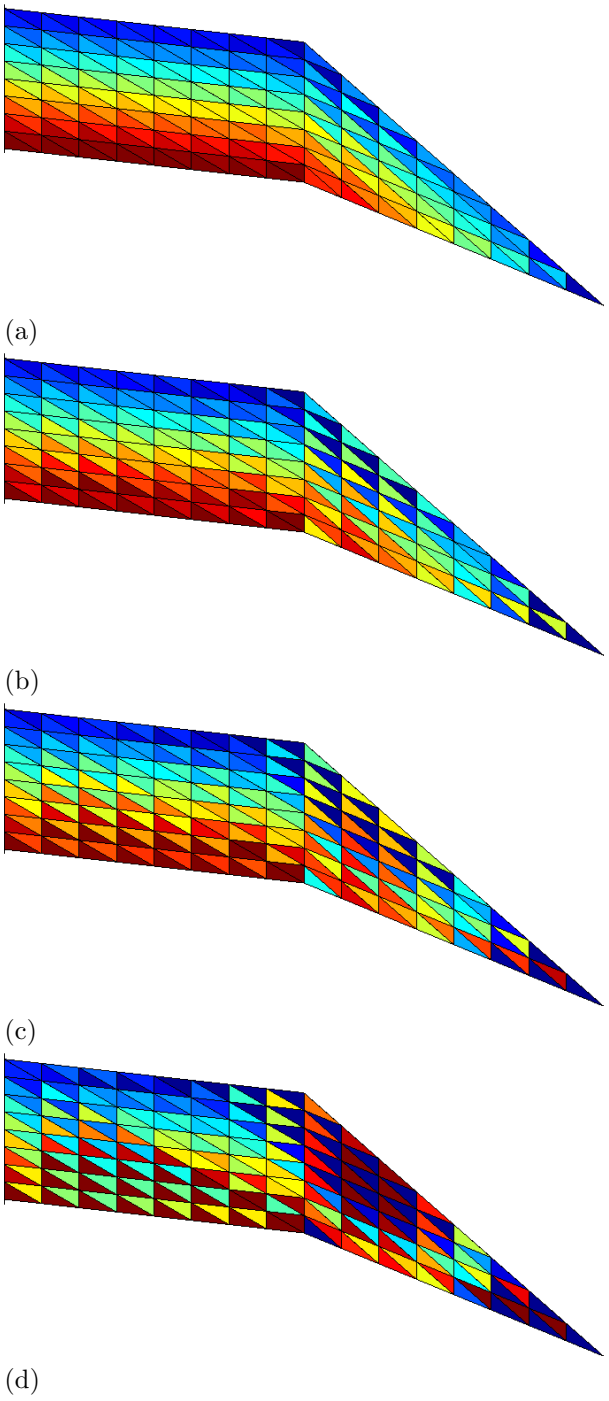

Figure 6.1: Pressure fields with iterations with $\alpha = 0.01$ and a linear creep law a) 1000 iterations b) 3000 iterations c) 6000 iterations d) 15000 iterations

6.4 Linear Creep Analysis

In order to evaluate stopping criterion assuming linear creep, three time steps were used. These correspond to one tenth ($\alpha = 0.1$), one hundredth ($\alpha = 0.01$), and one thousandth ($\alpha = 0.001$) of the critical time step. Values of normalized norms, such as $|R|/\alpha$, were monitored throughout analysis to identify trends which did not depend on time step size. The critical time step is 1.73×10^{-3} s. The bench mark velocity, obtained from 6-noded simulation, is 6 m·a^{-1}. The time step during an iteration is $\Delta t = \alpha \Delta t_{cr}$, *i.e.*, for $\alpha = 0.1$, each iteration is a time step of $\Delta t = 1.73 \times 10^{-4}$.

When looking at Fig. 6.2, one observes that after the first few iterations the reduction in $|R|$ becomes relatively linear for $\alpha = 0.1$. If this were to be used as an indicator of the converged velocity, the solution is near 40 iterations, which gives a velocity of 5.1 m·a^{-1} and a value of $|R|/\alpha$ of 2%. This velocity is low when compared with the expected value. This solution was obtained by eye through the use of secants to approximate the slope of the two portions of the curve. This method was used for all trends of this type.

Figure 6.3 shows that there were two choices that could be made with respect to a converged value, a slight plateau with respect to larger changes between 30 and 70 iterations, as well as a much larger overall minimum between 460-480 iterations. As it was already known that the peak occurs 30-50 iterations ($v = 5.1$ m·a^{-1}), this shows that the first plateau is likely more indicative of the solution. In this way the $|C|$ is also in agreement with $|R|$. This shows the importance of looking at multiple possible stopping criterion. The value of $|C|/\alpha$ at this point is 4.7%.

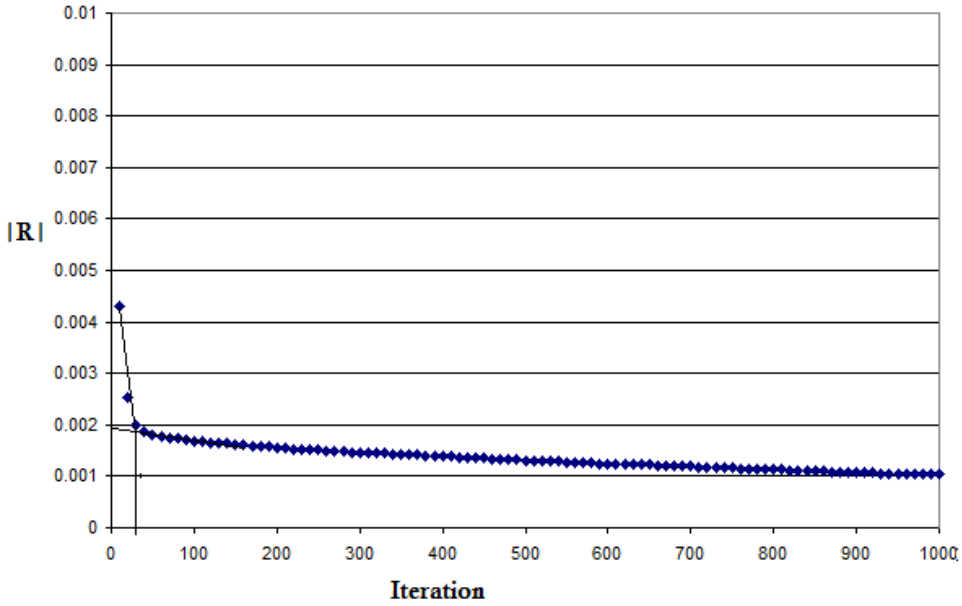

Figure 6.2: $|R|$ vs iteration for $\alpha = 0.1$, linear creep

Figure 6.4 shows that when viewing within very small ranges, $|\sigma_e|$ has a similar trend to $|C|$ for the linear creep problem. The difference lies in that the first plateau occurs around 80 and the second around 190 iterations, which are closer together than the ones encountered in $|C|$. These give velocities of 5.1 and 5.05, respectively. In this case it may not matter which is chosen. The value of $|\sigma_e|$ is very small, and does not appear to have a trend between problems, so a value has not been noted here.

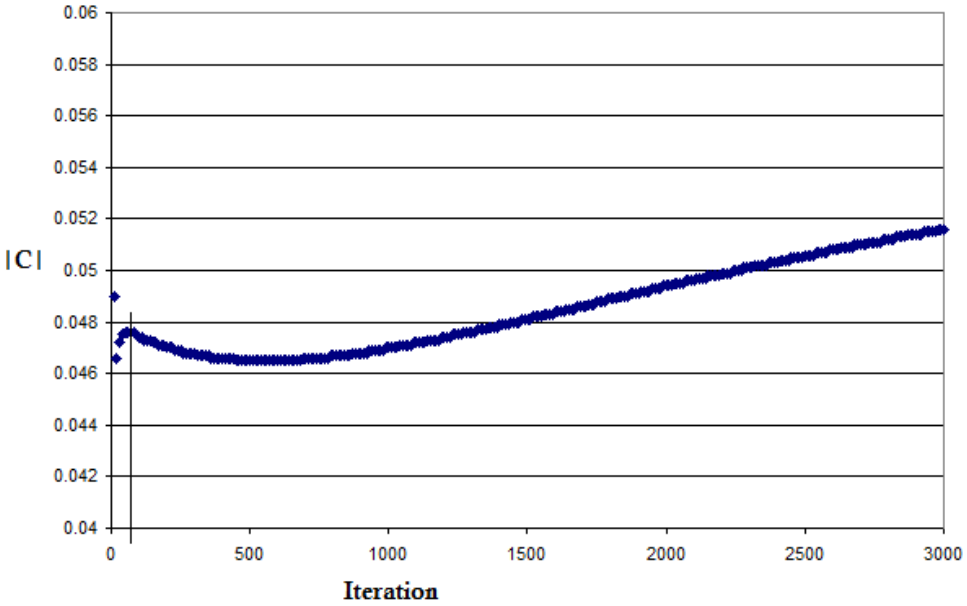

Figure 6.3: $|C|$ vs iteration for $\alpha = 0.1$, linear creep

Examining Fig. 6.5, it was observed that if an obvious or near linear trend is an indicator of convergence, a value of near 1000 iterations would be chosen, which is too large. Looking at the initial rapid changes in error, by 60 iterations they have effectively ceased. This corresponds to a solution of 5.1 m·a^{-1}. The value of $\bar{e}_p/\alpha$ at this point is 3.7%.

For the value of $\alpha = 0.01$, the trends were the same as when $\alpha = 0.1$. Large changes in $|R|$ stopped occurring between 300-500 iterations. The velocity values at this point were roughly 6 m·a^{-1}, which corresponds to the expected solution. The value of $|R|/\alpha$ at this point was 2.09%, which was very close to the value from the previous time step. For $|C|$, which had 2 relatively static areas, they corresponded to 500-600 iterations, as well as 4500 iterations. Once again the solution fell on the first plateau, at a value of 6 m·a^{-1}. The value of $|C|/\alpha$ at this point was 5.61%. $|\sigma_e|$ placed the possible solutions at 700 ($v = 5.99$ m·a^{-1}) and 1600 ($v = 5.94$ m·a^{-1}). Both were relatively good solutions. Ignoring the overall trend of $\bar{e}_p$ and watching closely for the rate of

change, 600 iterations was chosen as opposed to 10000 iterations. This gave a velocity of 6 m·a^{-1} and a $\bar{e}_p/\alpha$ of 4.96%.

Lastly, for the case of $\alpha = 0.001$, the $|R|$ is shown in Fig. 6.6. This figure does not have the clear trend that was seen in the larger time steps, and is much more gradual. This is attributed to a greater number of steps with smaller change between each step. In a case such as this, it is best to watch the trend of other measures, such as the equivalent stress. Time steps that are too small should be avoided as they are computationally time expensive and it is more difficult to evaluate steady-state conditions.

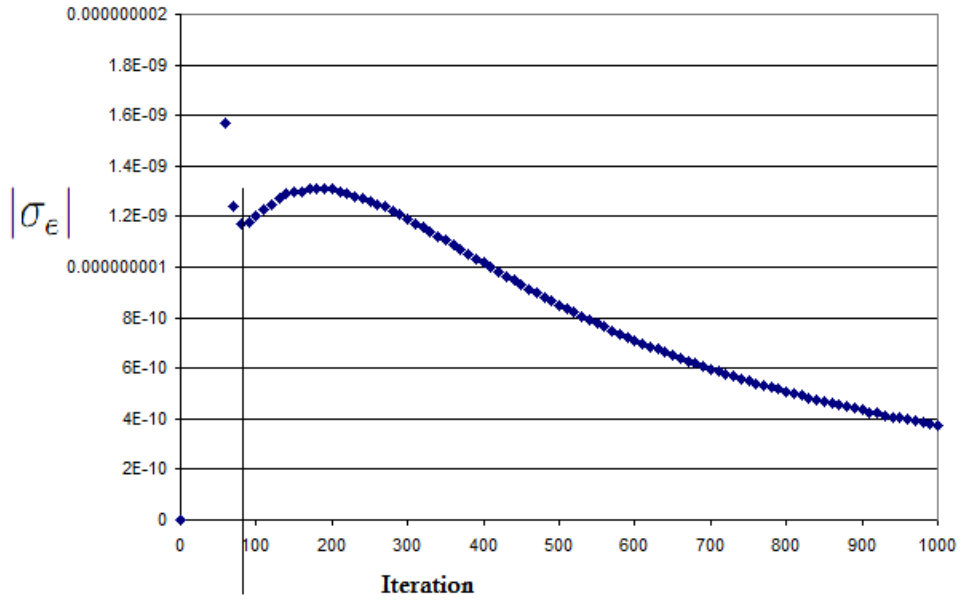

Figure 6.4: $|\sigma_e|$ vs iteration for $\alpha = 0.1$, linear creep

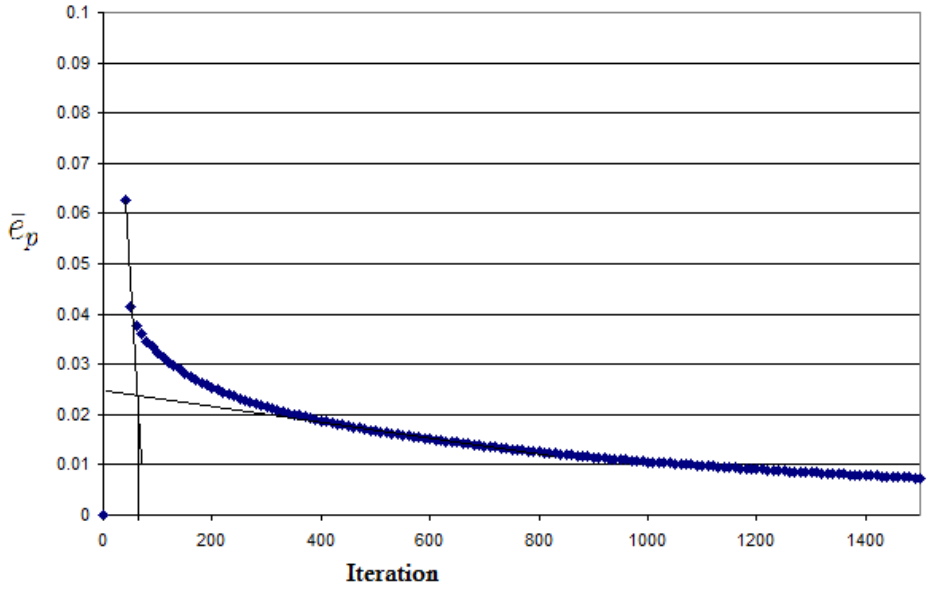

Figure 6.5: $\bar{e}_p$ vs iteration for $\alpha = 0.1$, linear creep

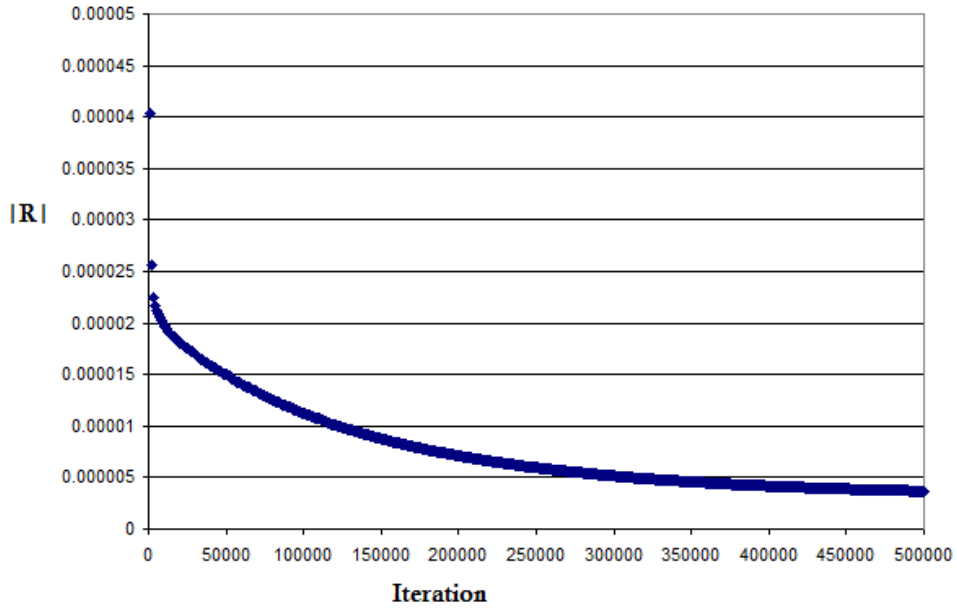

Figure 6.6: $|R|$ vs iteration for $\alpha = 0.001$, linear creep

$|C|$ had a trend similar to that shown in Fig. 6.3. There was a plateau at 8000, which gave a velocity of 6.1 and a $|C|/\alpha$ value of 5.69%. The value of $|C|$

was similar to that for $\alpha = 0.01$, providing insight with regards to convergence of the solution. For $|\sigma_e|$, the first plateau corresponded to 7000 iterations and a velocity of 6.1 m·a^{-1}; however, the second plateau at 15000 iterations was closer to the expected solution of 6.05 m·a^{-1}. For this very small time step, this appeared to provide a better estimate of the solution than the previous measures. Examining $\bar{e}_p$, a value of 5000 iterations would be appropriate. This corresponds to a velocity of 6.11 m·a^{-1} and a $\bar{e}_p/\alpha$ of 5.4%.

6.5 Discussion of Linear Creep Analysis

6.5.1 Linear $\alpha = 0.1$

Through the stopping criterion analysis, predictions of steady-state ranged from 40 iterations to 1000 iterations, with the majority being less than 100. Thus it was possible to identify a reasonable interval for convergence. These values can be compared with the horizontal velocity convergence to gain greater insight, and to see if the solution obtained from the norms is agreeable. The velocity profile is shown in Fig. 6.7.

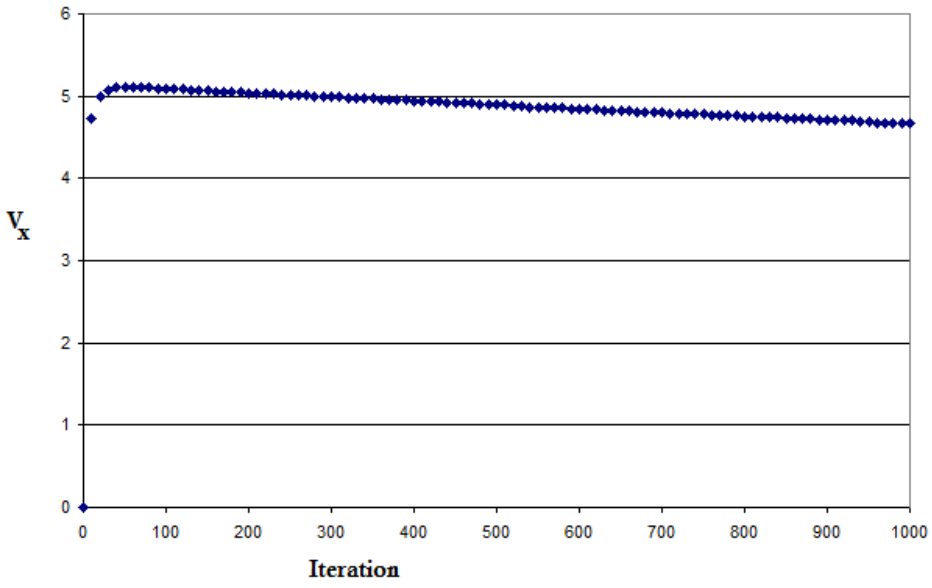

Figure 6.7: v_x vs iteration for $\alpha = 0.1$, linear creep

It was observed that no significant changes in velocity occur after 40 iterations, after which locking occurs. The pressure distributions were then compared for iteration 40 and 600 (Fig. 6.8), to check the quality of the pressure distribution. It is apparent that the pressure distribution at 600 iterations is very poor, as it contains large areas of checker boarding. It also contains more values at or in excess of the upper bound of 450 kPa (red). A good pressure distribution was obtained corresponding to 40 iterations, that was free of checker boarding. $|R|$, $|C|$ and $|\sigma_e|$ together give a good indication of steady-state. $|\sigma_e|$ provides an upper bound with respect to the number of iterations required to achieve steady-state. When considering the material relaxation, this solution falls between 50% and 90% relaxation, which correspond to 40 and 135 iterations (.25 and 0.84 days), respectively. It should be noted that for a relaxation test on a linear material percent relaxation $= e^{-\kappa t}$, where $\kappa = 3G \cdot A$.

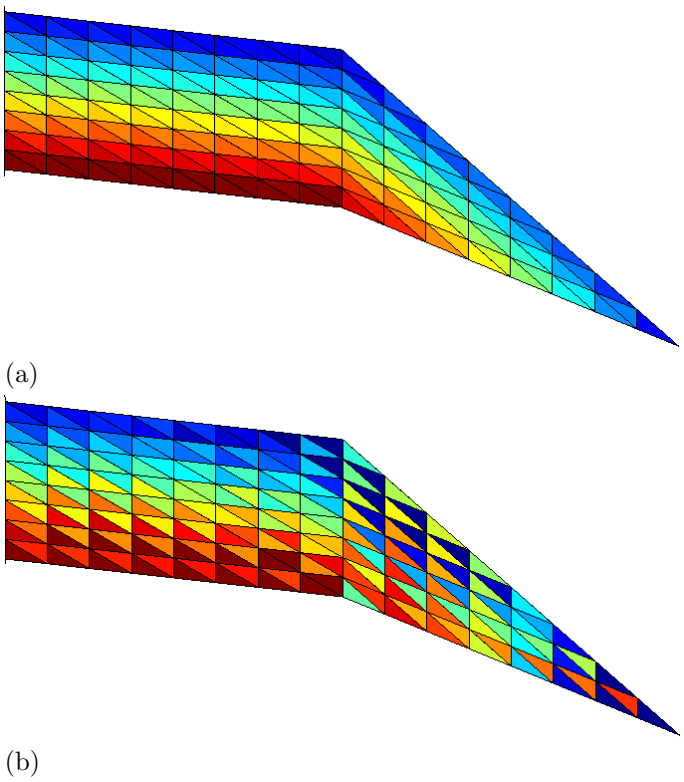

Figure 6.8: Pressure fields with iterations with $\alpha = 0.1$ and a linear creep law a) 40 iterations b) 600 iterations

Although $\alpha = 0.1$ was not a sufficiently small time step to produce the expected velocity, it provided insight to the convergence trends of norms. It is useful in familiarizing the reader with the norm analysis, as the trends are representative of other values of α. It also helps demonstrate the selection of an adequate time step.

6.5.2 Linear $\alpha = 0.01$

For this particular value of α, the range of predictions was found to be extreme, placing steady-state anywhere from 400 to 10000 iterations. The same trend with respect to velocity is present, a quick convergence followed by a slow decline (Fig. 6.9). When examining the pressure distributions (Fig. 6.10) for

400, 1600, and 10000 iterations, the first 2 pressure distributions are seen to be acceptable, while the 10000 iteration distribution is poor. Both the 400 and 1600 iteration pressure distributions would return reasonable results with the application of post simulation smoothening. Overall, the norms were found to be useful with regard to establishing at what point a steady-state is achieved. The equivalent stress norm ($|\sigma_e|$) again provided a slight upper bound with respect to the number of iterations to achieve steady-state.

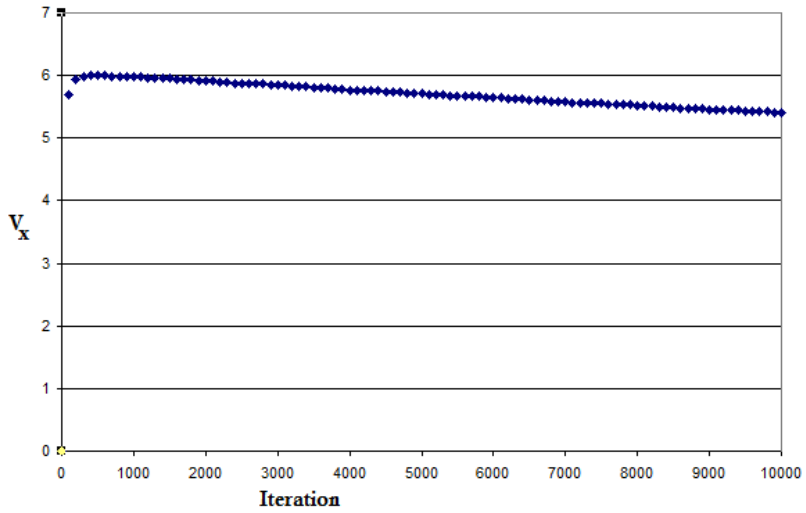

Figure 6.9: v_x vs iteration for $\alpha = 0.01$, linear creep

With respect to material relaxation, the 1600 iteration solution exceeds 90% relaxation (1350 iterations), but is less than 99% relaxation (2700 iterations). The 400 iteration solution occurs at 50% relaxation. The 10000 iteration solution greatly exceeds these values, which may explain the degeneration in the pressure distribution.

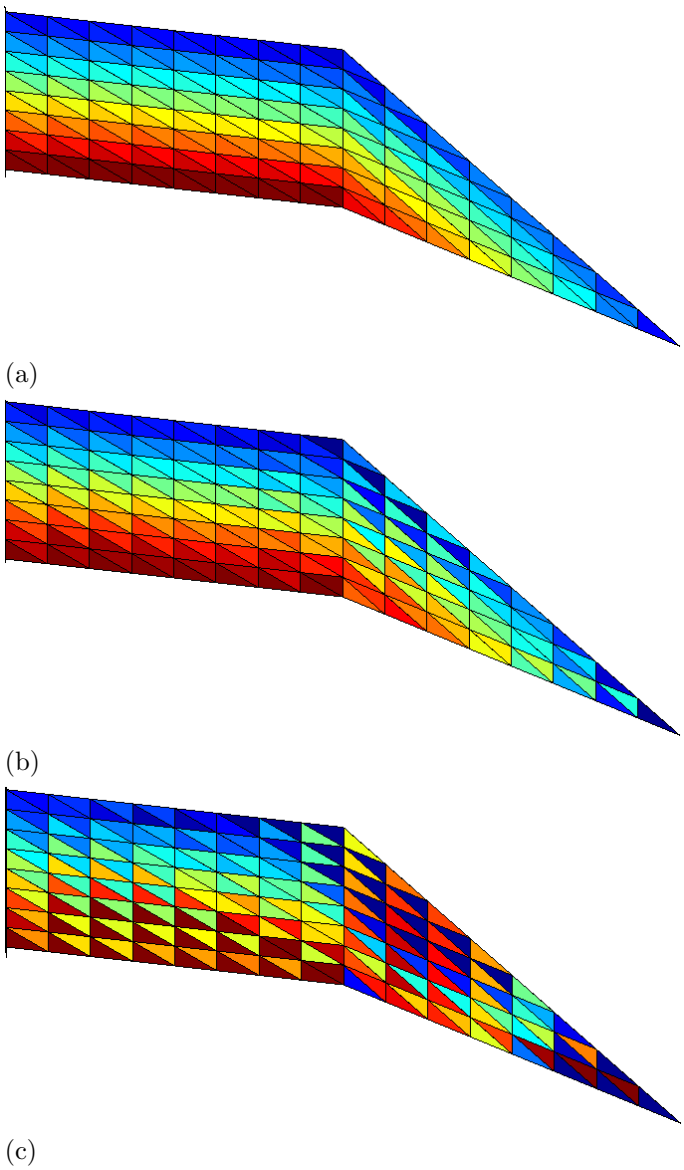

Figure 6.10: Pressure fields with iterations with $\alpha = 0.01$ and a linear creep law a) 400 iterations b) 1600 iterations c) 10000 iterations

6.5.3 Linear $\alpha = 0.001$

This time step, which is viewed as being too small when considering computational efficiency, predicts the velocity peaks at a higher value (6.11 $\mathrm{m{\cdot}a^{-1}}$), but maintains the same trend as Fig. 6.7. The norms provided a fairly disperse set of guesses from 7000 to 15000, which were near the peak in the velocity

field. As the norm histories did not provide well defined changes, it is best to look at the equivalent stress history. Using the equivalent stress as a predictor, steady-state is between 8000 and 10000 iterations, with velocities ranging from 6.08–6.1 m·a^{-1}. Regardless of the inconclusive predictions provided by the norms, good pressure distributions are obtained from both 9000 and 15000 iteration analyses as shown in Fig. 6.11. Most solutions from norms fell between 50% relaxation (4000 iterations) and 90% relaxation (13500 iterations).

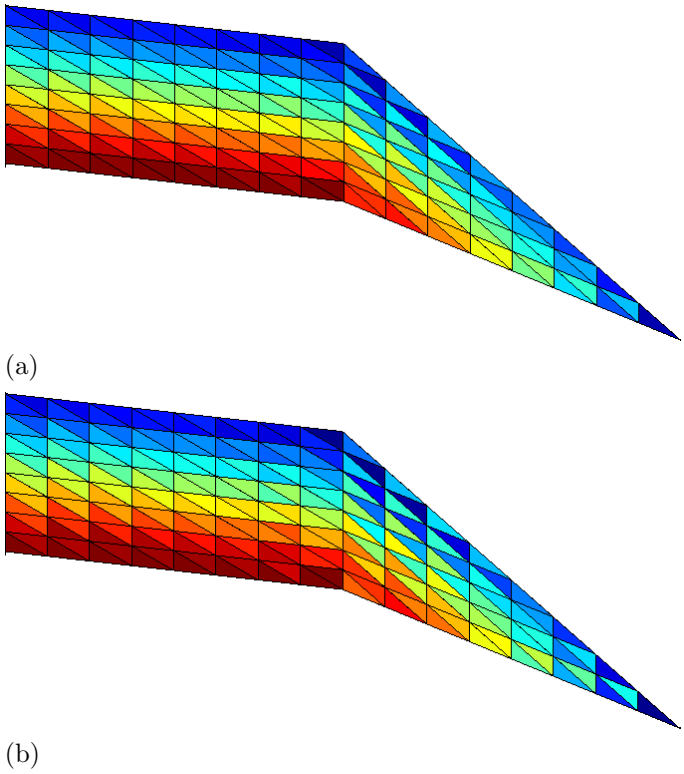

(a)

(b)

Figure 6.11: Pressure fields with iterations with $\alpha = 0.01$ and a linear creep law a) 9000 iterations b) 15000 iterations

6.6 Cubic Creep Analysis

Two numerical tests were conducted with a cubic creep law, using the same creep constant as was used for the linear law ($A = 0.001$ kPa^{-1}yr^{-1}). One

tenth and one hundredth of the critical time step were used in this analysis. The thousandth of the critical time step ($\alpha = 0.001$) simulation was not included as the examination of norms provided ambiguous predictions. The critical time step is 6.73×10^{-5}, yielding time steps of 6.73×10^{-6} and 6.73×10^{-7} for $\alpha = 0.1$ and $\alpha = 0.01$, respectively . Using a 6-noded MSA, a velocity of 6.26 $\text{m}\cdot\text{a}^{-1}$ was obtained, while a linear DR solution provided a velocity of 6 $\text{m}\cdot\text{a}^{-1}$. Acceptable solutions are assumed to be close to 6 $\text{m}\cdot\text{a}^{-1}$, as assuming greater precision is not plausible.

Figure 6.12, that plots $|R|$ versus iteration, a point at the end of the rapid changes was chosen, near 470 iterations, a velocity of 5.99 $\text{m}\cdot\text{a}^{-1}$ and $|R|$ of .0194% are obtained.

The creep norm, shown in Fig. 6.13, provides a clear trend of change with respect to iteration. Between 200-350 iterations, there is a sharp decline in the norm, after which changes appear linear. Looking at the velocities presented, they range from 6.19 $\text{m}\cdot\text{a}^{-1}$ at 200 to 6.01 $\text{m}\cdot\text{a}^{-1}$ at 350. The value of $|C|/\alpha$ is around 4.75%.

Figure 6.14, that presents $|\sigma_e|$ versus iteration, shows a trend change around 600 iterations, which corresponds to a velocity of 5.98 $\text{m}\cdot\text{a}^{-1}$. Figure 6.15, that presents $\bar{e}_p$ versus iteration, shows a fairly sharp reflex in the error curve at approximation 500 iterations, which corresponds with a velocity of 5.99 $\text{m}\cdot\text{a}^{-1}$ and a $\bar{e}_p/\alpha$ of 1.76%, which is closer to the bench mark. This trend is easily identified and is in agreement with $|R|$ and $|C|$. In the cubic case the square of the pressure error appears to be useful if trend is not apparent in $\bar{e}_p$.

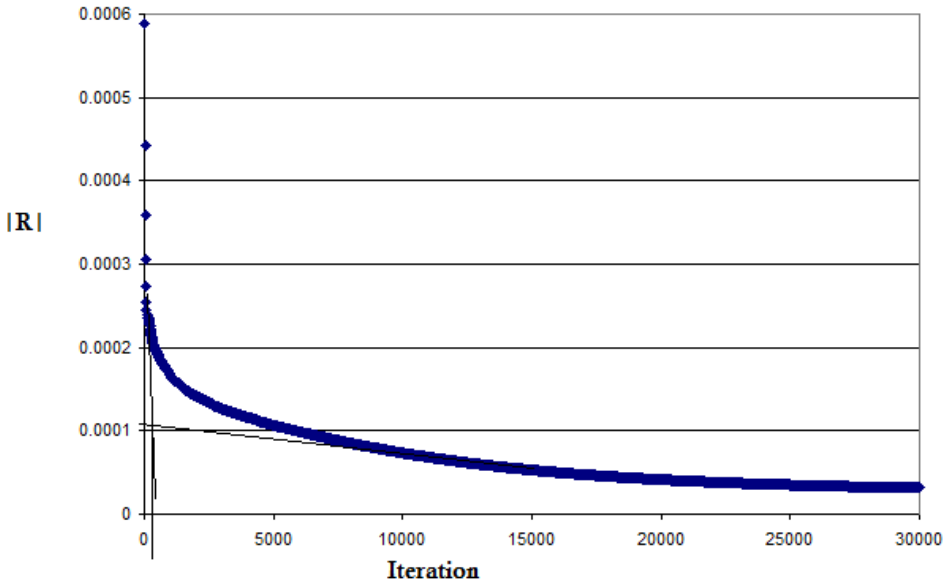

Figure 6.12: $|R|$ vs iteration for $\alpha = 0.1$, cubic creep

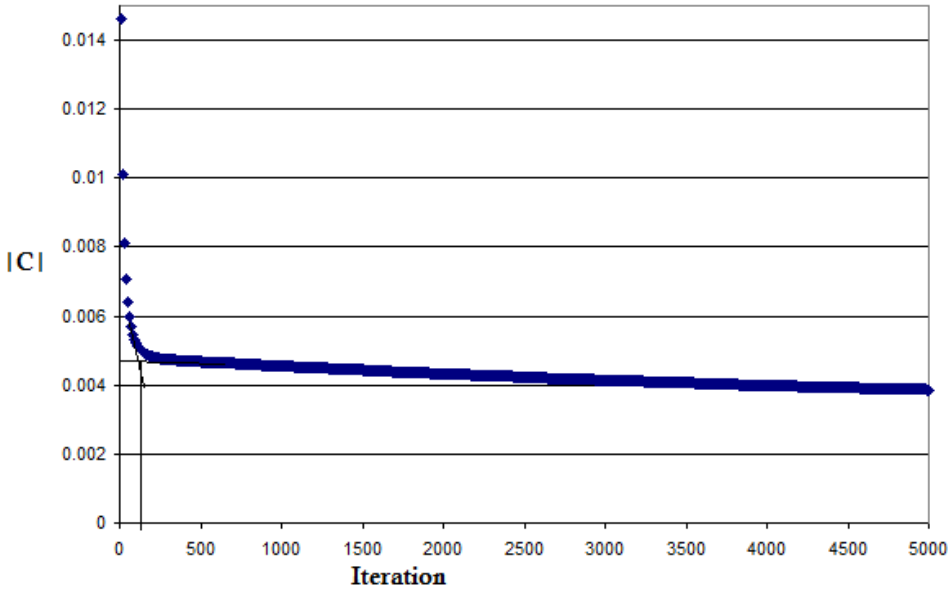

Figure 6.13: $|C|$ vs iteration for $\alpha = 0.1$, cubic creep

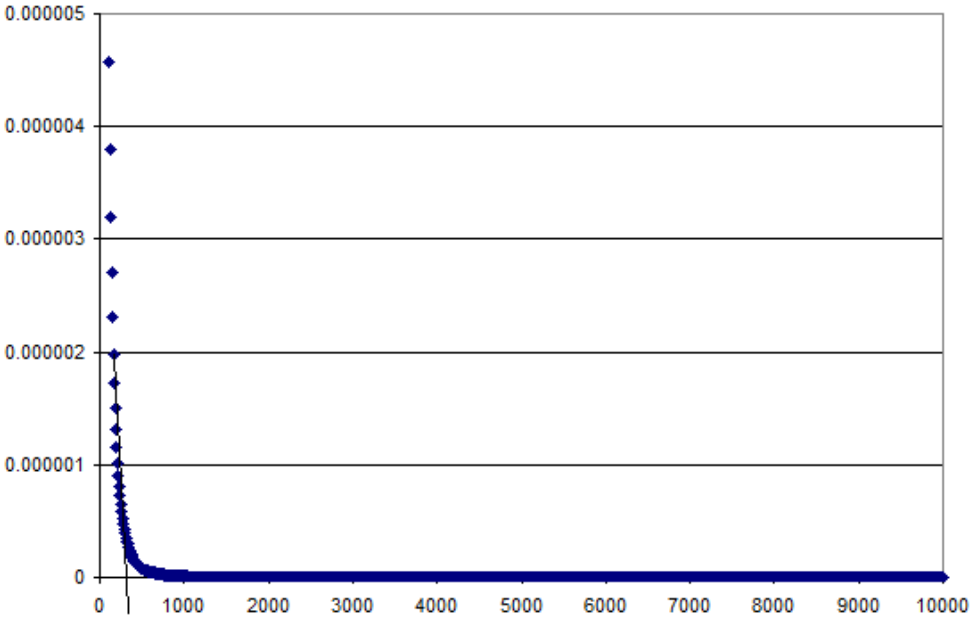

Figure 6.14: $|\sigma_e|$ vs iteration for $\alpha = 0.1$, cubic creep

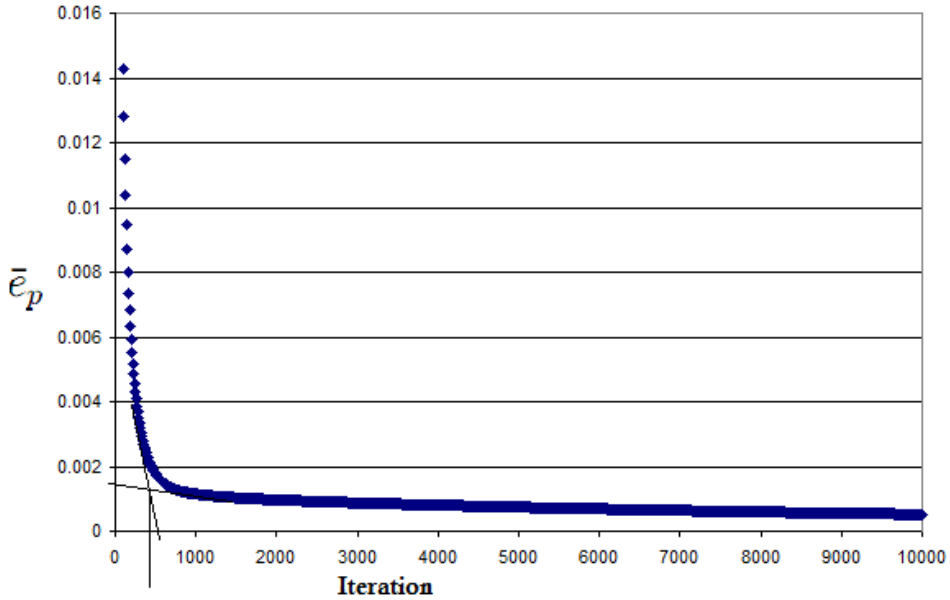

Figure 6.15: $\bar{e}_p$ vs iteration for $\alpha = 0.1$, cubic creep

If the methodology used in the previous example, with respect to $|R|$, were applied for $\alpha = 0.01$, iteration value of 1600 is obtained, which corresponds

to a velocity of 6.51 m·a^{-1} and $|R|/\alpha$ of .24%. While the trend was not as exaggerated for $\alpha = 0.01$, $|C|$ had a pronounced elbow. Unfortunately, this did not provide any new insight, as the elbow ended at roughly 1600 iterations, with a velocity of 6.51 m·a^{-1}. Having examined $|\sigma_e|$ for $\alpha = 0.01$, large changes ceased at 3000 iterations, giving a velocity of 6.2 m·a^{-1}. While the trend is not as exaggerated in Fig. 6.17, it was observed that no significant changes in $\bar{e}_p$ occurred after 2400 iterations. Using 2400 iterations as an approximation of the solution, a velocity of 6.26 m·a^{-1} and a value of $\bar{e}_p/\alpha$ of 0.38 % are obtained.

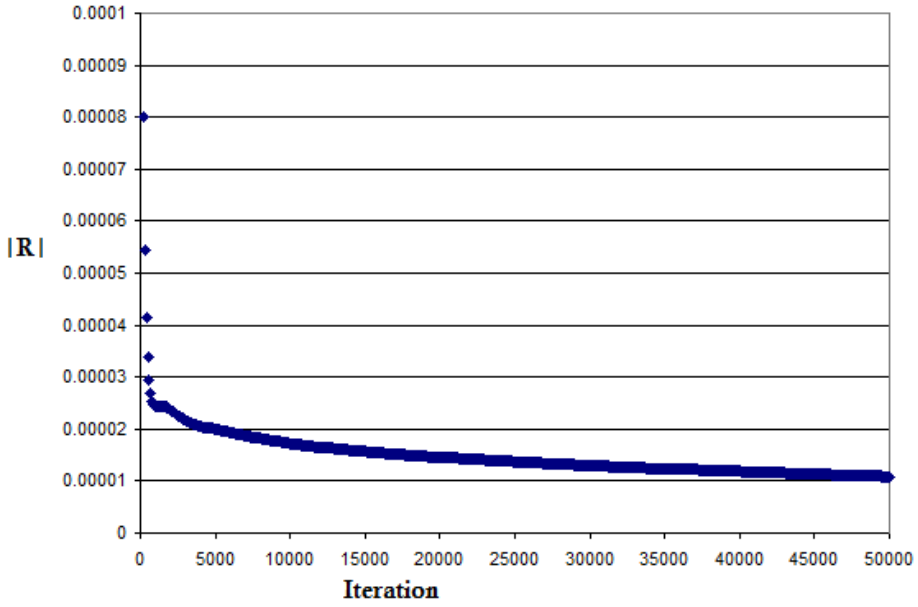

Figure 6.16: $|R|$ vs iteration for $\alpha = 0.01$, cubic creep

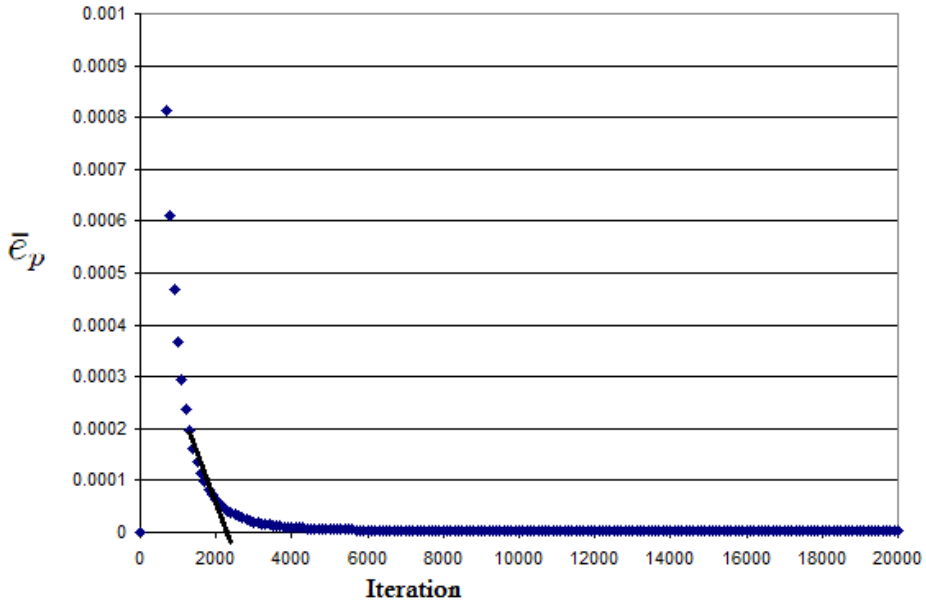

Figure 6.17: $\bar{e}_p$ vs iteration for $\alpha = 0.01$, cubic creep

6.7 Discussion of Cubic Creep Analysis

6.7.1 Cubic $\alpha = 0.1$

Steady-state using a cubic creep law, using the MSA, is more difficult to predict than when using a linear creep law. This is likely due to the fact that for $\sigma_e < 1$ changes in creep rate occur very slowly. For this particular time step, predictions ranges from 6–6.19m·a^{-1}. The velocity convergence plot begins at a large value and approach the minimum asymptotically, as shown in Fig. 6.18. It is possible that this time step may be too small, given the $\alpha = 0.01$ velocities were consistently higher, and closer to the 6-noded bench mark. The pressure field obtained from the 400 iteration analysis is very good (Fig. 6.19). Only the predictions from $|C|$ fall between 50% material relaxation (11 iterations, 0.027 days) and 90% relaxation (367 iterations, 0.9 days). Relaxation times

were calculated as $\left(\frac{\sigma_{e0}}{\sigma_e}\right)^2 = 6GA\sigma_{e0}^2 \cdot t$, assuming a representative $\sigma_e = 45$ kPa. It must be recognized that the actual relaxation times vary throughout the domain due to the stress dependency.

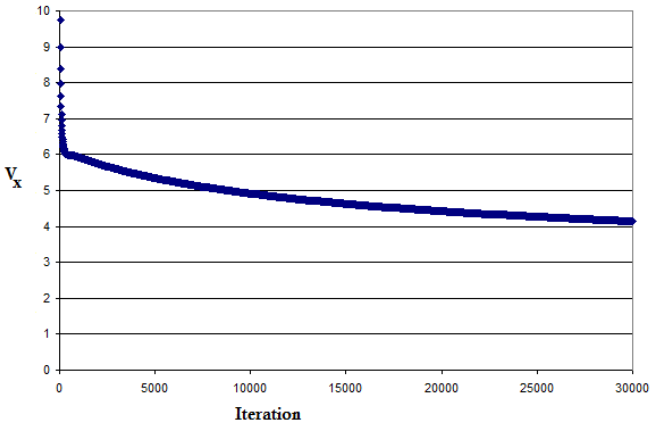

Figure 6.18: v_x vs iteration for $\alpha = 0.1$, cubic creep

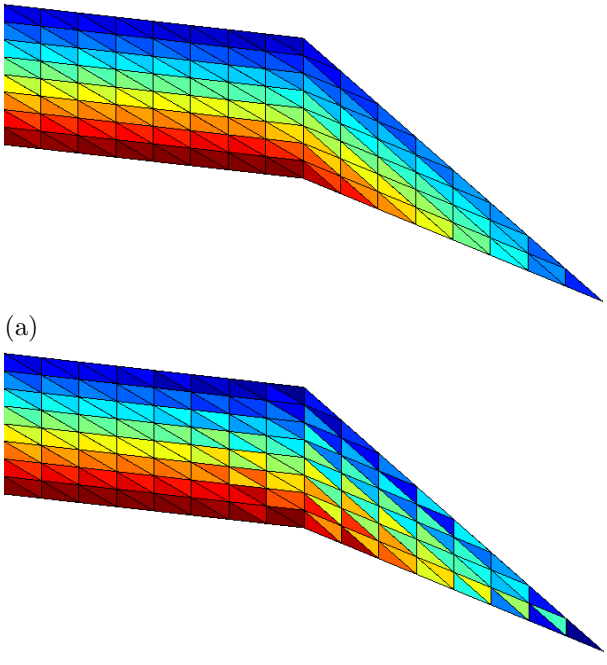

Figure 6.19: Pressure fields with iterations with $\alpha = 0.1$ and a cubic creep law a) 400 iterations b) 2000 iterations

6.7.2 Cubic $\alpha = 0.01$

This time step factor provided the results more consistent with the benchmark than $\alpha = 0.1$. Predictions ranges from 6.2–6.5 m·a^{-1}. The pressure fields for both 1600 and 3000 iterations are quite good (Fig. 6.20). Both the 1600 and 3000 iteration solutions fall between 50% and 90% material relaxation, it is possible this accounts for the quality of pressure field.

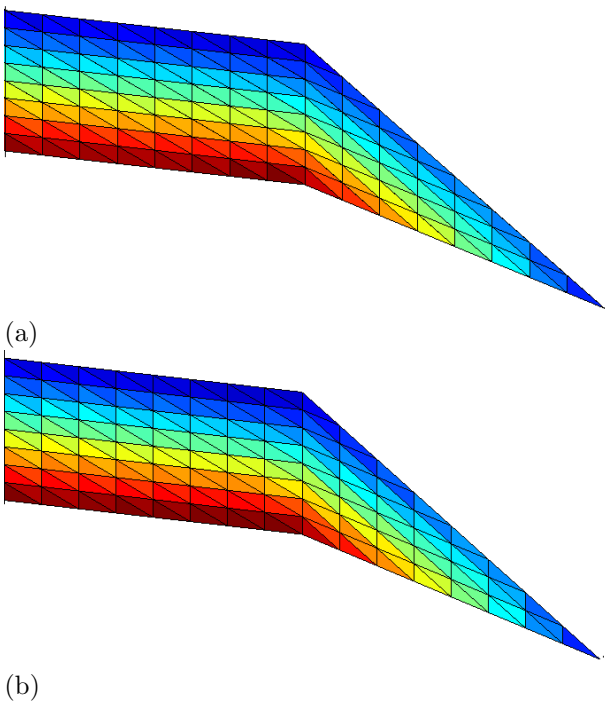

Figure 6.20: Pressure fields with iterations with $\alpha = 0.01$ and a cubic creep law a) 1600 iterations b) 3000 iterations

6.8 Final Comments

If the time step was too small, the identification of steady-state through that use of norms became difficult. If the time step was too large, an accurate estimate may be unobtainable. It is recommended that multiple time steps be used, in order to provide enough information to estimate steady-state.

Overall, for larger time steps, steady-state is identifiable, and the norms are in agreement. For the linear law $|R|$, $|C|$, and $|\sigma_e|$ were all able to estimate iterations that provided similar solutions. For the cubic law $|R|$,$|C|$, and $\bar{e}_p$ appeared to work better. In both cases, when faced with a time step that is too small, the quantity of agreeable information obtained from the norms is greatly reduced. Stopping criteria that were independent of time step ($|R|/\alpha$ and similar measures) did not show significant agreement to be used for the identification of steady-state.

Material relaxation coefficients were calculated to estimate time scales, to check if the analysis times were reasonable. All solutions fell between 50% and 90% relaxation. This is important, as the drift of pressure that is observed is attributed to non-uniqueness of pressure to volumetric strain, and the resulting accumulation of errors is due to numerical round-off or truncation error. The values for 50% and 90% relaxation may provide lower upper and upper bounds on times to achieve of steady-state.

The rate of change of a norm dictates where a reasonable steady-state the solution occurs. Consequently, caution must be taken when reducing the available data, as this could make rapid changes less apparent. The approach taken here may be compared to consolidation analysis, where one discards the immediate settlement (very large changes), and looks towards points of visible trend change. Two cases were commonly encountered, which are shown in Figs. 6.21, and 6.22. The solution methods that were successful are demonstrated on the figures for both cases. In case 1 the point of maximum curvature was sought, in case 2 the reversal of direction.

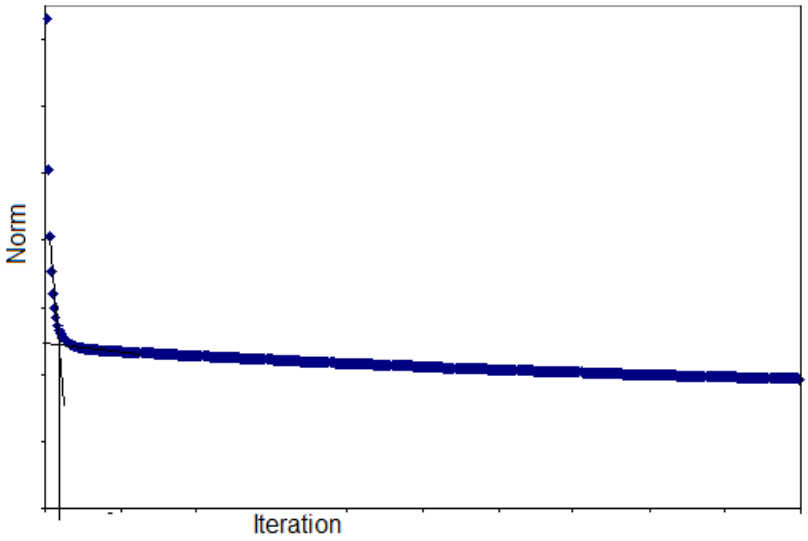

Figure 6.21: Steady-state prediction for case 1

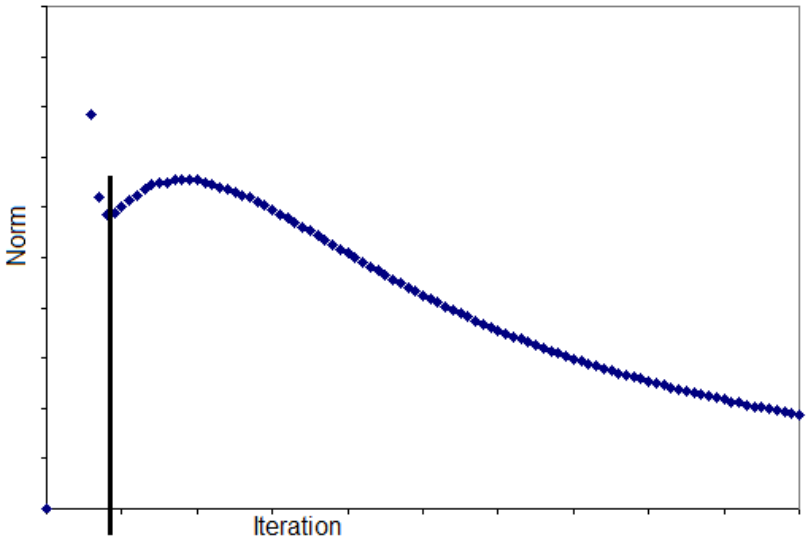

Figure 6.22: Steady-State prediction for case 2

For cases where there is no agreement between the norms, the value of equivalent stress vs. iteration was assumed to provide an indicator of steady-state. In the context of a linear creep law, equivalent stress provided similar convergence trend to that of the creep norm ($|C|$). For a cubic creep law, equivalent stress appears to provide a minima/maxima when steady-state has

been reached. This may not be true for other values of n.

The unfortunate aspect of this analysis is that it was not possible to identify a point or trend that identifies clearly when that the pressure field begins to drift. As norms did not identify when the pressure field diverged, this suggests that drift occurs incrementally throughout the analysis, due to round-off errors. Therefore, in order to minimize the negative effect of drift, excess computation must be avoided. Both the use of norms and the equivalent stress as a function of iteration provided useful tools for truncating the computation time required.

Chapter 7

Barnes Ice Cap

In order for the analyses presented within this work to be placed in the context of a real world problem, ice creep was examined, with respect to the Barnes ice cap. The Barnes ice cap is located on Baffin Island (69° 45′ N; 72° 15′ W). A contour map, from Hooke [14], shown in Fig. 7.1, is included. For the purpose of this analysis, the north east slope of the glacier (red box in Fig. 7.1), from the outer edge until the divide, is analysed. At the divide, compression is expected to dominate the behaviour, while further down the slope shear flow should dominate, causing a higher horizontal velocity. Both the radial return creep formulation and the traditional formulation are used to examine the creep of the ice cap.

Predictions from various creep laws were examined to evaluate their suitability, with respect to capturing the physics of this problem. These include Glen's power law, with $A = 0.017$ and $n = 4.2$, Nye's creep flow relation $\epsilon_e^c = \frac{1}{\sqrt{3}} A \left(\frac{\sqrt{3}}{3}\sigma_e\right)^n$, with $A = 0.17$ and $n = 3.07$, and Meier's flow law described as $\epsilon_e^c = \frac{1}{3} A\sigma_e + \frac{1}{\sqrt{2}} B \left(\frac{\sqrt{2}}{3}\sigma_e\right)^n$, with $A = 0.018$, $B = 0.13$, and $n = 4.5$ [13]. Predictions from the analysis were tested against the surface velocities that were measured during studies of the ice cap's movement, in the mid 20th

century. It is important to note that creep laws are temperature dependent; therefore, the objective is to see which one is most suitable. Glen's work was conducted at $-0.2°C$, Nye's at $-0.8°C$, and Meier's at $0°C$. In a prior study by Hanafy, creep simulations were carried out for '3000 minutes', likely to attempt to reduce computational cost. This practiced constraint would have minimized pressure drift; however, if this was the case, it was not mentioned. A simulation with the FSM was also completed assuming a constant viscosity to judge the effectiveness of the approach on predicting the flow field for an irregular geometry. The A parameter is based on Nye's law assuming that a representative σ_e is 0.8 bars.

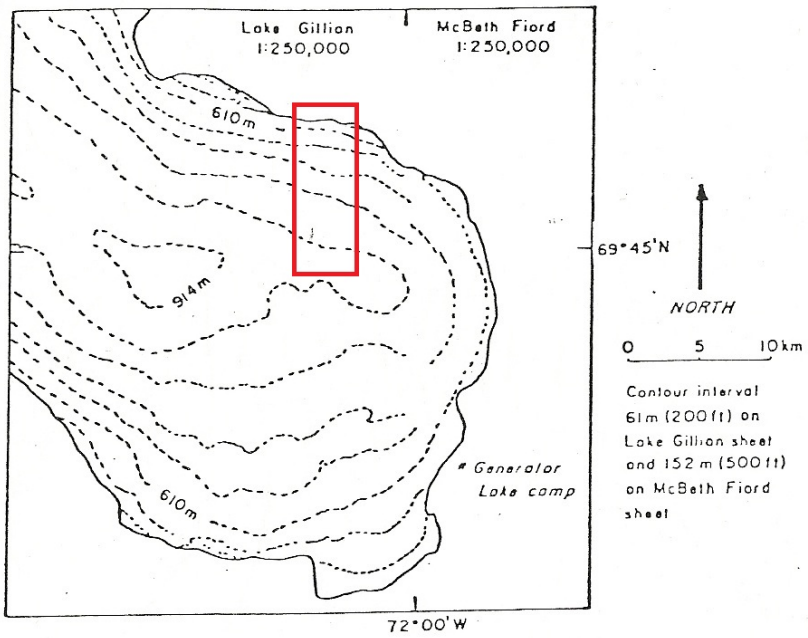

Figure 7.1: Contour map of Barnes ice cap [14]

The grid, which was used for this analysis is a 68 element, 48 node mesh, as shown in Fig. 7.2. While this mesh is rather coarse, it was assumed to be sufficient to accurately demonstrate the flow of the glacier. The base of the

glacier is fully fixed, which assumes that the ice is frozen to the bedrock and will not slip. The right hand side, which is taken at the divide, is a vertical plane, in which a zero shear condition is assumed together with the horizontal velocity being fixed at zero. The elastic modulus, Poisson's ratio and unit weight are $E = 907500$ kPa, $\nu = 0.34$ and $\gamma = 8.952$ kN·m^{-3}, respectively.

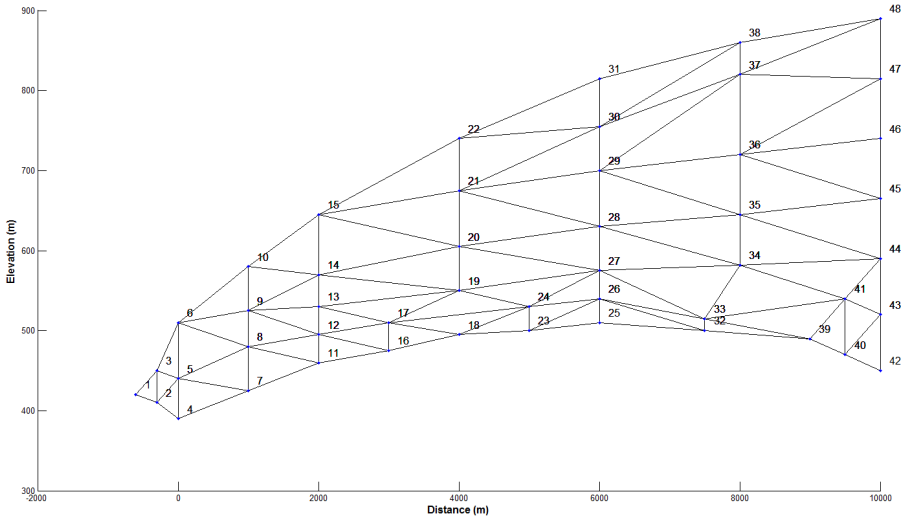

Figure 7.2: Mesh used for Barnes ice cap analysis

7.1 Horizontal Velocity Profiles

The methods discussed in the previous chapter were used to provide stopping criterion when using the method of successive approximation. Nye's and Glen's creep laws were implemented with both the radial return and tradition creep formulations. Meier's creep flow was only evaluated with the radial return creep formulation. The predictions for horizontal surface velocity are shown in Fig. 7.3, where the label 'B' following the law used (Glen, Nye, etc.) denotes the radial return creep formulation, and label 'A' the traditional creep formulation. Dynamic relaxation analysis was performed using Nye's law only.

When looking at the horizontal surface velocities, shown in Fig. 7.3, the

results from the Meier flow provide an obvious outlier. Surface velocities were much higher than predicted by the others, and will be disregarded in the following discussion. From the laws tested, Nye's provides results closest to the measured values when using the MSA, and up to 3000 metres provided a good trend with respect to the measured movement of the glacier. All MSA creep laws predicted a maximum velocity that was much closer to the divide than measured in-situ.

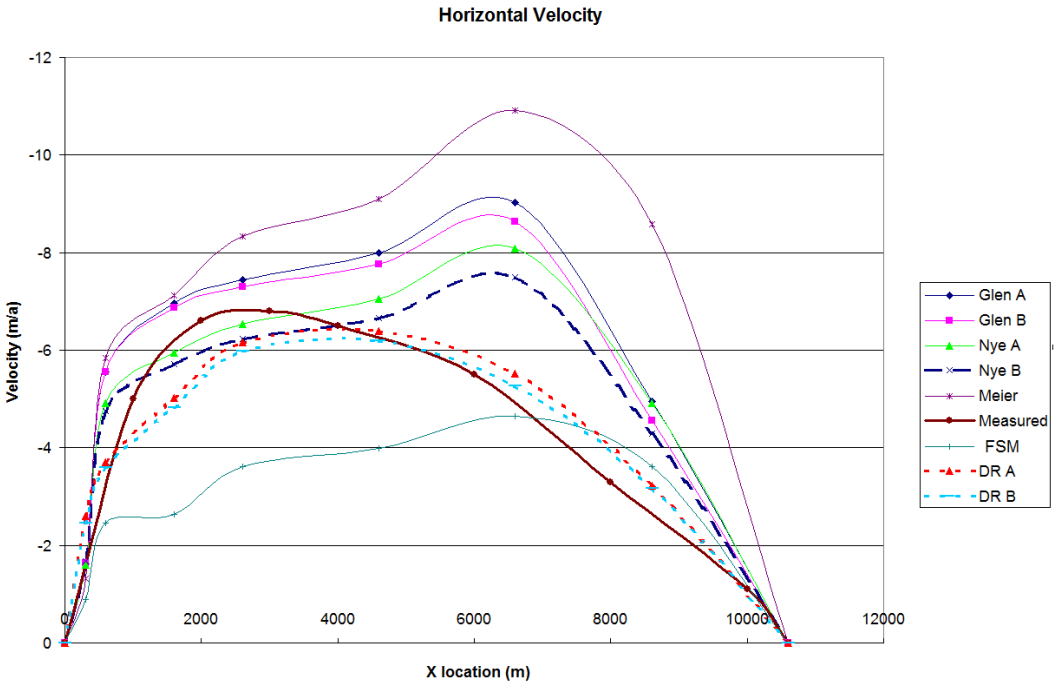

Figure 7.3: Results for horizontal velocities

Dynamic relaxation predicted a horizontal surface velocity profile closer to the measured results in trend and value, but the peak values were lower than that of the MSA. The DR algorithm provided the best results of all creep laws and algorithms tested.

The FSM prediction provided a poor overall prediction for the horizontal velocity, as it did not show the measured trend at any points. It should be

noted if a better prediction for viscosity had been selected, predictions might have been closer to the measured values. The velocity profile of the FSM also displayed odd trends that may be caused by complications when using the FSM for non-uniform meshes, as suggested by Huang and coworkers [15].

Given the difference in the trends between the predictions and measurements, it is clear that a single creep law (or constant coefficients) cannot be used to describe the flow behaviour of the glacier.

The similarity of trends with the various power laws within an algorithm are interesting. Figure 7.4 shows each horizontal surface velocity, normalized with respect to its maximum velocity. Glen's and Nye's law showed roughly the same trend, when used with the MSA, Meier's law predicted a similar trend. This suggests that a constant creep law (*i.e.* power law) can explain a trend, although the trend may not be correct. Solution scheme also seems to influence trend heavily. The trend presented by the FSM is relatively erratic compared to that predicted by the creep laws.

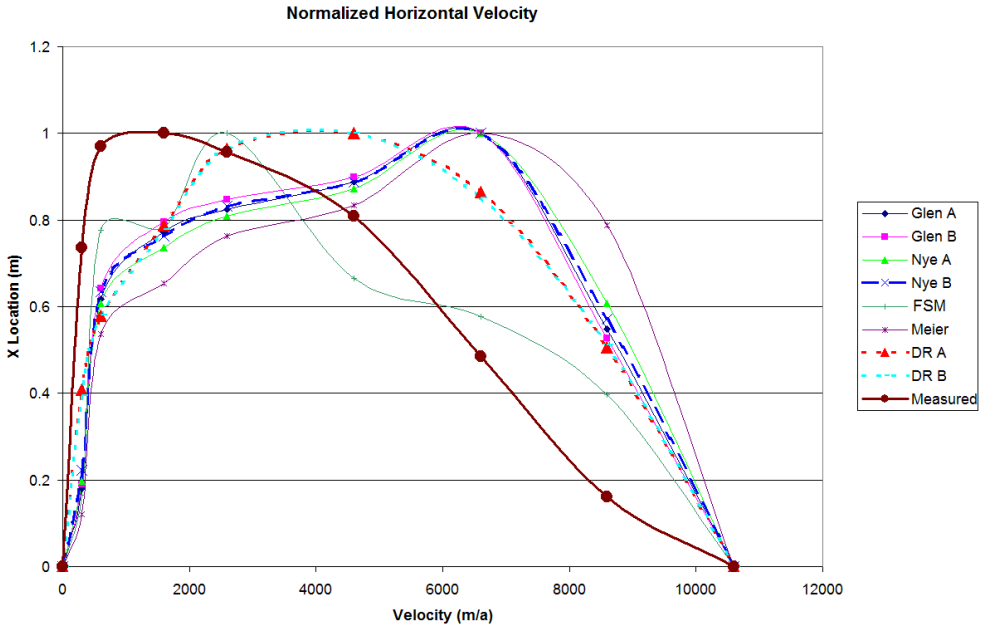

Figure 7.4: Results for normalized horizontal velocities

7.2 Vertical Velocity Profiles

MSA results for the vertical velocity profile (Fig. 7.5) are well in excess of the measured values. The higher horizontal velocity predictions near the divide explain why the vertical velocities are also much higher near the divide, taking into account the incompressibility constraint. The FSM and DR schemes both return much lower velocities, with the DR being closest to the measured values. The FSM and DR consequently have a lower horizontal velocity when approaching the divide.

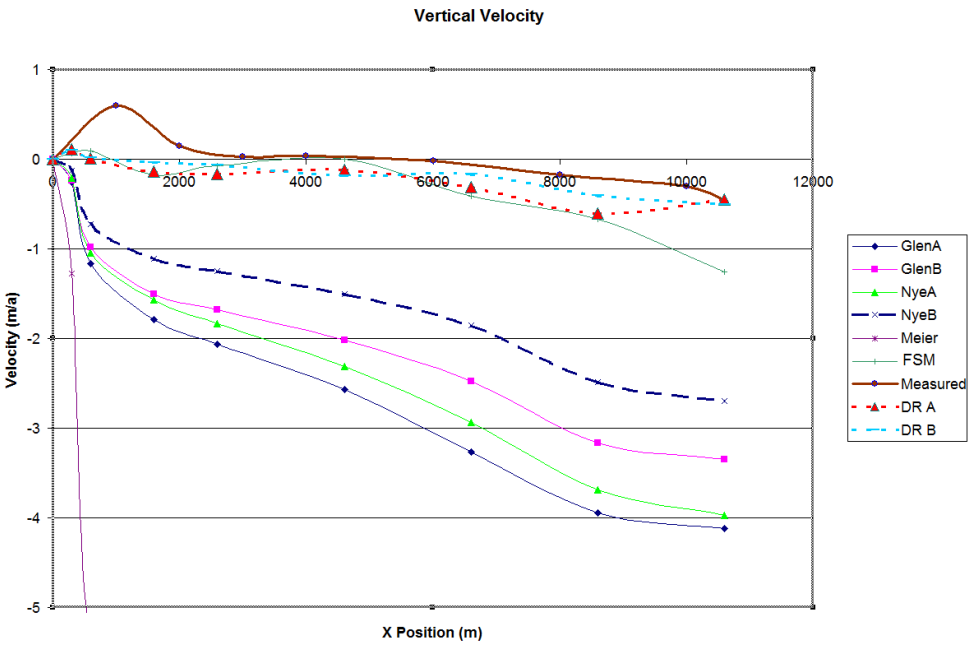

Figure 7.5: Results for vertical velocities

7.3 Pressure Plots

By using the methods presented in the stopping criterion chapter of this thesis, reasonable pressure fields were obtained for the creep formulations. The

solutions presented are all free of checker boarding. There are very few differences between the smoothened results obtained from Nye's flow law and the FSM (Figs. 7.6, 7.7, and 7.8). The plots are shown with 3500 kPa as red and -500 kPa as blue (compression is positive). The variations in pressure given are reasonable, *i.e.*, increasing with depth. At the base of the divide there are slight discrepancies with the Nye's flow law formulation. The FSM and DR do not show these discrepancies.

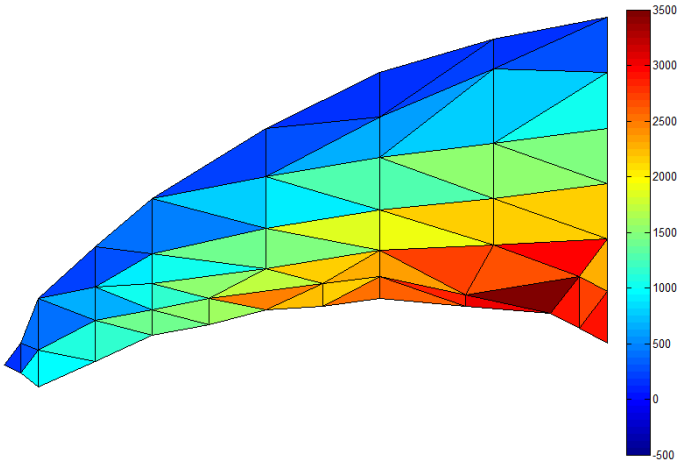

Figure 7.6: Pressure plot using Nye's law, smoothened

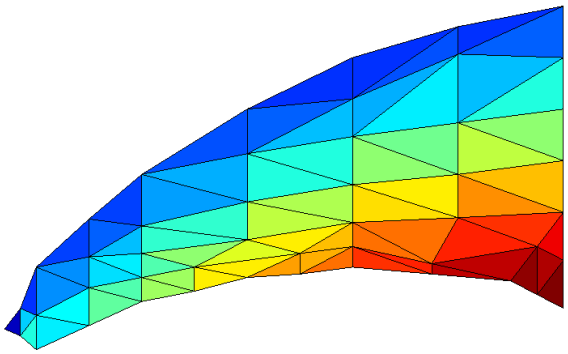

Figure 7.7: Pressure plot using FSM

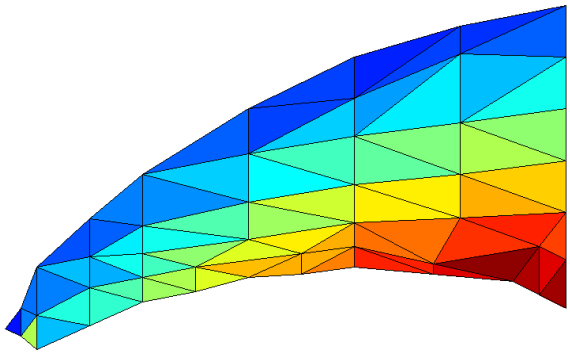

Figure 7.8: Pressure plot using DR with the radial return method and smoothening

7.4 Plasticity Analysis

The radial return plasticity presented in Chapter 5 was used to identify points of material yielding within the glacier. The strength variable, c, was set equal to the shear strength of random, polycrystalline ice (979 kPa at $-5°C$), taken from Sec. (2.4). The problem was solved iteratively to allow redistribution of stresses, while ignoring the possibility of tension cracking. A Poisson's ratio of $\nu = 0.34$ was used for the duration of the analysis, which corresponds to a value for instantaneous loading. Forty-two of the 68 elements were identified as having yielded. These are located about 100 m below the surface, where the deviatoric stresses S_{yy}, and S_{xx} are very large. The red elements (value exceeding 1) have exceeded the shear strength of the ice (fig. 7.9), which may indicate the possibility of basal yielding.

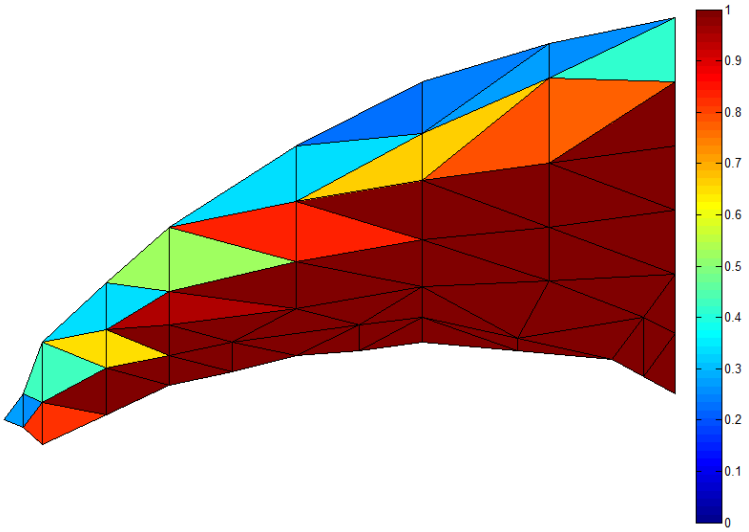

Figure 7.9: Results for areas of failure at 979 kPa shear strength

As the assumed shear strength may not be representative of the problem, simulations were carried out with two addition values; *i.e.*, 500 kPa and 1500 kPa. The results are shown in Figs. 7.10, and 7.11, respectively. For the 500 kPa simulation, most of the domain has yielded. This scenario does not seem likely. For the 1500 kPa solution, only the area near the base has yielded. As elements which have yielded are directly beside elements that are well below the yield strength, an increase in mesh density is expected to improve results.

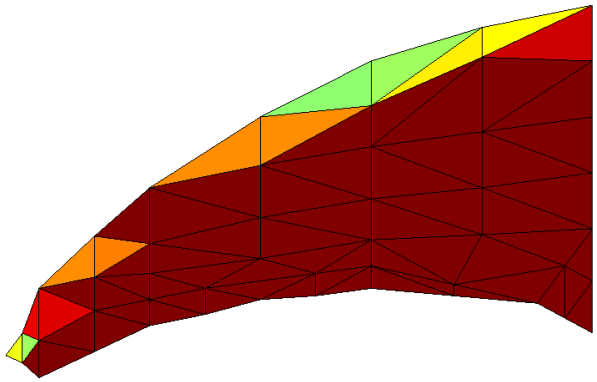

Figure 7.10: Results for areas of failure 500 kPa shear strength

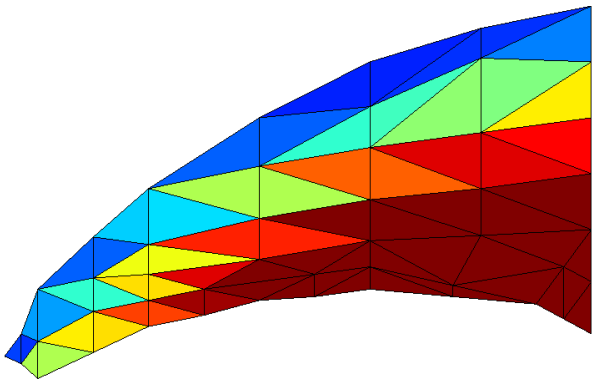

Figure 7.11: Results for areas of failure 1500 kPa shear strength

Figure 7.12 shows a post process smoothened yield ratio plot. The introduction of post process smoothening makes very little difference, causing the area of yielding to appear at a slightly greater depth.

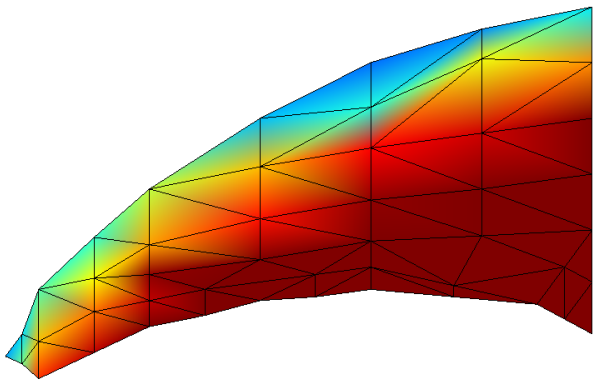

Figure 7.12: Results for areas of failure 979 kPa shear strength, with post process smoothening

The stresses presented for the yield of ice within a compressible domain are very high, peaking at over 15 bars. For quasi-static situations, it is suggested that the effective Poisson's ratio is $\nu = 0.5$ (Gold; [11]). This implies that the definition of failure is rate sensitive. The yield stress was assumed to be 1 bar, as suggested by Paterson [26], and $\nu = 0.4995$, for algorithm stability. Figure 7.13 shows yielding only in areas at the base near the toe, where large

deformations are expected, in contrast to the previous examples. Given that the stresses are more in line with what is observed for creep analysis, it is suggested that the apparent value for Poisson's ratio is more appropriate when considering long term yielding.

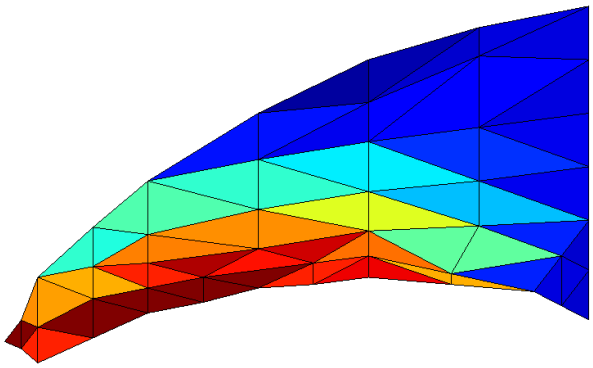

Figure 7.13: Results for areas of failure 100 kPa shear strength

7.5 Comments on the Results

The purpose of this analysis was to investigate the applicability of various creep laws to the Barnes Ice Cap. It was shown that a single creep law, or constant coefficients, were not adequate to simulate the measured behaviour. This is not surprising, as the A parameter varies with temperature and the density of ice. Where compression dominates, such as near the divide, the predicted vertical velocities exceed the measured velocities, which causes higher vertical velocity predictions. Nye's flow law provided the most suitable results in all formulations. Dynamic relaxation, using Nye's flow law, presented the most accurate values for horizontal and vertical velocity, with respect to the measured results, and showed a greater likeness to the trend of the measured values. The plasticity analysis included serves to demonstrate the versatility of the radial return procedure, and was able to identify potential material

yielding within the ice field.

Refinement with respect to property variation could improve this solution; however, such optimization of flow parameters was beyond the scope of this study. Previously, material variation was taken into account by Killeavy through manipulation of the 'A' parameter [18].

Both the traditional and radial return creep formulations obtained similar results. Pressure fields obtained from both creep formulations were in agreement, illustrating that the stopping criterion analysis (Chapter 6) is applicable to the traditional creep formulation. The velocity results from the radial return formulation were slightly lower, for both MSA and DR schemes. In terms of performance, no noticeable difference was observed. For a given creep law, time steps were equal. Nye's law had the largest time steps, $\Delta t = 0.111 \times 10^{-4}$ s, and Meier's had the smallest time steps $\Delta t = 0.866 \times 10^{-6}$ s. As there is a correlation between creep law and step size, larger exponent power laws will require a smaller time step. The radial return method, given the flexibility of time step, and use of dynamic relaxation are recommended for creep analysis.

Chapter 8

Concluding Remarks and Recommendations

8.1 Concluding Remarks

The majority of this work involved the capability of creep flow formulations to predict reasonable pressures and velocities when using low order elements. It is important to remember that creep flow was used in order to study the capability of the models to accomodate the extreme case of a fully incompressible domain. By examining incompressible domain problems, difficulties with the incompressible formulation were easily recognized. The study began with the transient creep analysis using method of successive approximations, which used a maximum time stopping criterion for preliminary analysis. With the addition of volumetric strain smoothening [7] pressure distributions were improved, but the results were still poor. Iterative solvers were also used. Dynamic relaxation [34] was found to provide adequate pressure fields.

A radial return method for creep flow was devised, that draws parallels to the methods used in plasticity. This method was shown to function well

under fully incompressible conditions, and was not limited by time step, which allowed the time step to be chosen based on the resolution required for an accurate solution. In contrast the traditional creep formulation had several drawbacks; *i.e.*, when analysing a fully incompressible problem, it functioned poorly, computation time increased,and very small time steps were required. The radial return method helped solve some of these problems.

The identification of steady-state through norms, and the change of effective stress was shown to be valuable tools, allowing the identification of acceptable solutions for both velocity and pressure. Spurious pressure distributions were prominent in the preliminary analysis. These pressure distributions alongside volumetric locking obscured when steady-state (secondary creep) was reached. In order to limit pressure drift, and identify steady-state, criteria for identifying when steady-state is attained for transient creep analysis were studied using the radial return creep formulation. Since the instance of large pressure changes was not found, and given the small values of $\bar{e}_p$, it is speculated that pressure drift occurs incrementally over the course of the entire analysis. This requires that the number of iterations be minimized, in order to obtain an acceptable pressure distribution.

The norm analysis used in the stopping criterion chapter was then applied to a more realistic problem, the Barnes ice cap. The traditional and radial return creep formulations, together with several creep laws were used to simulate the flow field of the glacier. The creep laws tested provided varying results, as expected, but it was found that Nye's law was most suitable to the problem. The use of a single law is not adequate for proper analysis of this problem, as the A value varies with temperature and density; however, the results did provide insight into being able to handle incompressibility using lower order

elements. A simple plasticity problem was also solved by modifying the radial return formulation, to demonstrate the versatility of the algorithm. The plasticity analysis was successful in identifying yielding within the glacier.

Overall, best results were obtained by using an algorithm which met or used the following criteria:

- Smoothening - The introduction of smoothening was illustrated to help reduce problems with locking
- Iteration - Iterative solvers provided better results overall, and were easier to work with
- Compressibility - when a material is not fully incompressible, but close ($\nu = 0.4995$), algorithms were more stable, and the problems associated with incompressibility were reduced.

If these criteria are incorporated into the formulation being used, the quality of results was noticeably improved; however, this does not mean that results were free of spurious pressure distributions.

The fractional step method, or velocity correction procedure, was also evaluated. This method was able to provide adequate pressure fields for simple problems, but may not perform well for non-uniform meshes. Experience showed the algorithm to be very sensitive to time step and the initial stress distribution. Finding the time step that maintains stability and an accurate solution was found to be cumbersome. Between the issues involving initial stress distribution and time step size, the algorithm is not recommended without experience.

The fractional step method results for velocity in the Barnes ice cap were less adequate than those obtained with Nye's Flow law, mainly due to the

fact that the analysis was linear. Non-linear analysis using the FSM proved difficult and often could not converge. Best results were obtained using this method for single material, linear, incompressible flow, which severely limits the use of the algorithm.

8.2 Recommendations

The effects of solution schemes, which help to mitigate pathological problems when dealing with incompressibility are documented within this study; however, problems with incompressible zones, such as those involving incompressible plastic flow, were not explored in detail. Results obtained from the extreme case of creep flow were promising, as such domains containing areas of incompressibility can likely be dealt with more effectively. A detailed study of analysis on domains which are not fully incompressible is recommended. The extension of the fractional step method to non-linear cases may also be a worthwhile endeavour, given the computational efficiency of the algorithm. In order to do this, the effects in initial stress distribution on the flow solution would also need to be quantified.

Bibliography

[1] J. Bonet and A.J. Burton. A Simple Average Nodal Pressure Tetrahedral Element for Incompressible and Nearly Incompressible Dynamic Explicit Applications. *Communications in Numerical Methods in Engineering*, 14:437–449, 1998.

[2] J. Bonet, H. Marriott, and O. Hassan. Stability and comparison of different linear tetrahedral formulations for nearly incompressible explicit dynamic applications. *International Journal for Numerical Methods in Engineering*, 50:119–133, 2001.

[3] D.H. Chan. Creep and Fracture Simulation of Ice using the Finite Element Method. Master's thesis, McMaster University, 1981.

[4] A.J. Chorin. A Numerical Method for Solving Incompressible Viscous Flow Problems. *Journal of Computational Physics*, 2:12–16, 1967.

[5] C. Coetzee. The Material Point Method. *University of Stellenbosch*, 2005.

[6] E.A de Souza Neto, F.M. Andrade Pires, and D.R.J. Owen. F-bar-based linear triangles and tetrahedra for finite strain analysis of near incompressible solids. Part I: formulation and benchmarking. *International Journal for Numerical Methods in Engineering*, 62:353–383, 2005.

[7] C. Detournay and E. Dzik. Nodal Mixed Discretization for tetrahedral elements. *4th International FLAC Symposium on Numerical Modeling in Geomechanics*, 07, 2006.

[8] J. Van Egmond. *Simulation of Large Mass Ice Flow* . PhD thesis, McMaster University, 1978.

[9] J.J. Emery. *Finite Element Analysis of Creep Problems in Soil Mechanics*. PhD thesis, 1971.

[10] J.W. Glen. The creep of polycrystalline ice. *Proceedings of the Royal Society of London*, 228:519–538, 1955.

[11] L.W. Gold. Some Bulk Properties of Ice. *Natonal Research Council of Canada, Division of Building Research*, 256, 1967.

[12] E.A. Hanafy. Finite Element Simulation of Tunnel Excavations in Creeping Rock. Master's thesis, McMaster University, 1976.

[13] E.A. Hanafy. Ice Flow Studies. *McMaster University*, 1977.

[14] R.L. Hooke. Structure and Flow in the Margin of the Barnes Ice Cap, Baddin Island, N.W.T, Canada. *Journal of Glaciology*, 12:423–438, 1973.

[15] M. Huang, S. Wu, and O.C. Zienkiewicz. Incompressible or nearly incompressible soil dynamics behaviour - a new staggered algorithm to circumvent restrictions of mixed formulation. *Soil Dynamics and Earthquake Engineering*, 21:169–179, 2001.

[16] M. Huang, Z.Q. Yue, L.G. Tham, and O.C. Zienkiewicz. On the stable finite element procedures for dynamic problems of saturated porous media.

International Journal for Numerical Methods in Engineering, 61:1421–1450, 2004.

[17] M. Kawahara and K. Ohmiya. Finite Element Analysis of Density Flow using the Velocity Correction Method. *International Journal for Numerical Methods in Fluids*, 5:981–993, 1985.

[18] M.S. Killeavy. Particle Path Determination in Large Ice Masses using the Finite Element Method. Master's thesis, McMaster University, 1985.

[19] H. Kraus. *Creep Analysis*. Wiley-Interscience Publications, 1980.

[20] P.O. De Micheli and K. Mocellin. Explicit F.E. formulation with modified linear tetrahedral elements applied to high speed forming processes. *CEMEF*, 2000.

[21] T. Nguyen. *Simulation of Ice Flow using the Finite Element Method*. PhD thesis, McMaster University, 1976.

[22] P. Nithiarasu. A Matrix Free Fraction Step Method for Static and Dynamic Incompressible Solid Mechanics. *International Journal for Computational Methods in Egnineering Science and Mechanics*, 75:369–380, 2007.

[23] P. Nithiarasu and O.C. Zienkiewicz. On Stabilization of the CBS algorithm: Internal and External Time steps. *International Journal for Numerical Methods in Engineering*, 48:875–880, 2000.

[24] E. Onate, J. Rojek, R.L. Taylor, and O.C. Zienkiewicz. Finite calculus formulation for incompressible solids using linear triangles and tetrahedra. *International Journal for Numerical Methods in Engineering*, 59:1473–1500, 2004.

[25] M. Pastor, O.C. Zienkiewicz, T.L. Xiaoqing, and M. Huang. Stabilized Finite Elements with Equal Order of Interpolation for Soil Dynamics Problems. *Archives of Computational Methods in Engineering*, 6:3–33, 1999.

[26] W.S.B. Paterson. *The Physics of Glaciers*. Pergamon Press, 1969.

[27] P. Perzyna. Fundamental Problems in Viscoplasticity. *Advances in Applied Mechanics*, 9:243–377, 1966.

[28] P. Sanchez, A. Huespe, and V. Sonzogni. Numerical Performance of a Mixed Stabilized Finite Element Technology for Solid Mechanics. Parallel Implementation. *International Journal for Numerical Methods in Engineering*, 32:1189–1203, 1991.

[29] G.E. Schneider, G.D. Raithyby, and M.M. Yovanovichi. Finite-Element Solution Procedures for Solving the Incompressible Navier-Stokes Equations using Equal Order Variable Interpolation. *Numerical Heat Transfer*, 1:433–451, 1978.

[30] D.F.E. Stolle. *Finite Element Modelling and Instability of Large Ice Masses*. PhD thesis, McMaster University, 1982.

[31] D.F.E. Stolle. Interpretation of a Galerkin Approach to Time Stepping. *Journal of Sound and Vibration*, 108:513–518, 1995.

[32] D.F.E. Stolle. Meaningful Numerical Modelling in Geotechnical Engineering. CGS short course, 2011.

[33] D.F.E. Stolle, I. Jassim, and P. Vermeer. Accurate simulation of incompressible problems in geomechanics. *Proceedings of CMM - 2009, Computer Methods in Mechanics*, 2009.

[34] R.G. Suave and D.R. Metzger. Advances in Dynamic Relaxation Techniques for Nonlinear Finite Element Analysis. *ASME*, 117:170–176, 1995.

[35] G.N. Wells, L.J. Sluys, and R. de Borst. A p-adapative for overcoming volumetric locking during plastic flow. *Computer methods in applied mechanics and engineering*, 191:3153–3164, 2002.

[36] O.C. Zienkiewicz. Achievements and some unsolved problems of the finite element method. *International Journal for Numerical Methods in Engineering*, 47:9–28, 2000.

[37] O.C. Zienkiewicz and I.C. Cormeau. Achievements and some unsolved problems of the finite element method. *International Journal for Numerical Methods in Engineering*, 8:821–845, 1974.

[38] O.C. Zienkiewicz, J. Rojek, R.L. Taylor, and M. Pastor. Triangles and Tetrahedra in Explicity Dynamic Codes for Solids. *International Journal for Numerical Methods in Engineering*, 43:565–583, 1998.

[39] O.C. Zienkiewicz and R.L. Taylor. The Finite Element Method: The Basis, 2000.

[40] O.C Zienkiewicz, R.L. Taylor, and P. Nithiarasu. *The Finite Element Method Vol. 3* , volume 6, pages 79–105. Butterworth-Heinemann, 2005.

[41] O.C. Zienkiewicz and S. Wu. Incompressibility without tears How to avoid restrictions of mixed formulation. *International Journal for Numerical Methods in Engineering*, 32:1189–1203, 1991.